ATMIRE

Title	Effects of thermomechanical pretreatment on abnormal grain growth during simulated carburization, The
Item Type	Text
Authors	Gruich, James M.
Publisher	Colorado School of Mines. Arthur Lakes Library
Rights	Copyright of the original work is retained by the author.
Download date	2026-11-28 06:17:33
Link to Item	https://hdl.handle.net/11124/179343

THE EFFECTS OF THERMOMECHANICAL PRETREATMENT ON ABNORMAL GRAIN GROWTH DURING SIMULATED CARBURZIIZATION

By

James M. Gruich

A thesis submitted to the Faculty and Board of Trustees of the Colorado School of Mines in partial fulfillment of the degree of Master of Science (Metallurgical and Materials Engineering)

Golden, Colorado

Date_____

Signed: _____

James M. Gruich

Signed: _____

Dr. Kip O. Findley

Thesis Advisor

Golden, Colorado

Date_____

Signed: _____

Dr. Ivar Reimanis

Professor and Head

Department of Metallurgical and Materials Engineering

ABSTRACT

Carburization followed by quenching, and tempering is frequently utilized in the automotive industry to increase the surface hardness and compressive residual stress of a steel alloy while retaining toughness and ductility in the core. At carburizing temperatures, austenite grains are formed and abnormal grain growth (AGG) can occur. During AGG, the steel microstructure undergoes bimodal grain growth with some grains growing exponentially faster than others. The growth of large austenite grains through AGG compromises the fatigue performance of carburized steels. AGG has been shown to be further exacerbated by cold work introduced into the alloy prior to carburizing.

Warm and cold work are also sometimes utilized in part forming prior to carburizing. In this study, the effects of warm work and warm work in combination with cold work on austenite grain size were investigated. AISI 4121with added Al and N and a modified AISI 4121 with additions of Nb and Mo were homogenized, warm reduced by 0-50 pct at a temperature of 900 °C, subjected to cold reduction ranging from 0-25 pct, and then heated in a furnace for 0-328 min at a temperature of 930 °C after ramping up 8 °C min^{-1} from room temperature to simulate a carburizing heat treatment without a carburizing atmosphere.

WR resulted in refinement of the resulting ferritic and secondary microconstituent microstructures. The average prior austenite grain size (PAGS) and AGG also tended to decrease as WR and CR increased. The refinement due to WR and CR were roughly equivalent, but the addition of CR tended to decrease the effectiveness of grain refinement due to WR. The alloy condition with the coarsest average PAGS and highest degree of AGG was 4121Nb after a 328 min hold time, equivalent to a full carburization cycle. 4121Al had a higher relative grain refinement across a majority of experimental conditions, as well as a lower degree of AGG on average. The precipitates present in 4121Al were exclusively AlN and those present in 4121Nb included both AlN and finer precipitates interpreted to be Nb(C,N).

TABLE OF CONTENTS

ABSTRACT iii

LIST OF FIGURES vi

LIST OF TABLES xv

ACKNOWLEDGEMENTS xvi

CHAPTER 1: INTRODUCTION 1

1.1 Problem Statement and Industrial Relevance 1

1.2 Project Objectives 1

CHAPTER 2: BACKGROUND 3

2.1 Significance of Grain Size to Mechanical Properties 3

2.2 Effects of Microalloying Additions on Grain Size Refinement 6

2.3 Strain-Induced Precipitation 13

2.4 Mechanisms of Abnormal Grain Growth 16

2.4.1 Dissolution of Pinning Precipitates 16

2.4.2 Cold Reduction and AGG 21

CHAPTER 3: EXPERIMENTAL PROCEDURES 25

3.1 Experimental Materials 25

3.2 Thermomechanical Processing 25

3.3 Microstructure Analysis 29

3.4 Thermodynamic Modeling 29

3.5 Carbon Extraction Replication and TEM 29

CHAPTER 4: RESULTS AND DISCUSSION 31

4.1 Microstructure and Grain Size Evolution 31

4.1.1 Initial Microstructure 31

4.1.2 Effects of Warm and Cold Reduction on PAGS and AGG 34

4.2 Precipitate Size and Compositional Evolution 46
4.3 Analysis of the Effects of Thermomechanical Pretreatment and Microalloying Additions on Microstructural Evolution 53
CHAPTER 5: CONCLUSIONS 55
5.1 Effects of Warm and Cold Reduction on Microstructural Development 55
5.2 Effects of Composition on Precipitate and Microstructural Evolution 55
CHAPTER 6: FUTURE WORK 57
REFERENCES 58
APPENDIX A: MICROGRAPHS OF EACH WARM REDUCTION AND COLD REDUCTION COMBINATION 62
APPENDIX B: 2D PLOTS OF AIL AND AGG 69
APPENDIX C: AIL WITH RESPECT TO WARM AND COLD REDUCTION 77
APPENDIX D: COPYRIGHT PERMISSIONS 81

LIST OF FIGURES

Figure 2.1 Microstructure of an Fe-0.2C alloy quenched to form martensite with (a) etched to show austenite grain boundaries and (b) etched to show martensite [12]. 4

Figure 2.2 Relationship between austenite grain size and martensite packet size for Fe-Mn alloys [11]. 5

Figure 2.3 Relationship between martensite packet size and martensite yield strength [14]. 5

Figure 2.4 Correlation coefficients for selected specimen characteristics on bending fatigue endurance limits of carburized and hardened alloy steels [3]. 6

Figure 2.5 Solubility product plots of (a) AlN and (b) NbC with respect to temperature and wt pct of constituent elements. 8

Figure 2.6 AGS values of pseudo-carburized 20MnCr5, 4120Mod, and 4121Mod steels. The specimens were heat-treated by (a) austenitizing at 900 ℃ for 1 hour, followed by isothermal annealing at 650 ℃ for 1.5 hours and air cooling, and (b) subcritical annealing at 700 ℃ for 3 hours and air cooling [18]. 11

Figure 2.7 Model predictions of (a) NbC number density and volume fraction, (c) NbC size, and (d) Nb concentration in the austenite matrix of 0.084C-0.015N-0.06Nb after holding at an initial temperature of 1300 ℃ and subsequent cooling down to 950 ℃. Predictions of the same model with 0.33 true strain during annealing shows (b) NbC number density, (d) NbC size, and (f) Nb concentration in austenite matrix [29]. 15

Figure 2.8 Microstructure of 4121Nb after 50 pct WR and 10 pct CR and 328 minutes at 930 ℃. The arrows indicate abnormally grown grains which are noticeably larger than those of the normal microstructure that they are surrounded by. 17

Figure 2.9 Average prior austenite grain sizes of the (a) non-deformed and (b) 50 pct CR specimens after annealing at various temperatures for 1800 s [34]. 18

Figure 2.10 Heat treatment cycles of low alloy steel to obtain as rolled (AR) and fully precipitated (FP) states and subsequent heat treatment of both the states [9]. 19

Figure 2.11 (a) Average prior austenite grain sizes of AR and FP with respect to 1 hour heat treatments at various temperatures and (b) volume fraction taken up by the largest 10 pct of grains (by diameter) [9]..... 20
Figure 2.12 (a) Micrograph of As Rolled (AR) condition heat treated at 1050 ℃ for 1 h, (b) grain size distribution of AR condition in terms of volume fraction, (c) micrograph of Fully Precipitated (FP) condition heat treated at 1050 ℃ for 1 h, and (d) grain size distribution of FP condition in terms of volume fraction [9]..... 20
Figure 2.13 Austenite grain growth behavior at various annealing temperatures in specimens deformed at various reduction ratios [34]. 21
Figure 2.14 (a) Volume fraction and (b) size of the AlN particles in the undeformed (ST) and 50 pct CR (STD-50%) specimens after annealing at various temperatures for 1800 s [34]. 22
Figure 2.15 Diagram of the time-temperature processing history showing a multi-step treatment composed of subcritical annealing, cold rolling (CR), subcritical annealing, and final CR prior to simulated carburizing [35]. 23
Figure 2.16 (a) Average PAGS and (b) number density of abnormally grown austenite grains after simulated carburization in 4121 (Ref Steel) and Nb-modified 4121 (Nb Steel) as a function of CR amount [35]. 24
Figure 3.1 Diagram depicting the thermomechanical history of the (a) as-forged sample and (b) the warm forged samples where the zig-zag lines indicate points where work was done on the material, and the lower temperature zig-zags specifically indicate cold reduction at room temperature.....26
Figure 3.2 Diagram of steel billet and its separate bars after shearing, each bar denoted with the amount of warm reduction it underwent and the as-forged piece, which was not subjected to warm forging. 26
Figure 3.3 Photograph of (a) the AISI 4121 bars stacked on top of each other after warm reduction and (b) subsequently wrapped in thick wool and allowed to cool, simulating industrial conditions. 27

Figure 4.1 4121Al initial microstructures for (a) as-forged, (b) 0 pct WR, (c) 10 pct WR, (d) 25 pct WR, and (e) 50 pct WR conditions and 4121Nb initial microstructures for (f) as-forged, (g) 0 pct WR, (h) 10 pct WR, (i) 25 pct WR, and (j) 50 pct WR conditions, 2 pct nital etch. Olympus® DSX500 light optical micrographs. 32

Figure 4.2 Microstructure of 4121Al after (a) 0 pct WR and (b) subsequent simulated carburization at 930 ℃ for 328 min and (c) 50 pct WR and (d) subsequent simulated carburization at 930 ℃ for 328 min. 2 pct nital etch was used for (a) and (c), picral etch for (b) and (d). Olympus® DSX500 light optical micrographs. 33

Figure 4.3 Microstructure of 4121Nb after (a) 0 pct WR and (b) subsequent simulated carburization at 930 ℃ for 328 min and (c) 50 pct WR and (d) subsequent simulated carburization at 930 ℃ for 328 min. 2 pct nital etch was used for (a) and (c), picral etch for (b) and (d). Olympus® DSX500 light optical micrographs. 34

Figure 4.4 Micrographs of each WR condition and the as-forged condition of 4121Al after 0 pct CR and picral etching at 1664x magnification. (a)-(e) depict the 0 min dwell time condition, (f)-(j) depict the 30 min dwell time condition, and (k)-(o) depict the 328 min dwell time condition. Olympus® DSX500 light optical micrographs. 35

Figure 4.5 Micrographs of each WR condition and the as-forged condition of 4121Nb after 0 pct CR and picral etching at 1664x magnification. (a)-(e) depict the 0 min dwell time condition, (f)-(j) depict the 30 min dwell time condition, and (k)-(o) depict the 328 min dwell time condition. Olympus® DSX500 light optical micrographs. 36

Figure 4.6 3D surface plots that depict the average intercept length with respect to both WR and CR for 4121Al after (a) 0 min, (b) 30 min, and (c) 328 min. The color of the surface varies according to the heights specified by AIL, with lighter such as yellow being high AIL and darker colors such as blue being lower AIL. 39

Figure 4.7 3D surface plots that depict the average intercept length with respect to both WR and CR for 4121Nb after (a) 0 min, (b) 30 min, and (c) 328 min. The color of the surface varies according to the heights specified by AIL, with lighter such as yellow being high AIL and darker colors such as blue being lower AIL. 40
Figure 4.8 (a) AIL of 4121Al after 0 pct CR and (b) 10 pct CR with respect to WR and (c)AIL of 4121Nb after 0 pct CR and (d) 10 pct CR with respect to WR. ... 41
Figure 4.9 3D surface plots that depict the number density of abnormally grown grains with respect to both WR and CR for 4121Al after (a) 0 min, (b) 30 min, and (c) 328 min. The color of the surface varies according to the heights specified by AIL, with lighter such as yellow being high AIL and darker colors such as blue being lower AIL. 43
Figure 4.10 3D surface plots that depict the number density of abnormally grown grains with respect to both WR and CR for 4121Nb after (a) 0 min, (b) 30 min, and (c) 328 min. The color of the surface varies according to the heights specified by AIL, with lighter such as yellow being high AIL and darker colors such as blue being lower AIL. 44
Figure 4.11 Comparison of (a) PAGS of 4121Al and (c) PAGS of 4121Nb observed by Lee *et al.* after simulated carburization with (b) AIL of 4121Al after 50 pct WR and (d) AIL of 4121Nb after 50 pct WR [35]. 45
Figure 4.12 Comparison of the microstructures of 4121Nb after (a) the thermomechanical pre-treatment done by Lee *et al.* [5] and (b) 0 pct WR prior to cold reduction and simulated carburization in the current work..... 46
Figure 4.13 Plots of volume fraction of AlN with respect to temperature in (a) 4121Al and (b) 4121Nb with vertical dashed lines denoting 900 ℃, 930 ℃, and 1230 ℃, respectively. 48
Figure 4.14 Plots of volume fraction of Nb(C,N) with respect to temperature in (a) 4121Al and (b) 4121Nb with vertical dashed lines denoting 900 ℃, 930 ℃, and 1230 ℃, respectively. 48

Figure 4.15 Plot showing respective mass percentage of Nb, Mo, N, and C in Nb(C,N) with respect to temperature in 4121Nb with vertical dashed lines denoting 900 ℃, 930 ℃, and 1230 ℃, respectively. 49
Figure 4.16 CER sites with precipitates present in 0 pct WR+0 pct CR 4121Al at 30 kx magnification. Bright field images taken with FEI Tecnai T12 Transmission Electron Microscope. 50
Figure 4.17 CER sites with precipitates present in 0 pct WR+0 pct CR 4121Nb at 30 kx magnification. Bright field images taken with FEI Tecnai T12 Transmission Electron Microscope. 51
Figure 4.18 EDS spectrum of precipitate site shown in Figure 4.16(a). 52
Figure A-1 Micrographs of each WR condition and the as-forged condition of 4121Al after 5 pct CR and picral etching at 1664x magnification. (a)-(e) depict the 0 min dwell time condition, (f)-(j) depict the 30 min dwell time condition, and (k)-(o) depict the 328 min dwell time condition. Olympus® DSX500 light optical micrographs. 63
Figure A-2 Micrographs of each WR condition and the as-forged condition of 4121Nb after 5 pct CR and picral etching at 1664x magnification. (a)-(e) depict the 0 min dwell time condition, (f)-(j) depict the 30 min dwell time condition, and (k)-(o) depict the 328 min dwell time condition. Olympus® DSX500 light optical micrographs. 64
Figure A-3 Micrographs of each WR condition and the as-forged condition of 4121Al after 10 pct CR and picral etching at 1664x magnification. (a)-(e) depict the 0 min dwell time condition, (f)-(j) depict the 30 min dwell time condition, and (k)-(o) depict the 328 min dwell time condition. Olympus® DSX500 light optical micrographs. 65
Figure A-4 Micrographs of each WR condition and the as-forged condition of 4121Nb after 10 pct CR and picral etching at 1664x magnification. (a)-(e) depict the 0 min dwell time condition, (f)-(j) depict the 30 min dwell time condition, and (k)-(o) depict the 328 min dwell time condition. Olympus® DSX500 light optical micrographs. 66

Figure A-5 Micrographs of each WR condition and the as-forged condition of 4121Al after 25 pct CR and picral etching at 1664x magnification. (a)-(e) depict the 0 min dwell time condition, (f)-(j) depict the 30 min dwell time condition, and (k)-(o) depict the 328 min dwell time condition. Olympus® DSX500 light optical micrographs. 67

Figure A-6 Micrographs of each WR condition and the as-forged condition of 4121Nb after 25 pct CR and picral etching at 1664x magnification. (a)-(e) depict the 0 min dwell time condition, (f)-(j) depict the 30 min dwell time condition, and (k)-(o) depict the 328 min dwell time condition. Olympus® DSX500 light optical micrographs. 68

Figure B-1 Average intercept length of each CR condition with respect to WR for both alloys where 4121Al has been subjected to (a) 0 pct CR, (c) 5 pct CR, (e) 10 pct CR, and (g) 25 pct CR and 4121Nb after (b) 0 pct CR, (d) 5 pct CR, (f) 10 pct CR, and (h) 25 pct CR. 69

Figure B-2 Average intercept length of each WR condition with respect to CR for both alloys where 4121Al has been subjected to (a) 0 pct WR, (c) 10 pct WR, (e) 25 pct WR, (g) 50 pct WR, and (i) the as-forged condition and 4121Nb after (b) 0 pct WR, (d) 10 pct WR, (f) 25 pct WR, (h) 50 pct WR, and (j) the as-forged condition. 71

Figure B-3 Percentage area of abnormal grains normalized over the total microstructural area of each CR condition with respect to WR for both alloys where 4121Al has been subjected to (a) 0 pct CR, (c) 5 pct CR, (e) 10 pct CR, and (g) 25 pct CR and 4121Nb after (b) 0 pct CR, (d) 5 pct CR, (f) 10 pct CR, and (h) 25 pct CR. 73

Figure B-4 Percentage area of abnormal grains normalized over the total microstructural area of each WR condition with respect to CR for both alloys where 4121Al has been subjected to (a) 0 pct WR, (c) 10 pct WR, (e) 25 pct WR, (g) 50 pct WR, and (i) the as-forged condition and 4121Nb after (b) 0 pct WR, (d) 10 pct WR, (f) 25 pct WR, (h) 50 pct WR, and (j) the as-forged condition. 75

Figure D-1 Grain size frequency determined by line-intercept measurement in MATLAB of the as-forged condition for both alloys after 0 min of simulated carburization where 4121Al has been previously subjected to (a) 0 pct CR, (c) 5 pct CR, (e) 10 pct CR, and (g) 25 pct CR and 4121Nb after (b) 0 pct CR, (d) 5 pct CR, (f) 10 pct CR, and (h) 25 pct CR. 81
Figure D-2 Grain size frequency determined by line-intercept measurement in MATLAB of the as-forged condition for both alloys after 30 min of simulated carburization where 4121Al has been previously subjected to (a) 0 pct CR, (c) 5 pct CR, (e) 10 pct CR, and (g) 25 pct CR and 4121Nb after (b) 0 pct CR, (d) 5 pct CR, (f) 10 pct CR, and (h) 25 pct CR. 83
Figure D-3 Grain size frequency determined by line-intercept measurement in MATLAB of the as-forged condition for both alloys after 328 min of simulated carburization where 4121Al has been previously subjected to (a) 0 pct CR, (c) 5 pct CR, (e) 10 pct CR, and (g) 25 pct CR and 4121Nb after (b) 0 pct CR, (d) 5 pct CR, (f) 10 pct CR, and (h) 25 pct CR. 85
Figure D-4 Grain size frequency determined by line-intercept measurement in MATLAB of the 0 pct WR condition for both alloys after 0 min of simulated carburization where 4121Al has been previously subjected to (a) 0 pct CR, (c) 5 pct CR, (e) 10 pct CR, and (g) 25 pct CR and 4121Nb after (b) 0 pct CR, (d) 5 pct CR, (f) 10 pct CR, and (h) 25 pct CR. 87
Figure D-5 Grain size frequency determined by line-intercept measurement in MATLAB of the 0 pct WR condition for both alloys after 30 min of simulated carburization where 4121Al has been previously subjected to (a) 0 pct CR, (c) 5 pct CR, (e) 10 pct CR, and (g) 25 pct CR and 4121Nb after (b) 0 pct CR, (d) 5 pct CR, (f) 10 pct CR, and (h) 25 pct CR. 89
Figure D-6 Grain size frequency determined by line-intercept measurement in MATLAB of the 0 pct WR condition for both alloys after 328 min of simulated carburization where 4121Al has been previously subjected to (a) 0 pct CR, (c) 5 pct CR, (e) 10 pct CR, and (g) 25 pct CR and 4121Nb after (b) 0 pct CR, (d) 5 pct CR, (f) 10 pct CR, and (h) 25 pct CR. 91

Figure D-7 Grain size frequency determined by line-intercept measurement in MATLAB of the 10 pct WR condition for both alloys after 0 min of simulated carburization where 4121Al has been previously subjected to (a) 0 pct CR, (c) 5 pct CR, (e) 10 pct CR, and (g) 25 pct CR and 4121Nb after (b) 0 pct CR, (d) 5 pct CR, (f) 10 pct CR, and (h) 25 pct CR. 93
Figure D-8 Grain size frequency determined by line-intercept measurement in MATLAB of the 10 pct WR condition for both alloys after 30 min of simulated carburization where 4121Al has been previously subjected to (a) 0 pct CR, (c) 5 pct CR, (e) 10 pct CR, and (g) 25 pct CR and 4121Nb after (b) 0 pct CR, (d) 5 pct CR, (f) 10 pct CR, and (h) 25 pct CR. 95
Figure D-9 Grain size frequency determined by line-intercept measurement in MATLAB of the 10 pct WR condition for both alloys after 328 min of simulated carburization where 4121Al has been previously subjected to (a) 0 pct CR, (c) 5 pct CR, (e) 10 pct CR, and (g) 25 pct CR and 4121Nb after (b) 0 pct CR, (d) 5 pct CR, (f) 10 pct CR, and (h) 25 pct CR. 97
Figure D-10 Grain size frequency determined by line-intercept measurement in MATLAB of the 25 pct WR condition for both alloys after 0 min of simulated carburization where 4121Al has been previously subjected to (a) 0 pct CR, (c) 5 pct CR, (e) 10 pct CR, and (g) 25 pct CR and 4121Nb after (b) 0 pct CR, (d) 5 pct CR, (f) 10 pct CR, and (h) 25 pct CR. 99
Figure D-11 Grain size frequency determined by line-intercept measurement in MATLAB of the 25 pct WR condition for both alloys after 30 min of simulated carburization where 4121Al has been previously subjected to (a) 0 pct CR, (c) 5 pct CR, (e) 10 pct CR, and (g) 25 pct CR and 4121Nb after (b) 0 pct CR, (d) 5 pct CR, (f) 10 pct CR, and (h) 25 pct CR. 101
Figure D-12 Grain size frequency determined by line-intercept measurement in MATLAB of the 25 pct WR condition for both alloys after 328 min of simulated carburization where 4121Al has been previously subjected to (a) 0 pct CR, (c) 5 pct CR, (e) 10 pct CR, and (g) 25 pct CR and 4121Nb after (b) 0 pct CR, (d) 5 pct CR, (f) 10 pct CR, and (h) 25 pct CR. 103

Figure D-13 Grain size frequency determined by line-intercept measurement in MATLAB of the 50 pct WR condition for both alloys after 0 min of simulated carburization where 4121Al has been previously subjected to (a) 0 pct CR, (c) 5 pct CR, (e) 10 pct CR, and (g) 25 pct CR and 4121Nb after (b) 0 pct CR, (d) 5 pct CR, (f) 10 pct CR, and (h) 25 pct CR. 105
Figure D-14 Grain size frequency determined by line-intercept measurement in MATLAB of the 50 pct WR condition for both alloys after 328 min of simulated carburization where 4121Al has been previously subjected to (a) 0 pct CR, (c) 5 pct CR, (e) 10 pct CR, and (g) 25 pct CR and 4121Nb after (b) 0 pct CR, (d) 5 pct CR, (f) 10 pct CR, and (h) 25 pct CR. 107
Figure D-15 Grain size frequency determined by line-intercept measurement in MATLAB of the 50 pct WR condition for both alloys after 328 min of simulated carburization where 4121Al has been previously subjected to (a) 0 pct CR, (c) 5 pct CR, (e) 10 pct CR, and (g) 25 pct CR and 4121Nb after (b) 0 pct CR, (d) 5 pct CR, (f) 10 pct CR, and (h) 25 pct CR. 109

LIST OF TABLES

Table 2.1 Nb and Mo Compositions of Alloys (in wt pct) 12

Table 2.2 Ratios of Observed Coarsening Rates to Calculated LSW Coarsening Rates 12

Table 2.3 Mean Lineal Intercept of Tempered Alloys Following Ramp to Specified Temperature, Soaking for Specified Time, and Water Quench 12

Table 4.1 Mean Lineal Intercept of Tempered Alloys Following Ramp to Specified Temperature, Soaking for Specified Time, and Water Quench 47

Table C-1 AIL of 4121Al by Warm Reduction 77

Table C-2 AIL of 4121Al by Warm Reduction 77

Table C-3 AIL of 4121Al After 5 pct Cold Reduction by WR 78

Table C-4 AIL of 4121Nb After 5 pct Cold Reduction by WR 78

Table C-5 AIL of 4121Al After 10 pct Cold Reduction by WR 79

Table C-6 AIL of 4121Nb After 10 pct Cold Reduction by WR 79

Table C-7 AIL of 4121Al After 25 pct Cold Reduction by WR 80

Table C-8 AIL of 4121Nb After 25 pct Cold Reduction by WR 80

ACKNOWLEDGEMENTS

From the bottom of my heart, I would like to thank the many people that made this project possible. I would like to thank the Advanced Steel Processing and Products Research Center (ASPPRC) at Colorado School of Mines and its industrial sponsors. I would also like to express gratitude to TimkenSteel for producing and facilitating processing of the experimental lab heats and Nexteer for assistance in the initial project proposal and valuable input on its direction.

I would like to gratefully thank my committee members, Prof. Emmanuel De Moor and Prof. Bob Cryderman. To the ASPPRC faculty, including Karen Coulson and Michael Burnett, I express my thanks for giving me community and helping me through the transformative process of graduate school. To my advisor, Prof. Kip Findley, I want to sincerely express my gratitude for all of the guidance, support, and instruction he has given throughout the completion of this research.

Lastly, I want to truly thank my friends and family for being the ones to get me across the finish line. To my parents, Michael and Bridget, my brothers, Nick and Kevin, my cousins, my aunt and uncle, and every person that gave me even a word of encouragement-you have been the ones that made this possible, and I owe who I am to all of you.

CHAPTER 1: INTRODUCTION

1.1 Problem Statement and Industrial Relevance

Carburization is a widely utilized thermomechanical heat treatment process for steel that improves the wear and fatigue properties of components. The process involves diffusion of carbon into the surface of a low to medium-carbon steel at high temperatures. Carbon diffusion is dependent on three things: carburizing atmosphere, time, and temperature. Increasing carburizing temperatures can lead to a reduction in the time a carburizing cycle takes, but this can come at the expense of austenitic grain coarsening. Microalloying is one methodology that attempts to remediate high-temperature grain coarsening through precipitate pinning of grains [1], [2]. Niobium and aluminum have been utilized in this capacity.

An additional microstructural issue carburized parts may experience is abnormal grain growth (AGG) where select austenite grains grow exponentially faster than those surrounding them, which also negatively impacts fatigue performance [1], [2], [3]. These abnormal grains are likely the result of precipitates dissolving and subsequently facilitating unpinning grains that were previously pinned. These grains, surrounded by others that are still pinned, are able to grow freely at the expense of their neighbors, leading to abnormally large grains [4].

Another factor that affects AGG is cold work prior to carburization. Cold reduction (CR) within a range of approximately 5-20 pct has been shown to increase the amount of AGG that occurs in a carburization heat treatment cycle [5]. Some carburized parts experience not just cold reduction but also warm reduction (WR) at elevated temperatures, the effects of which have not been thoroughly investigated.

1.2 Project Objectives

The objective of this research was to investigate the effect of different degrees of WR and WR in combination with CR as thermomechanical pretreatments on AGG at carburizing temperatures in AISI 4121 steel, a low-carbon carburizing steel. The primary precipitate that forms in 4121 is AlN, and its precipitation can also be affected by WR and CR [6]. Because Nb and Mo have been utilized as microadditions to create precipitates more effective at high-temperature grain refinement relative to AlN, this work also investigated how this precipitation is affected by WR and CR in 4121 with these microadditions. The standard alloy is referred to as 4121Al and the microalloyed 4121 is referred to as 4121Nb to reflect the primary

precipitating element in each alloy. The following questions were developed to address the objectives of this research:

1. *How does warm work affect the microstructural development of 4121Al and 4121Nb and abnormal grain growth during carburization?*
2. *Are previously observed effects of cold reduction on austenite grain coarsening in 4121Al and 4121Nb during simulated carburization affected by warm working prior to cold reduction?*
3. *Do either AlN and Nb(C,N), as the primary pinning precipitates in 4121Al and 4121Nb, respectively, pin austenitic grains more effectively in the thermomechanical processing routes investigated?*

Chapter 2 will provide background information on the topics relevant to this work. Chapter 3 will describe the procedures utilized, and their subsequent results will be discussed in Chapter 4. Conclusions are presented in Chapter 5, followed by recommendations for future work in Chapter 6.

CHAPTER 2: BACKGROUND

In gear, bearing, shaft, and some other part production, carburization is a process that takes place both after the initial heat treatment and annealing of the product and after gear forging. Using gas carburizing as an example, gears are subjected to austenitizing temperatures in an atmosphere of C_3H_8 or C_4H_8, which is broken down into carbon which penetrates through the surface of the steel [7]. This diffusion of carbon leads to surface hardening and improvement of fatigue strength from the surface of the steel to a certain depth into the product (the "case depth") while maintaining a higher toughness within the core of the steel. Unfortunately, a process that is known to occur during carburization, particularly in steels that have been cold worked earlier in their manufacturing process, is abnormal growth of austenitic grains [5], [8].

There are instances where AGG appears to be more prevalent and develops more rapidly in carburizing steels. Steels that have been cold worked to a certain degree and steels with a relatively high volume fraction of initially fine precipitates have demonstrated a higher degree of AGG than the same steels that are non-worked and/or have lower volume fractions of coarser precipitates [5], [9]. Because AGG has been shown to initiate at sites where pinning precipitates dissolve and coarsen, microstructures with high volume fractions of fine, easily dissolvable precipitates would be likely to experience a high degree of AGG. The effects of cold reduction on AGG are less well-understood, and this work attempts to elucidate its effects *via* the use of a wide range of warm and cold reductions in initial thermomechanical processing conditions.

2.1 Significance of Grain Size to Mechanical Properties

Control of grain coarsening during austenitization is valuable in improving the properties of steel. It has been demonstrated by Zackay *et al.* and Krauss that austenite grain size correlates proportionally to resultant martensite packet size [10], [11]. Figure 2.1 shows the microstructure of a Fe-0.2C steel after austenitizing and quenching in water. The microstructure is martensitic. Figure 2.1(a) has been etched to show the prior austenite grain boundaries, and Figure 2.1(b) has been etched to show martensite. The correlation between PAGS and the resultant martensitic microstructure can be seen in Figure 2.1, with martensite packets, groups of parallel laths that

form during transformation, growing within parent austenite grains [12]. Equation 2.1 describes the relationship between tensile properties and martensite structure:

$$\sigma_y = \sigma_i + k\sqrt{c} + k_y d^{\frac{-1}{2}} + \alpha G b\sqrt{\rho} \tag{2.1}$$

where σ_y is the yield strength of martensite, σ_i is overall resistance of lattice to dislocation motion, α and k are constants, c is solute atom concentration, k_y is the locking parameter, d is the martensite packet size, G is the shear modulus, b is the Burgers vector, and ρ is dislocation density [13].

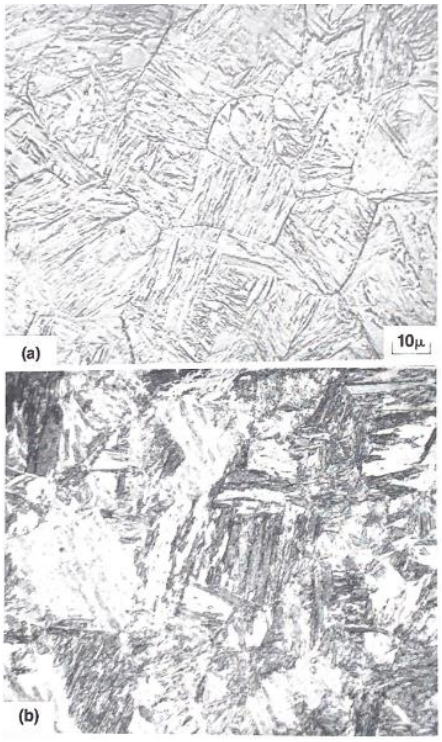


Figure 2.1 Microstructure of an Fe-0.2C alloy quenched to form martensite with (a) etched to show austenite grain boundaries and (b) etched to show martensite [12].

Figure 2.2 shows the experimentally measured relationship between PAGS and martensite packet size, and Figure 2.3 shows the relationship between martensite packet size and martensite strength according to Equation 2.1 [11]. As Figure 2.2 shows that martensite packet size increases proportionally with PAGS and Figure 2.3 shows that strength decreases as packet

size increases, it can be inferred that martensite strength is dependent on PAGS such that a finer PAGS results in a finer martensite packet size and higher martensite strength [8], [11].

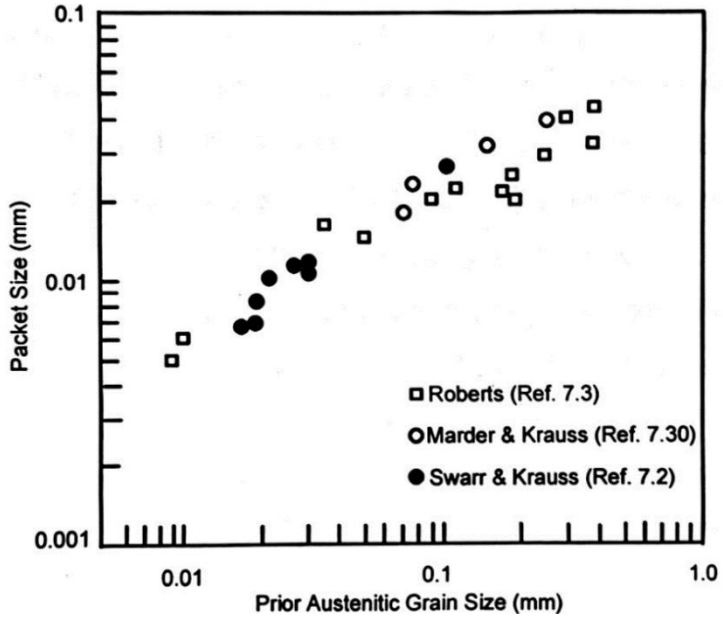


Figure 2.2 Relationship between austenite grain size and martensite packet size for Fe-Mn alloys [11].

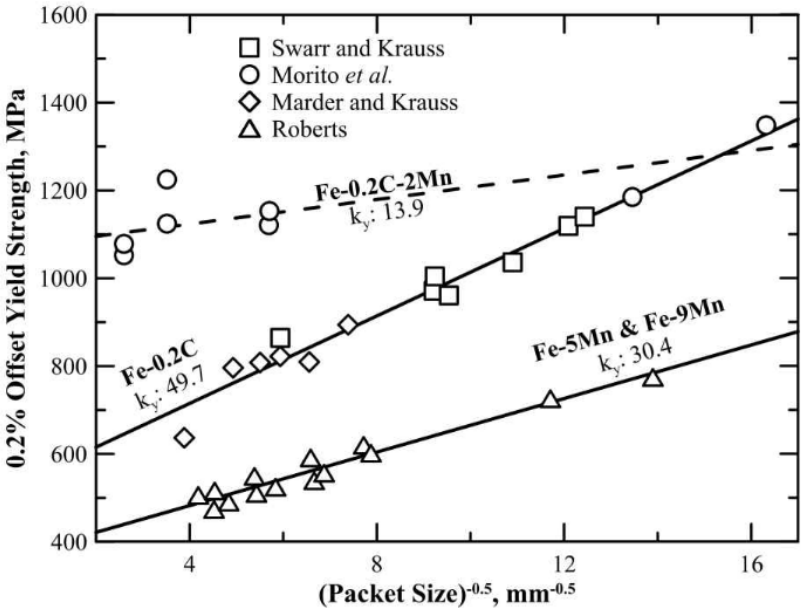


Figure 2.3 Relationship between martensite packet size and martensite yield strength [14].

Wise *et al.* demonstrated through statistical analysis of a large set of experimental fatigue data from a wide range of carburized alloys with the same specimen geometry that austenite grain size is the most important variable that influences the bending fatigue endurance limit. These data were collected by using various carburizing processes, testing bending fatigue with a cantilever beam bending fatigue specimen, and characterizing the microstructures of the case and core of each sample. The results of this study can be seen in Figure 2.4, which shows to what degree certain mechanical and microstructural characteristics affect bending fatigue strength [3]. As can be seen, the case grain size is the most important factor to consider when improving the fatigue performance of a carburized steel.

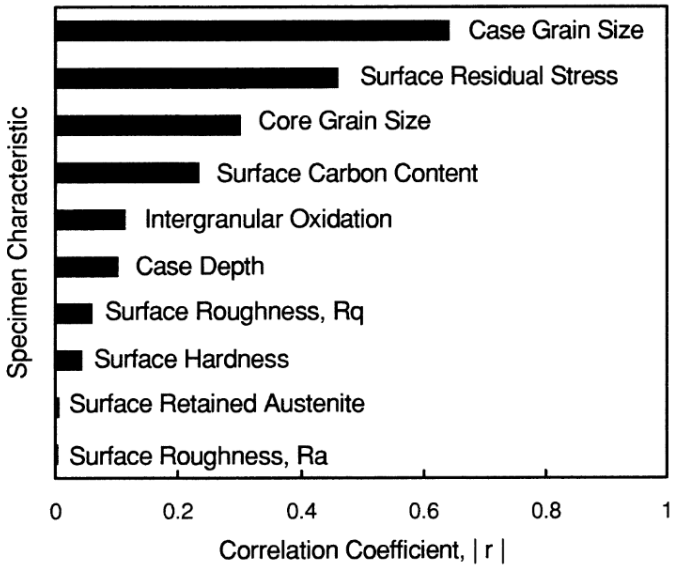


Figure 2.4 Correlation coefficients for selected specimen characteristics on bending fatigue endurance limits of carburized and hardened alloy steels [3].

Wise *et al.* also concluded that decreasing the average austenite grain size also decreases the susceptibility to intergranular fracture, consistent with a previous observation by Ohmori *et al.*, who found that the fracture mode of tempered and untempered martensitic structures changed from intergranular to transgranular by refining austenite grain size [3], [15].

2.2 Effects of Microalloying Additions on Grain Size Refinement

One technique for improving grain size refinement at high temperatures is microalloying which restrict austenitic grain growth *via* precipitation of fine particles that restrict grain boundary movement. As grain growth occurs in polycrystalline arrays to minimize grain

boundary energy, large grains eventually grow at the expense of smaller grains, overtaking them [16]. Microalloy precipitates pin grain boundaries during austenite grain growth through a reduction in grain boundary surface area due to the intersection of grain boundaries and second-phase precipitates. This intersection creates a local energy minimum when the area of intersection is maximized, which results in halting grain boundary motion.

The relationship between grain size and pinning precipitates is described by Zener in Equation 2.2:

$$r_{crit} = 3\frac{R_0 f}{\pi}(3 - \frac{4}{Z})^{-1} \quad (2.2)$$

where R_0 is the average grain size, Z is a parameter representing the inhomogeneity of the initial grains, f is the volume fraction of second-phase particles, and r_{crit} is the radius of the pinning precipitates. A lower volume fraction of precipitates and/or a finer average precipitate radius both result in a finer austenite grain size.

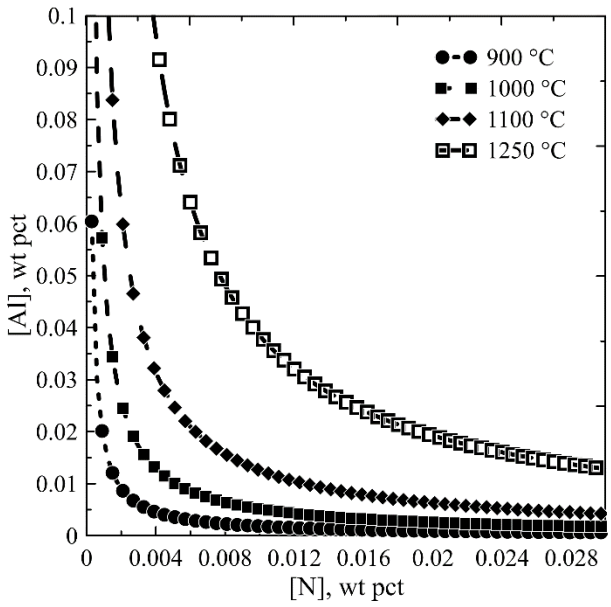
AlN is a conventionally used precipitate for grain refinement in carburizing steels. NbN and NbC are also used through microalloying with Nb. Generally, less NbN forms than NbC due to the limited amount of free nitrogen in carburizing steels. Due to the mutual solubility of NbC and NbN, Nb precipitates are designated as Nb(C,N) [17]. Though Nb(C,N), particularly with additional Mo microadditions, have been shown to persist at high temperatures (1050 °C) and coarsen more slowly than AlN, AlN is a more conventional approach to grain refinement in steels [18], [19], [20].

Following Equation 2.2, the most important factors in the development of precipitates for the purpose of grain size control in a steel undergoing heat treatment are increasing volume fraction and minimizing average precipitate radius. Volume fraction is largely dependent on the solubility of a particular microalloy precipitate [21]. The solubility products of AlN and NbC (the primary precipitates considered in this work in austenite) are defined in Equations 2.3 and 2.4, respectively, as:

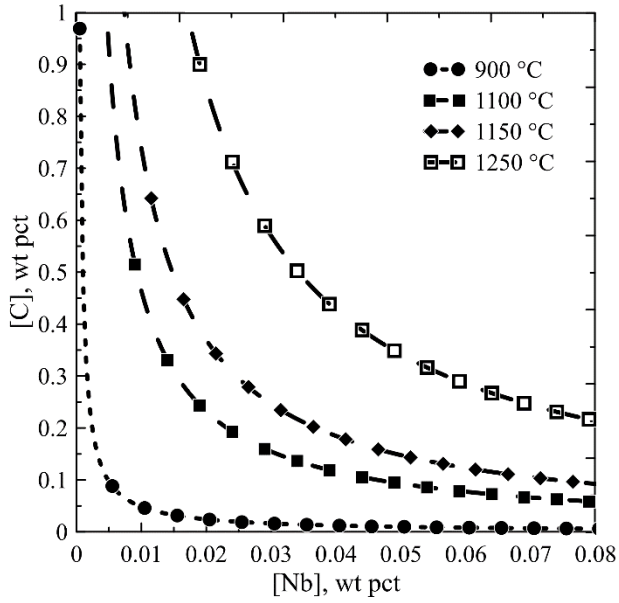
$$logk_s = -\frac{6770}{T} + 1.03 \quad (2.2)$$

$$logk_s = -\frac{6770}{T} + 2.26 \quad (2.3)$$

where logk_s is -4.5976 in Equation 2.3 and -3.14692 in Equation 2.4 [21]. Solubility product plots for AlN and NbC are shown in Figure 2.5(a) and (b) for AlN and NbC, respectively.



(a)



(b)

Figure 2.5 Solubility product plots of (a) AlN and (b) NbC with respect to temperature and wt pct of constituent elements.

The precipitate radius is dictated by the growth and coarsening rate of a given species.

In general, microalloy precipitate coarsening has been shown to follow the Lifshitz-Slyozov-Wagner (LSW) relation shown in Equation 2.5:

$$r^3 - r_0^3 = \frac{8D_M \Omega [M] \gamma_{P/M}}{9RT} \cdot t \tag{2.5}$$

where r and r_o are the instantaneous average and initial average particle radii, respectively, D_M is the diffusion coefficient for the carbonitride forming metal (rate controlling species) in the given matrix, *[M]* is the concentration in solution of the carbonitride forming metal (rate controlling species) in atomic fraction, Ω is the molar volume of the precipitate, $\gamma_{P/M}$ is the particle/matix interfacial energy, R is the ideal gas constant, T is the absolute temperature, and t is the time in seconds. For a given temperature, assuming a similar solute concentration and initial precipitate size, the diffusion coefficient for Al is greater than that of Nb, meaning that AlN precipitates coarsen more rapidly than Nb(C,N) [22], [23], [24].

The coarsening rate of Nb(C,N) in austenite in particular was defined by Martín *et al.* as the expression in Equation 2.5 using experimental austenite grain size measurement under non-isothermal heating conditions:

$$r^3 = r_0^3 + \frac{4\sigma V_m}{9R\theta} \int_{A_{c_3}}^{T} \frac{[Nb] D_V}{T} \, dT \tag{2.5}$$

where r is the radius of carbonitrides in microns, T is the absolute temperature, σ is the interfacial energy per unit area between precipitate and matrix ($0.5 \cdot 10^{-12}$ Jμm^{-2}) [25], V_m is the molar volume of carbonitrides ($1.28 \cdot 10^{13}$ μm^{3}mol^{-1}) [25], [Nb] is the amount of niobium in mass pct in solid solution in equilibrium with the austenite matrix, θ is the heating rate, and D_V is the coefficient of niobium volume diffusion in grain boundaries ($9.3 \cdot 10^8 \exp(-291966/RT)$ μm^{2}s^{-1}). The main conclusion by Martín *et al.* was that the coarsening of Nb(C,N) was mainly controlled by volume diffusion of Nb in austenite, with a higher rate of volume diffusion leading to a higher coarsening rate [24].

Seo *et al.* and Enloe *et al.* demonstrated in their work that Mo as a microalloying addition in conjunction with Nb can decrease the coarsening rate of Nb-rich precipitates, consequently increasing the temperature at which austenite grain coarsening initiates [18], [19]. Seo *et al.* studied three similar carburizing steels: 20MnCr5, 4120Mod (modified to add Mo and Nb), and 4121Mod (modified to add Mo and Nb). The three steels had increasing amounts of Mo (0.01,

0.15, and 0.29 wt pct respectively) and were subjected to carburizing temperatures with two different pre-heat treatment cycles.

The first pre-heat treatment (referred to as pre-heat treatment 1) consisted of austenitizing at 900 ℃ for 1 hour, allowing the steels to cool to 650 ℃ to isothermally anneal for 1.5 hours before air-cooling to room temperature. The second pre-heat treatment (referred to as pre-heat treatment 2) only subjected the steels to subcritical annealing at 700 ℃ for 3 hours before being air cooled. These pre-heat treatment steps were conducted in order to simulate two different processing paths a shaped carburized part could be subjected to prior to carburization. Pre-heat treatment 1 aimed to improve machinability of the material by obtaining blocky ferrite and pearlite microstructures. Pre-heat treatment 2 was designed to soften the material by the formation and the annealing of ferrite and bainite from the initial martensitic/austenitic microstructure, which would provide improved cold workability.

While the Mo content did not impact the average PAGS significantly when heat treating in the 930-1000 ℃ range, when heat treating above 1000 ℃, the presence of Mo reduced average grain size (AGS) by 10-40 μm compared to the alloy without Mo additions (20MnCr5), as can be seen in Figure 2.6 [18].

The effects of the pre-heat treatments can also be seen when comparing Figure 2.6(a) and (b), which show that a higher volume fraction of Mo in a Nb microalloyed steel will proportionally improve grain refinement at high temperatures. The 0.01 wt pct Mo alloy that was subjected to pre-heat treatment 1 had a larger average grain size after a soak temperature of 1050 ℃, but finer AGS after 1100 ℃ when compared to the same alloy subjected to pre-heat treatment 2. The 0.15 wt pct Mo alloy, when only subcritically annealed rather than austenitized and annealed, had a larger AGS after both 1050 ℃ and 1100 ℃. The 0.29 wt pct Mo alloy maintained average grain sizes finer than the other two alloys at all temperatures after both pre-heat treatment methods, with little difference in final AGS [18]. These results show that the addition of Mo improves grain refinement at high temperatures in Nb microalloyed carburizing steels.

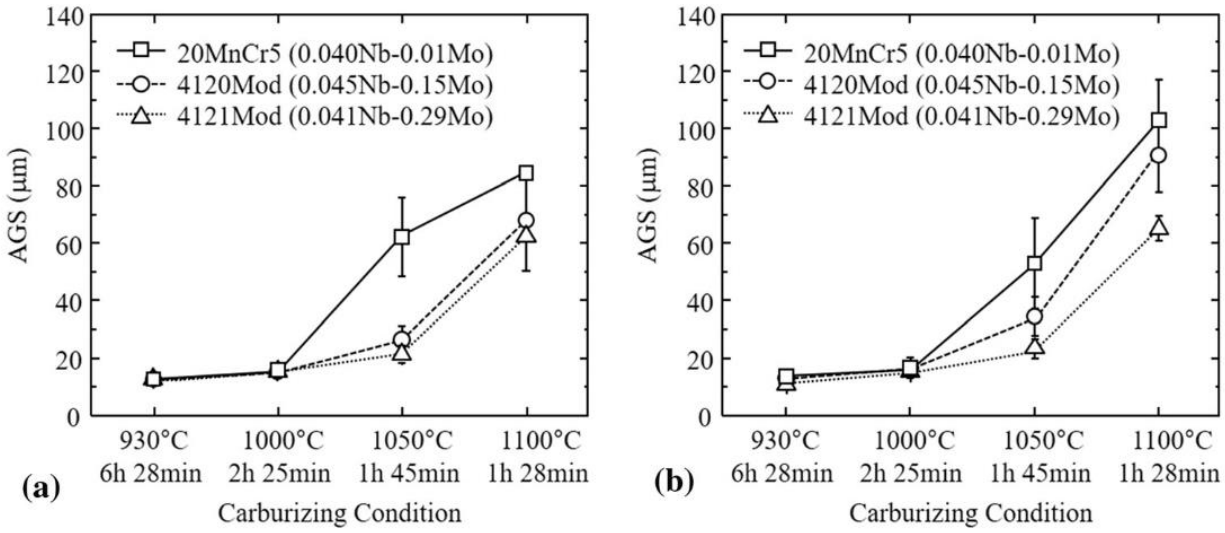


Figure 2.6 AGS values of pseudo-carburized 20MnCr5, 4120Mod, and 4121Mod steels. The specimens were heat-treated by (a) austenitizing at 900 ℃ for 1 hour, followed by isothermal annealing at 650 ℃ for 1.5 hours and air cooling, and (b) subcritical annealing at 700 ℃ for 3 hours and air cooling [18].

Enloe *et al.* experimented with changing both Nb and Mo content of an SAE 4120 steel tempered at 600 ℃ prior to heat treatment. These heat treatments consisted of holding the steels for 90 min at 1050 ℃ and 60 min at 1100 ℃. The Nb and Mo compositions in the alloys used by Enloe are listed in Table 2.1. It was found that the ratio of experimental coarsening rates of NbC precipitates with calculated LSW coarsening rates consistently increased with the addition of Nb and consistently decreased with the addition of Mo, which can be seen in

Table 2.2. The decrease in coarsening rates due to Mo resulted in a higher austenite grain coarsening temperature and finer resultant microstructures. These results seem to imply that low-Nb, high-Mo microalloying additions in 4120 are ideal for minimizing high-temperature austenite grain coarsening. The mean lineal intercepts (MLI) of the PAGS of differing compositions can be seen in

Table 2.3 [19].

Without the addition of Mo,

Table 2.3 shows that the addition of Nb to 4120 can decrease the MLI by tens of microns after soaking at 1100 ℃. The effect of Mo additions can be seen when comparing the LNb and MoLNb conditions. The addition of Mo similarly results in reduction in MLI after 1100 ℃.

These results indicate that Nb and Mo microadditions in 4120 reduce grain coarsening at temperatures in excess of 1050 °C. The MLI refinement due to Nb and Mo coincided with increased AGG onset temperatures [19].

Table 2.1 Nb and Mo Compositions of Alloys (in wt pct)

Composition	Nb	Mo
LNb	0.044	0
HNb	0.110	0.01
MoLNb	0.044	0.30
MoHNb	0.110	0.30

Table 2.2 Ratios of Observed Coarsening Rates to Calculated LSW Coarsening Rates

Composition	1050 °C	1100 °C
LNb	3.8	6.9
HNb	7.4	22
MoLNb	3.3	2.7
MoHNb	6.5	10

Table 2.3 Mean Lineal Intercept of Tempered Alloys Following Ramp to Specified Temperature, Soaking for Specified Time, and Water Quench

Composition	1050 °C for 90 min (μm)	1100 °C for 60 min (μm)
LNb	16.9	44.9
HNb	16.8	18.9
MoLNb	17.0	25.0
MoHNb	16.5	17.2

Mo has been suggested to reduce the diffusivity of Nb, which is the presumed mechanism behind Mo decreasing the coarsening rate of austenite. Lee *et al.* performed simulated hot rolling on low-carbon steels with variations in Nb and Mo compositions. After finishing rolling, the metal carbide (MC)-type precipitates became finer and denser as the amount of Mo increased. EDS analysis indicated that the finer MC carbides had a higher ratio of Mo/Nb. The conclusion drawn by Lee *et al.* was that, similar to Mn, Mo lowers both the diffusivity of Nb and the driving force for precipitation [26], [27]. Thermo-Calc predicted that, as Mo content increased, the driving force of MC precipitates would decrease. Additionally, atom probe analysis of a hot rolled Ti-Nb-Mo steel conducted by Uemori *et al.* found Mo to segregate strongly at the

Nb(C,N)/ferrite matrix interface, which likely suppressed the diffusion of Nb atoms into Nb(C,N) from the ferrite matrix, directly resulting in fine precipitates in the Ti-Nb-Mo steel [28].

2.3 Strain-Induced Precipitation

Within steel, precipitate formation is separated into two stages-nucleation and growth, and coarsening. The activation energy for precipitate nucleation is determined by three parameters: (i) the chemical free energy arising from the chemical supersaturation of the solutes, (ii) the interfacial energy spent for creating the precipitate/matrix interface, and (iii) the strain energy used to accommodate a strain mismatch [29]. The introduction of dislocations into a microstructure *via* strain results in the creation of dislocation nodes where precipitates can nucleate heterogeneously. The presence of these dislocation nodes in addition to the dislocation energy introduced into the system leads to a lower activation energy for nucleation with a greater number of nucleation sites. The critical radius for nucleation is the radius a randomly-formed supercritical cluster of atoms must reach in order to nucleate. The critical radius depends on the driving force for transformation and the interfacial energy, but is typically reached after some incubation time [30]. Once the critical radius and the mean radius of the precipitates becomes nearly equal at the end of this incubation period, coarsening begins and is assisted by pipe diffusion along dislocations, as they are the primary sites where precipitates form [29]. In summary, the introduction of dislocations into a system allows precipitates to nucleate, grow, and coarsen at an accelerated rate compared to an non-deformed structure [29], [31], [32]. Based on this, the dislocation density proves to be an important variable to understand the predicted rate of nucleation and coarsening. In a study by Dutta *et al.*, the kinetics of strain induced precipitation of NbC in austenite in a Nb microalloyed steel (0.084C-0.015N-0.06Nb) were modeled and found to show good agreement with experimental observations from previous work. The steel was heated to 1300 ℃ and subsequently cooled down to 950 ℃, at which point the experimental alloy was deformed to a true strain of 0.33 and held isothermally, likely to simulate conventional hot rolling.

Figure 2.7 shows the differences in NbC number density, formation rate, and size in a non-deformed sample in comparison to one that has experienced 0.33 true strain as defined by the modelling by Dutta *et al*. Figure 2.7(a) and (b) show that the precipitate number density is much higher, and precipitation begins at a much earlier time, in the deformed sample, leading to

a maximum number density and subsequent coarsening at a much earlier time. In Figure 2.7(c) and (d), it can be seen that the mean radius of the precipitates in the deformed sample was also significantly finer due to a lower activation energy required for precipitation on dislocations, resulting in a very high nucleation rate, which led to smaller average precipitate radii. The early onset of nucleation and coarsening are the result of this lower activation energy for precipitation and enhanced coarsening kinetics due to dislocation-assisted diffusion. The higher nucleation rate at an earlier time also led to a much quicker depletion of Nb within the austenite matrix, which can be seen when comparing Figure 2.7(e) and (f). Figure 2.7(e), which shows results for the non-deformed sample, did not have any reduction in Nb in the matrix until after an incubation time of ~16 minutes. In contrast, the Nb concentration in the matrix of the deformed sample, as can be seen in Figure 2.7(e), seemed to begin depletion immediately, without any incubation [29].

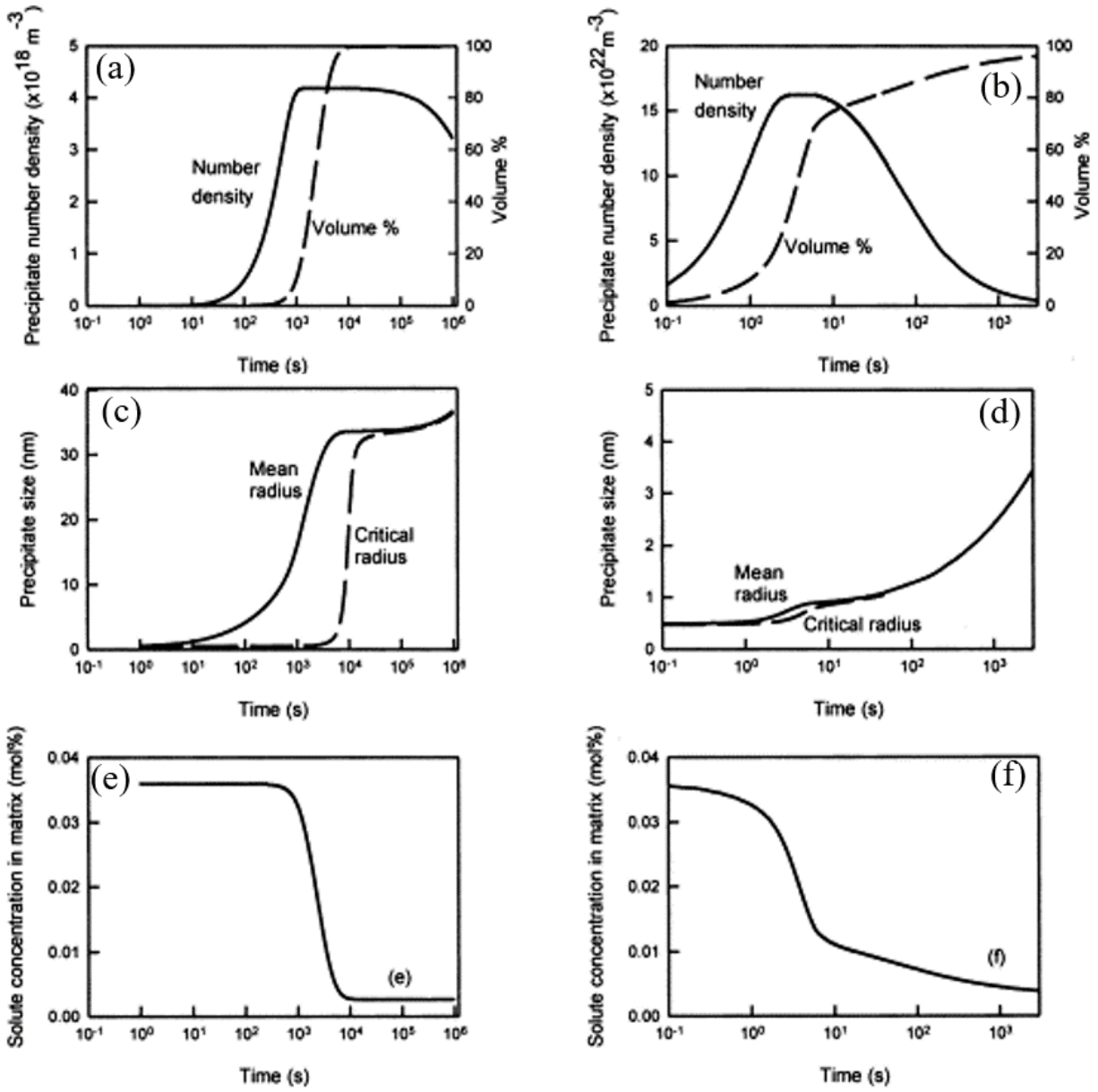


Figure 2.7 Model predictions of (a) NbC number density and volume fraction, (c) NbC size, and (d) Nb concentration in the austenite matrix of 0.084C-0.015N-0.06Nb after holding at an initial temperature of 1300 ℃ and subsequent cooling down to 950 ℃. Predictions of the same model with 0.33 true strain during annealing shows (b) NbC number density, (d) NbC size, and (f) Nb concentration in austenite matrix [29].

2.4 Mechanisms of Abnormal Grain Growth

2.4.1 Dissolution of Pinning Precipitates

AGG is the unwanted bimodal grain growth of austenite during heat treatment. An example of prior austenite grains that have undergone AGG can be seen in Figure 2.8 for an SAE 4121 steel with additional microalloying of Nb and Mo after 50 pct WR at 900 °C, 10 pct CR, and 328 minutes of soaking at 930 °C after a ramp rate of 8 °C/min from room temperature. As can be seen, a few very large grains are present within a microstructure that has grains that are much smaller on average. Abnormal grains much larger than their surrounding neighbors compromise the fatigue performance in a heat treated part [3], [33]. This issue is further explained in Section 2.1. Lowered fatigue strength is obviously undesirable in industrially produced parts that require consistent performance and high quality, and as conventional carburization takes place at high temperatures (900-1000 °C), AGG is a consistent issue that requires deliberate mitigation [7].

Work by Holm *et al.* [4] demonstrated that within a mesoscale grain growth simulation of 3D polycrystals containing static particle dispersions, AGG always initiates in one of the largest grains in a system (about 2.4 times larger in diameter than the average grain). Grains that grow abnormally first thermally fluctuate away from their pinning particles. After this, due to the surrounding grains being rendered immobile due to still being pinned, the now-free grain can then freely grow without competing for area with its immobile neighbors. As this abnormal grain grows, its size advantage further increases its ability to grow at the expense of its neighbors.

The mechanism which initiates this AGG is the dissolution of the pinning precipitates in the microstructure. As material is heated in the austenitic temperature range, precipitates coarsen and eventually begin to dissolve. According to Equation 2.2, both coarsening and dissolution contribute to an increase in the average austenite grain size. Grain growth increases rapidly at sites where precipitate coarsening and dissolution occur, causing local regions of AGG.

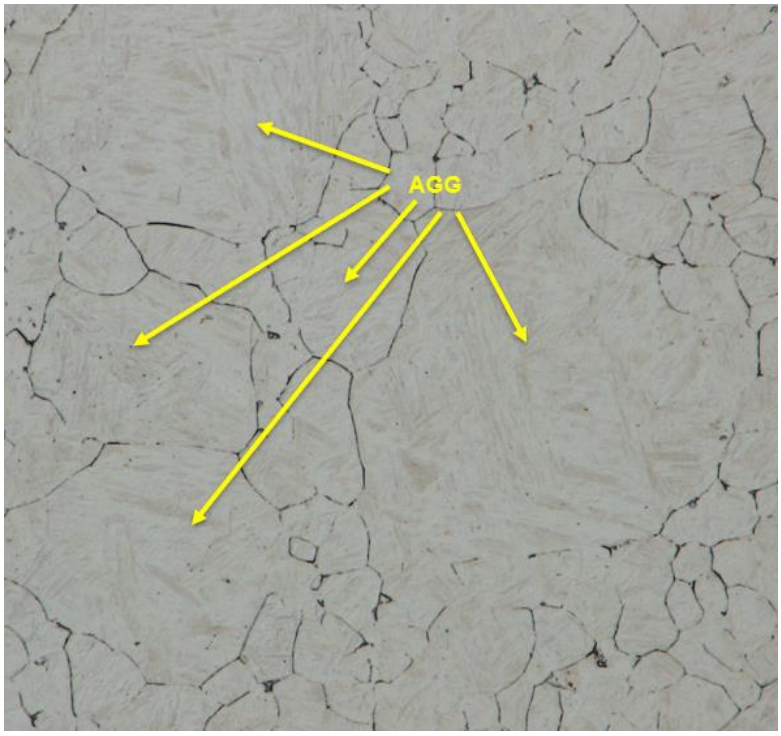


Figure 2.8 Microstructure of 4121Nb after 50 pct WR and 10 pct CR and 328 minutes at 930 °C. The arrows indicate abnormally grown grains which are noticeably larger than those of the normal microstructure that they are surrounded by.

Further evidence that dissolving precipitates initiate AGG can be seen in work by Zhang *et al.* and Razzak *et al.* Zhang *et al.* subjected a low alloy steel with AlN as the primary pinning precipitate to cold reduction and subsequent annealing at temperatures between 1173-1473 K for time periods ranging from 0-30 minutes. Figure 2.9(a) shows a range of temperatures the undeformed steel was subjected to for 30 minutes. The figure shows the temperature ranges where normal grain growth (NGG) ends, AGG begins, and NGG resumes for a static hold time. Each heat treatment performed below ~1325 K resulted in a final microstructure that underwent NGG. Above 1325 K, the temperature which closely matches where AlN begins to dissolve (T_c), AGG initiates. AGG continues to occur in the range ~1325-1400 K, but transitions back to NGG at 1400 K, the approximate temperature at which AlN completely dissolves (T_f) [34].

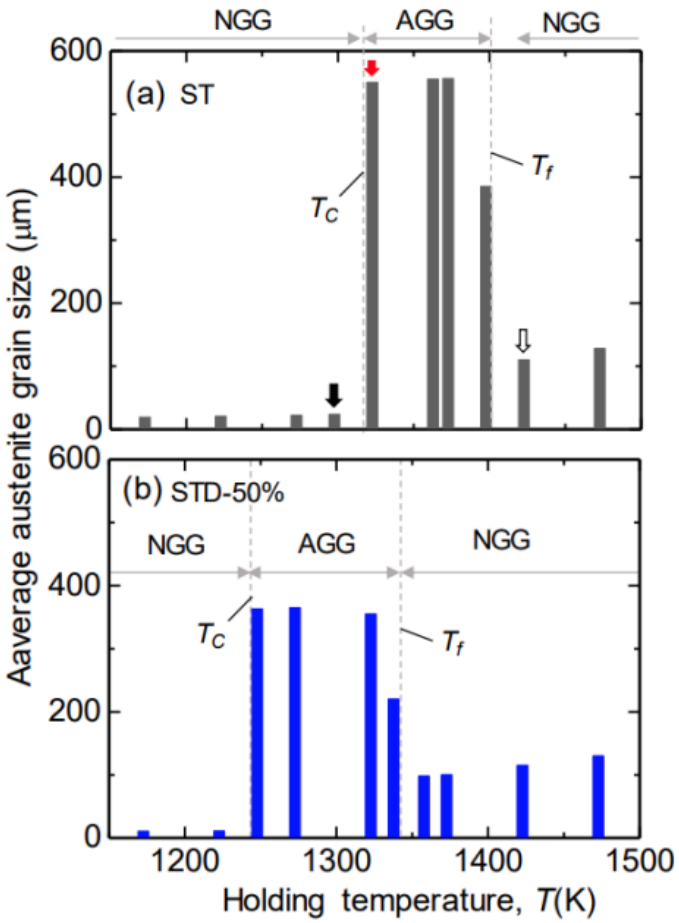


Figure 2.9 Average prior austenite grain sizes of the (a) non-deformed and (b) 50 pct CR specimens after annealing at various temperatures for 1800 s [34].

Razzak *et al.*, using a different low-alloy steel with AlN as its primary precipitate, conducted two different heat treatment cycles to obtain two distinct states with different volume fractions of the primary precipitate. These two states were denoted as “as rolled” (AR) and “fully precipitated” (FP), where AR mimicked the heat treatment of a hot rolled steel, and FP included an additional austenitization and annealing step meant to maximize the amount of AlN precipitated out of solution. These two conditions were then each subjected to 1 hour of soaking at 900, 1050, and 1200 °C. The full thermomechanical history of AR and FP can be seen in Figure 2.10.

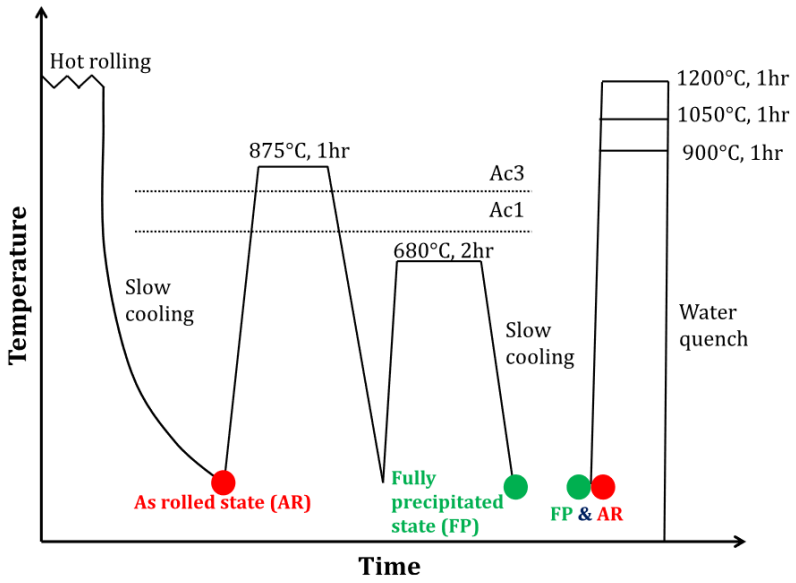


Figure 2.10 Heat treatment cycles of low alloy steel to obtain as rolled (AR) and fully precipitated (FP) states and subsequent heat treatment of both the states [9].

The volume fraction of AlN in FP prior to heat treatment was ~0.03 wt pct. AR had a lower relative volume fraction of AlN of ~0.015 %. Razzak *et al.* defined AGG as occurring when the total volume fraction taken up by the largest 10 pct of grains changes. Figure 2.11(a) shows the average PAGS with respect to temperature, and AR and FP do not diverge significantly. Figure 2.11(b) shows the total volume fraction of the 10 pct largest grains. Below 1050 °C, grain growth proceeded normally in both conditions. However, in the FP condition at 1050 °C, there was a significant jump in total volume fraction taken up by the largest 10 pct of grains, indicating the onset of AGG.

Figure 2.12(a) and (c) show the difference in grain size between the AR and FP conditions, and Figure 2.12(b) and (d) show the difference in overall grain size distribution after heat treatment at 1050 °C. A larger amount of AGG occurred in the FP condition than the AR condition, as evidenced both by the micrographs and the grain size distribution, with abnormally large grains being plainly visible in the microstructure and the distribution showing that grain size skews to grains with diameters greater than 65 µm.

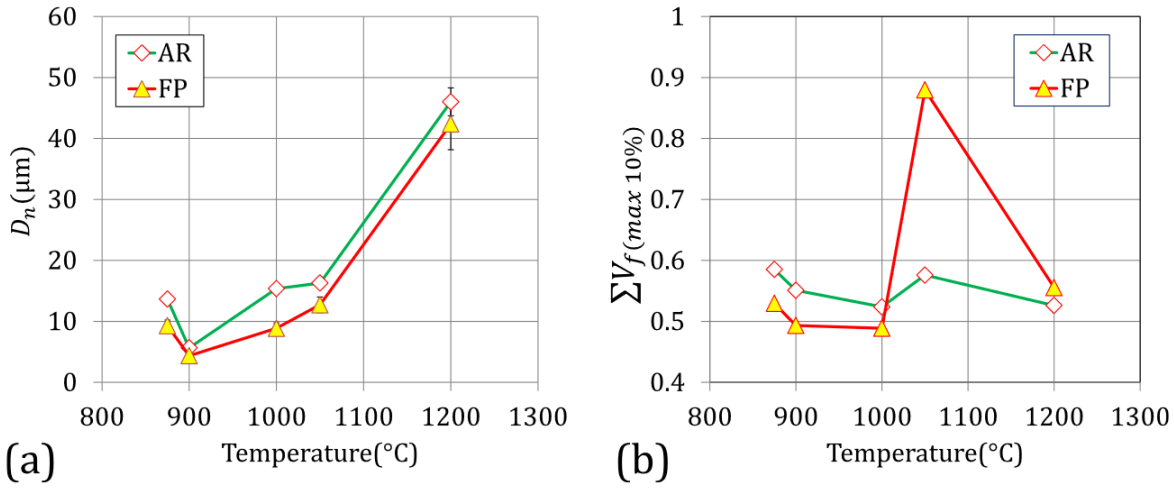


Figure 2.11 (a) Average prior austenite grain sizes of AR and FP with respect to 1 hour heat treatments at various temperatures and (b) volume fraction taken up by the largest 10 pct of grains (by diameter) [9].

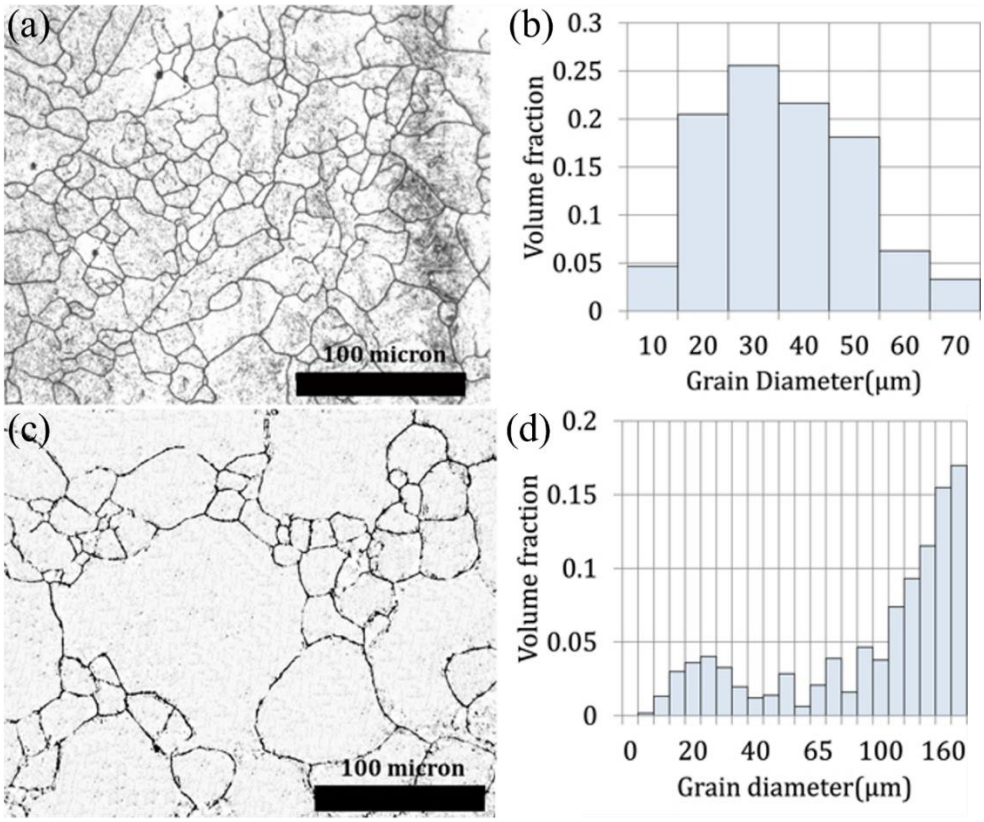


Figure 2.12 (a) Micrograph of As Rolled (AR) condition heat treated at 1050 °C for 1 h, (b) grain size distribution of AR condition in terms of volume fraction, (c) micrograph of Fully Precipitated (FP) condition heat treated at 1050 °C for 1 h, and (d) grain size distribution of FP condition in terms of volume fraction [9].

2.4.2 Cold Reduction and AGG

The effect of CR on AGG can be seen in work by Zhang *et al.* and Lee *et al.* From work by Zhang, which had no pre-treatment steps prior to heat treatment, Figure 2.9(b) shows the temperature regions where NGG and AGG occur when 50 pct CR is performed prior to heat treatment. When compared to the non-deformed condition, the temperature region where AGG initiates and ceases shifts to a lower temperature regime. The effect of increasing CR on the AGG temperature regime can be seen more clearly in Figure 2.13, which shows the temperature range where AGG occurs after CR ranging from 0 pct to 70 pct. Up to a certain point (50 pct CR), CR decreases the temperatures at which AGG both initiates and ceases. The lowering of T_c and T_f with increased work is likely due to the effect the work has on the kinetics of precipitation, which was discussed in Section 2.3 [29], [34].

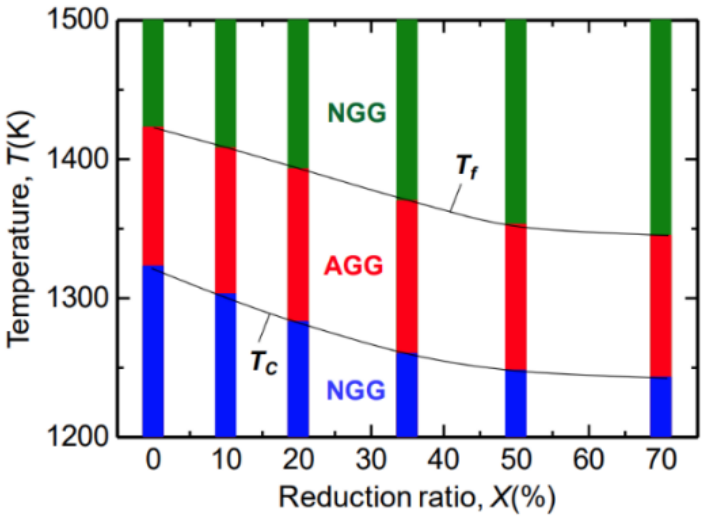


Figure 2.13 Austenite grain growth behavior at various annealing temperatures in specimens deformed at various reduction ratios [34].

Similar to what was observed in work by Dutta *et al.*, work done prior to heat treatment led to both a reduction in precipitate size and an increase in the initial volume fraction [29]. Figure 2.14(a) shows that at the lowest heat treatment temperatures, the volume fraction of AlN present in the 50 pct deformed specimen (labeled as STD-50%) is approximately 40 pct higher than that of the non-deformed specimen (labeled as ST), with the gap between the two conditions closing as temperature increases until 1350 K. Figure 2.14(b) shows that the deformed condition has a finer average AlN diameter at all temperatures. The reduced precipitate size in the

50 pct CR condition results in precipitates that can more easily dissolve, and a high volume fraction of fine precipitates that dissolve more easily results in a high amount of AGG [34].

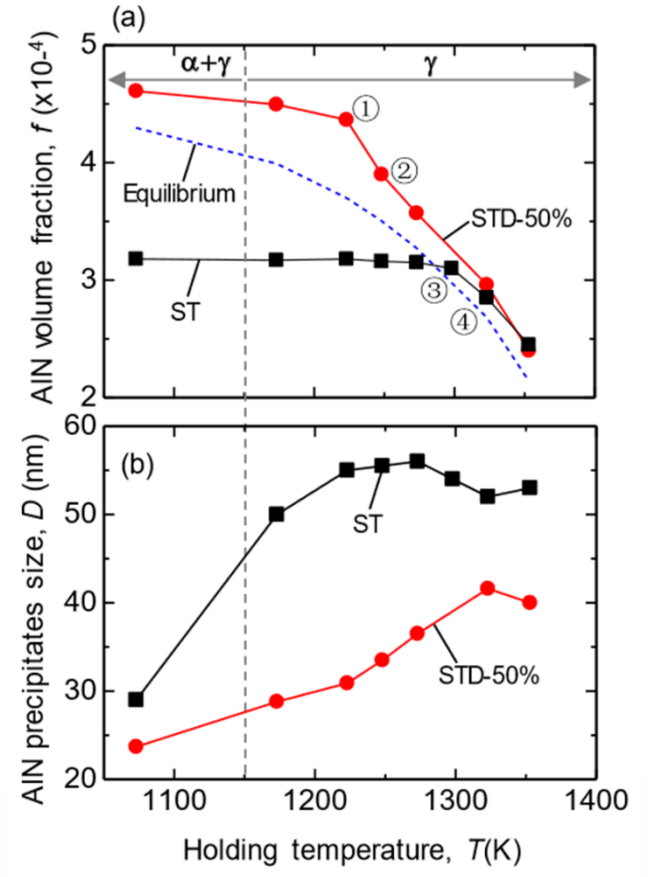


Figure 2.14 (a) Volume fraction and (b) size of the AlN particles in the undeformed (ST) and 50 pct CR (STD-50%) specimens after annealing at various temperatures for 1800 s [34].

Lee *et al.* varied the degree of CR done to an SAE 4121 and Nb-modified 4121 (reference steel) with 0.04 wt pct Nb prior to a simulated carburization process that simulated carburizing heat treatment conditions without a carburizing atmosphere. The time-temperature processing history used by Lee *et al.* can be seen in Figure 2.15 which shows the two subcritical annealing steps and 50 pct CR done prior to simulated carburization. The key step in the processing history is the 2nd CR performed prior to the carburizing simulation, with a range of CR between 0-50 pct.

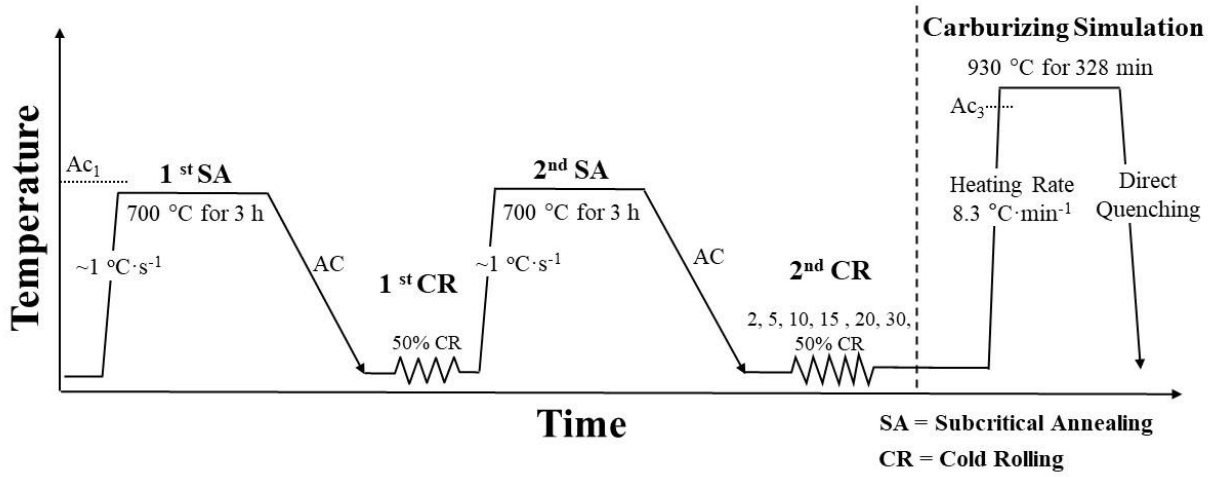
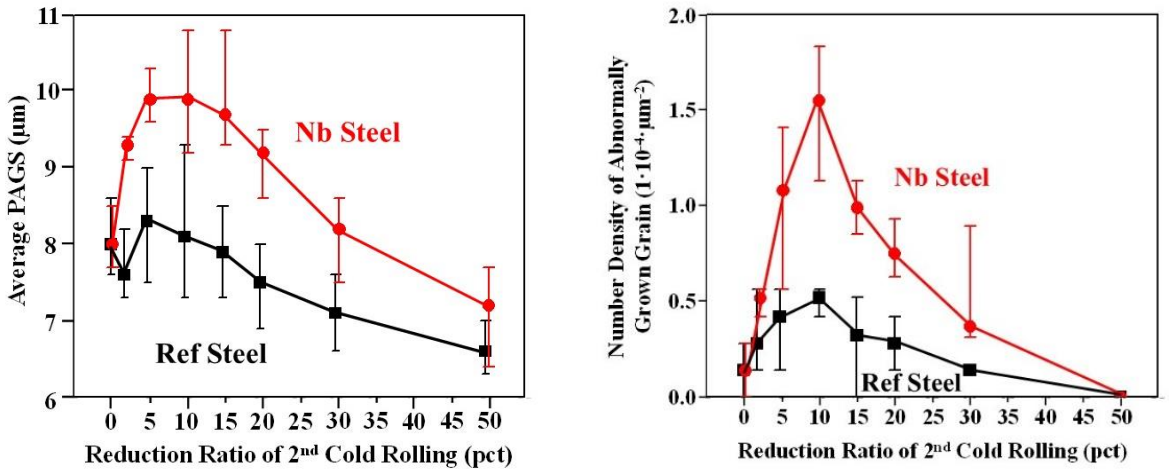


Figure 2.15 Diagram of the time-temperature processing history showing a multi-step treatment composed of subcritical annealing, cold rolling (CR), subcritical annealing, and final CR prior to simulated carburizing [35].

The PAGS of both alloys was measured after this range of reductions by picral etching. The average PAGS of both alloys, shown in Figure 2.16(a), shows that the reference steel had a finer average PAGS than the Nb-modified steel at all reductions besides 0 pct CR. The average PAGS of both alloys increased between 0-5 pct CR, and the PAGS of the Nb-modified 4121 increased until 10 pct CR. The average PAGS decreased consistently up to 50 pct CR after peaking at 5 and 10 pct CR for the reference steel and Nb-modified steels, respectively. Figure 2.16(b) shows that the number density of abnormally grown grains (grains with a diameter ≥30 μm) was greater in the Nb-modified alloy at all CR conditions compared to the reference steel besides 0 pct CR. The number density of abnormal grains in both alloys also similarly increased from 0 to 10 pct CR, decreasing with additional CR up to 50 pct, where no abnormal grains were measured in either alloy [35].



(a) (b)

Figure 2.16 (a) Average PAGS and (b) number density of abnormally grown austenite grains after simulated carburization in 4121 (Ref Steel) and Nb-modified 4121 (Nb Steel) as a function of CR amount [35].

CHAPTER 3: EXPERIMENTAL PROCEDURES

This chapter presents the experimental methodology utilized to achieve the project objectives outlined in Section 1.2. The topics include thermomechanical processing, metallographic preparation and analysis, and carbon extraction replica preparation and analysis.

3.1 Experimental Materials

Two AISI 4121 grade carburizing steels were used for this project. The composition of the standard AISI 4121 steel (denoted as 4121Al) and the composition of the Nb-modified 4121 steel (denoted as 4121Nb) are listed in Table 3.1. It should be noted that nitrogen was also added to the 4121Al steel to increase the amount of AlN precipitates. Seo *et al.* [18] demonstrated that, in comparison to a similar alloy with lower Nb and Mo content, the fatigue performance of NbMo-modified carburizing steel was improved by reducing prior austenite grain size and precipitate coarsening at temperatures ranging from 930-1050 ℃, particularly at 1050 ℃. Hold time varied with heat treatment temperature, with samples in the 1050 ℃ cycle being held for 105 min, increasing to 328 min at 930 ℃. Similar compositions of Nb and Mo to those used by Seo *et al.* were added to the 4121Nb ingots in this work to determine if the same reduction in coarsening and precipitate size would be observed after warm and cold reduction. Ingots were fabricated by TimkenSteel through vacuum induction melting and later forged at Solmet Technologies to produce ten bars with varying degrees of WR. These particular alloys were used in order to have a comparative analysis with previous work [5].

Table 3.1 Chemical Composition of 4121 Steels (in wt pct)

Steel	C	Mn	Si	Mo	Nb	Al	N	P	S
4121Al	0.21	0.79	0.23	0.21	0.002	0.024	0.0152	0.002	0.004
4121Nb	0.22	0.77	0.24	0.30	0.041	0.009	0.0069	0.002	0.008

3.2 Thermomechanical Processing

Figure 3.1 shows the time-temperature processing history of the steel through initial forging and subsequent testing. The two initial ingots were heated to 1230 °C for homogenization, forged into bars, cut into five 38.1 mm thick pieces, and were allowed to air cool to room temperature. Four pieces of each respective bar were then reheated to 900 °C to

simulate warm forging as shown in Figure 3.1(b), with the fifth piece being left out to provide a reference for the as-forged condition shown in Figure 3.1(a). Each condition experienced CR ranging from 0-25 pct and were then heated to 930 °C at a rate of 8 °C /min to simulate carburization.

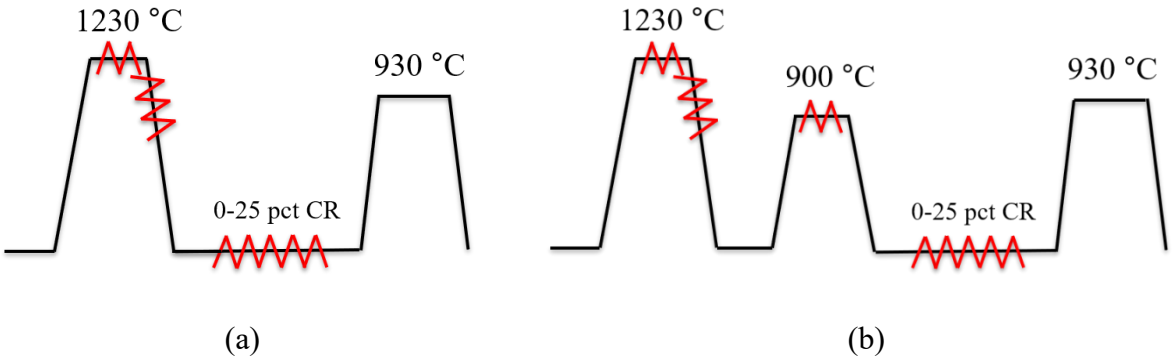


Figure 3.1 Diagram depicting the thermomechanical history of the (a) as-forged sample and (b) the warm forged samples where the zig-zag lines indicate points where work was done on the material, and the lower temperature zig-zags specifically indicate cold reduction at room temperature.

The four pieces re-heated to 900 °C of each alloy were warm forged to reduce the thicknesses by 0 pct, 10 pct, 25 pct, and 50 pct, respectively, with the 0 pct piece simply removed from the re-heat furnace and allowed to cool. Figure 3.2 is a diagram showing the separation from ingots to bars and subsequent deformation.

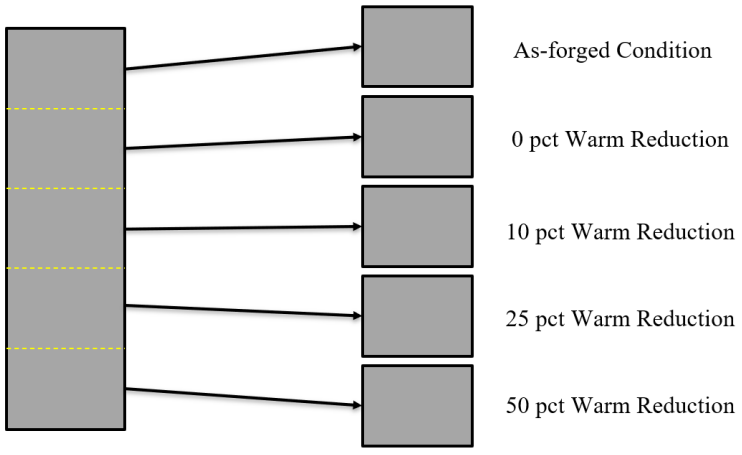


Figure 3.2 Diagram of steel billet and its separate bars after shearing, each bar denoted with the amount of warm reduction it underwent and the as-forged piece, which was not subjected to warm forging.

Recrystallization is relevant to this experiment due to high temperature working conditions. The non-recrystallization temperature (T_{NR}) in particular is most relevant. T_{NR} is the temperature below which complete recrystallization does not occur. The non-recrystallization temperature for these alloys was calculated to be approximately 887 °C for 4121Al and 1027 °C for 4121Nb through use of the Boratto equation [36]

$$T_{NR}=464C-\left(644\sqrt{Nb}-6445Nb\right)-\left(230\sqrt{V}-732V\right)+(363Al\cdot 890T_i)+(-357Si)+887 \quad (3.2)$$

where *Nb*, *V*, *Ti*, *C*, and *Si* represent the elements' amounts in wt pct in the alloy. From this calculation, complete recrystallization will not theoretically occur for 4121Nb during warm reduction at 900 °C, as its T_{NR} is over 100 °C above the warm working temperature. The 4121Al, however, should fully recrystallize during warm reduction.

In the industrial conditions that this project is attempting to simulate, parts are collected in a bin immediately after warm forging to create a large thermal mass and are allowed to cool to room temperature. To create cooling conditions analogous to those for warm forged parts, the warm forged bars were stacked on top of each other immediately after WR and subsequently sealed within a thick wool blanket until they cooled to room temperature, as shown in Figure 3.3.



(a) (b)

Figure 3.3 Photograph of (a) the AISI 4121 bars stacked on top of each other after warm reduction and (b) subsequently wrapped in thick wool and allowed to cool, simulating industrial conditions.

Cold reductions of 0, 5, 10, and 25 pct were performed with a FENN® Rolling Mill on each of the warm forged conditions. For cold rolling, each ingot was machined to create bars of a uniform thickness of 21 mm and with greater widths than heights. To obtain a sample for each

CR condition, a section of each bar was removed at each of the desired CR percentages as the cold rolling progressed (5 pct, 10 pct, and 25 pct).

Simulated carburization for each condition was conducted at 930 °C (as shown for both conditions in Figure 3.1) for times of 0, 30, and 328 min in an atmosphere of air. These times were chosen to include a baseline of only heating the steel to carburization temperature (0 min), a time where AGG may have initiated (30 min), and a time meant to simulate a full-length carburization cycle (328 min). After the respective time in the furnace was reached, the sample was immediately water quenched so that the prior austenite grain boundaries (PAGBs) could be observed through etching.

The simulated carburization at 930 °C is intended to austenitize the alloys. Steel fully austenitizes above its Ac_3 temperature, which, using Equation 3.1, was calculated to be approximately 835 °C for both of these alloys [12]:

$$Ac_3=910-203\sqrt{C}-15.2Ni+44.7Si+104V+31.5Mo+13.1W \quad (3.1)$$

where *C*, *Ni*, *Si*, *V*, *Mo*, and *W* each represent the respective wt pct of these elements in the alloy. As simulated carburization occurs at 930 °C, it is assured that the samples fully austenitize prior to being quenched. Due to the hardenability of the alloy and relatively small cross-sections used in the study, martensite is expected after quenching, thus preserving the PAGBs.

Each distinct combination of CR and WR underwent simulated carburization. Each one of these conditions then underwent microstructural analysis as outlined in Section 3.3. Table 3.2 summarizes the thermomechanical conditions that this project is investigating.

Table 3.2 Experimental Conditions Being Evaluated

Composition	Warm Reduction (pct)	Cold Reduction (pct)	Simulated Carburization Time (min)
4121Al	None (As-forged)	0	0
4121Nb	0	5	30
-	10	10	328
-	25	25	-
-	50	-	-

3.3 Microstructure Analysis

Metallographic samples were taken from each distinct bar of steel prior to any cold work or simulated carburization for initial microstructure analysis. Each experimental condition underwent microstructural analysis after simulated carburization as well, so the influence of WR, CR, and simulated carburization time could be examined. Metallographic observation was performed with light optical microscopy after polishing to 1 μm and etching with a picral etchant at 65 °C for 15-20 s. Picral etchant (280 mL deionized water, 8.5 mL Teepol^{TM}, 2 mL HCl, and 5.5 g picric acid crystals) was used to outline the PAGBs to determine the PAGS and to evaluate the degree of AGG [12].

Five micrographs per condition were used to determine an average PAGS using micrographs taken on an Olympus® DSX 500 Digital Microscope. The average PAGS was calculated using the line-intercept method with five lines per image and dividing their length by the number of grain boundaries they intercept. AGG was measured by assuming each intercept length represents grain diameter and that each grain is perfectly circular. Grains with line-*-intercepts ≥30 μm were classified as "abnormal" and their total area was divided over the total grain area calculated using these assumptions.

3.4 Thermodynamic Modeling

As a supplement to experimental results, the commercially-available equilibrium software Thermo-Calc was utilized to model the volume fractions and phase compositions of the two alloys. The package used was Steels and Fe-alloys v12.0 (TCFE12, MOBFE7). The total phase equilibrium within the temperature range of interest (900-1230 °C) was obtained for both alloys, with phases ALN_B4 and FCC_A1#2 specifically being analyzed for the volume fractions of AlN and Nb(C,N), respectively.

3.5 Carbon Extraction Replication and TEM

To quantify the effects of heat treatment on the precipitate development of these two alloys, carbon extraction replicas (CER) were produced in order to observe the precipitate distribution, size, and composition in an FEI Tecnai T12 Transmission Electron Microscope (TEM). CER were produced by polishing mounted samples down to 1 μm and submerging them in 4 pct Nital solution (96 mL methanol, 4 mL nitric acid) for 1 minute. After etching, the surface of the mount is covered with tape such that only the metal surface is exposed. These taped and

etched samples were carbon coated. A grid of squares approximately 1 mm^2 were cut into the metal surface with a sharp knife after removing the tape. These samples were submerged in 4 pct Nital until the carbon layer began to float off the sample. In some cases, samples were then submerged in DI water, resulting in the carbon layer fully lifting off the sample. As AlN is water soluble, some AlN precipitates could have dissolved in samples exposed to DI water, so resultant CER samples may have had lower quantities of AlN than expected. The 1 mm^2 squares were collected with copper grids and allowed to dry before being imaged with bright field imaging in TEM. EDS was performed on sites with visible precipitates in TEM, though the beam size was too large to collect elemental compositions of the precipitates at most sites.

CHAPTER 4: RESULTS AND DISCUSSION

This chapter presents results obtained from the outlined experimental procedures. The effects of warm reduction on microstructural evolution in comparison to cold reduction are discussed, as well as the development of precipitates within the two alloys and how they may have affected microstructural development.

4.1 Microstructure and Grain Size Evolution

This section discusses the effects of WR and CR on PAGS and AGG of 4121Al and 4121Nb after various heat treatment times, as well as the differences in final microstructures between the two alloys.

4.1.1 Initial Microstructure

As discussed in Chapter 3.2, the temperatures that 4121Al and 4121Nb are exposed to during WR (900 °C) are above the Ac_3 temperatures of both alloys (835 °C) but below the T_{NR} temperature of 4121Nb (1027 °C).

Light optical micrographs of the microstructures for each condition prior to simulated carburization are shown in Figure 4.1. Microconstituents of what appear to be pearlite and/or bainite were present in a ferrite matrix in each microstructure. The as-forged samples were distinct from those that were warm reduced because they were air-cooled, resulting in a faster cooling rate and bainite as the most prominent secondary microconstituent rather than pearlite. The as-forged 4121Nb, shown in Figure 4.1(f), had a higher volume fraction of secondary microconstituents (bainite) compared to the as-forged 4121Al, shown in Figure 4.1(a).

As WR percentage increased, the average ferrite grain size decreased proportionally. This change in grain size with WR can be seen more clearly in Figure 4.2 and Figure 4.3. For example, Figure 4.2(a) and (c) show light optical micrographs of the microstructures of 4121Al after WR of 0 pct and 50 pct, respectively. The 50 pct WR condition was visibly refined compared to the non-worked condition.

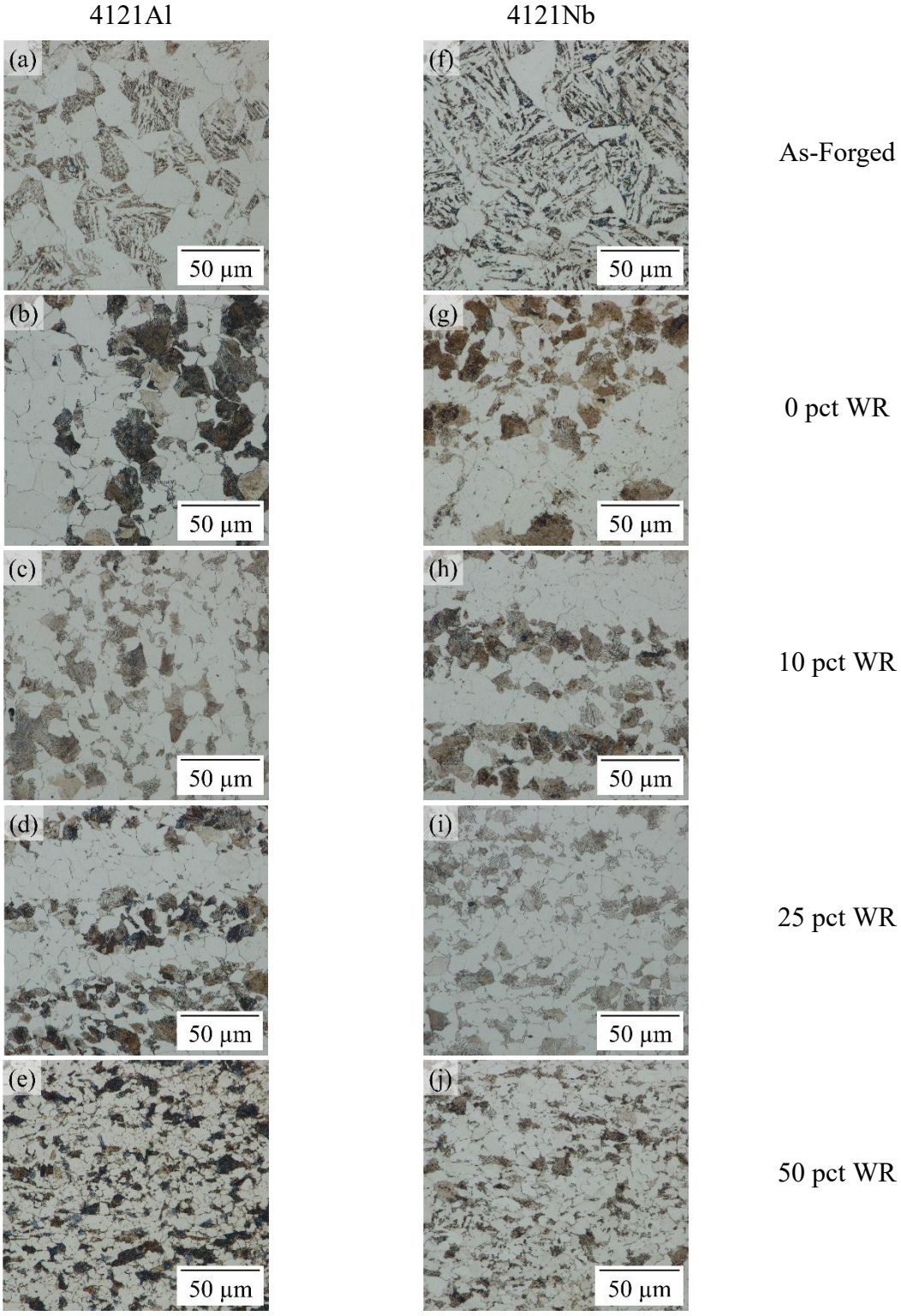


Figure 4.1 4121Al initial microstructures for (a) as-forged, (b) 0 pct WR, (c) 10 pct WR, (d) 25 pct WR, and (e) 50 pct WR conditions and 4121Nb initial microstructures for (f) as-forged, (g) 0 pct WR, (h) 10 pct WR, (i) 25 pct WR, and (j) 50 pct WR conditions, 2 pct nital etch. Olympus® DSX500 light optical micrographs.

After simulated carburization, the PAGS of each condition was similarly refined in proportion to the amount of WR done, exemplified by Figure 4.2(b) and (d). This refinement is likely a result of the difference in total grain boundary area in the initial ferrite-pearlite microstructures of the two conditions. The 50 pct WR condition had a larger total grain boundary area with its more refined microstructure, leading to a higher amount of austenite nucleation sites, resulting in smaller austenite grains on average than in conditions that were subjected to less warm reduction.

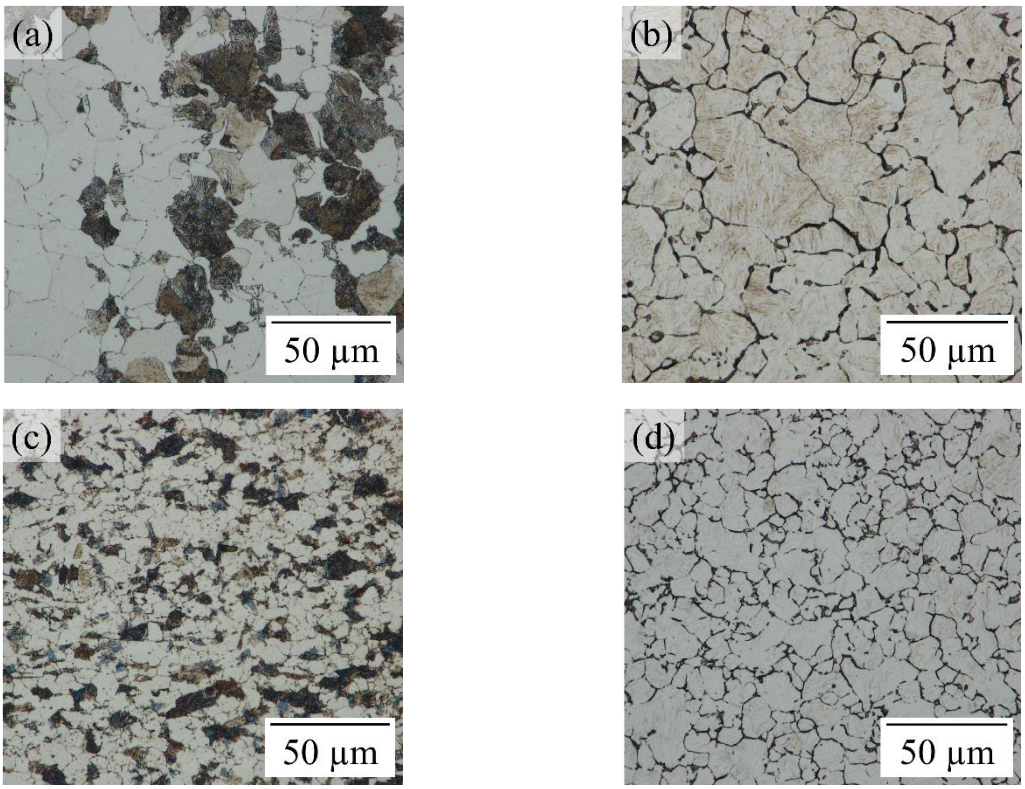


Figure 4.2 Microstructure of 4121Al after (a) 0 pct WR and (b) subsequent simulated carburization at 930 °C for 328 min and (c) 50 pct WR and (d) subsequent simulated carburization at 930 °C for 328 min. 2 pct nital etch was used for (a) and (c), picral etch for (b) and (d). Olympus® DSX500 light optical micrographs.

The refining effect of warm reduction on the initial microstructure was similarly observed in 4121Nb, as shown in Figure 4.3. Figure 4.3 displays the microstructures of 4121Nb after 0 and 50 pct WR and subsequent simulated carburization. Refinement of the initial pearlitic and ferritic microstructure with the application of warm reduction is shown between Figure 4.3(a) and (c). After simulated carburization, the refinement due to warm reduction can be seen in the resultant

microstructures in Figure 4.3(b) and (d), with the size of the PAGS appearing to be proportional to the size scale of the initial microstructure.

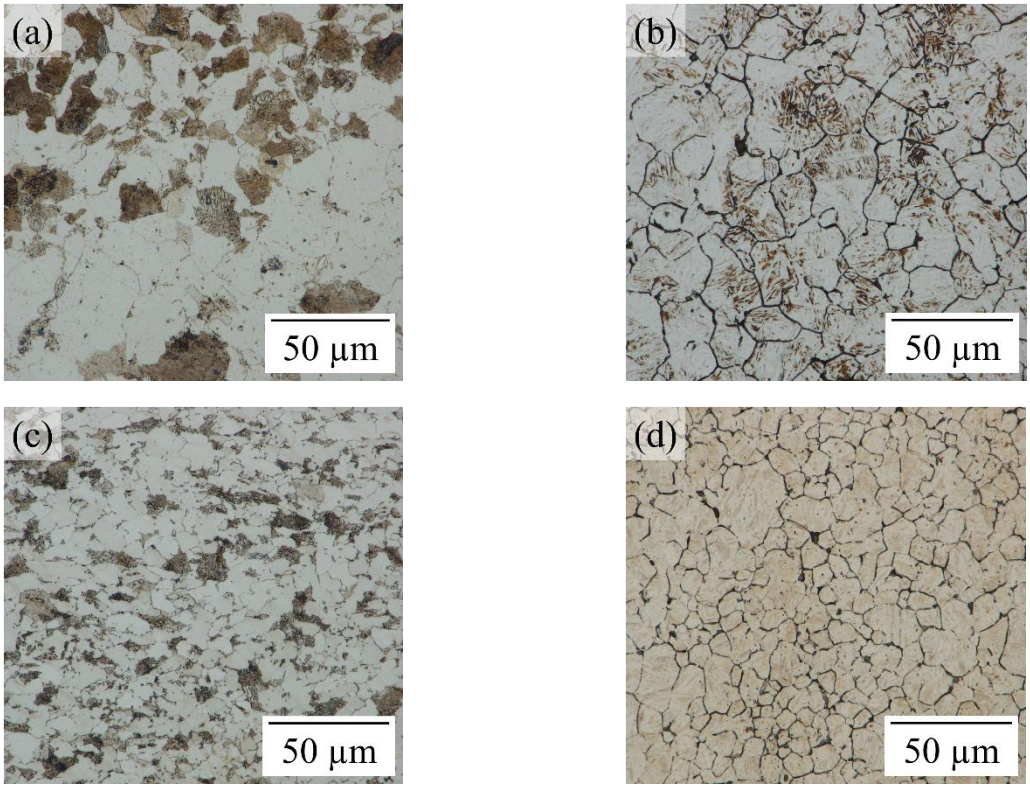


Figure 4.3 Microstructure of 4121Nb after (a) 0 pct WR and (b) subsequent simulated carburization at 930 °C for 328 min and (c) 50 pct WR and (d) subsequent simulated carburization at 930 °C for 328 min. 2 pct nital etch was used for (a) and (c), picral etch for (b) and (d). Olympus® DSX500 light optical micrographs.

4.1.2 Effects of Warm and Cold Reduction on PAGS and AGG

Figure 4.4 and Figure 4.5 show micrographs of 4121Al and 4121Nb, respectively, for each WR condition after being subjected to no CR (0 pct CR) and then simulated carburization. The micrographs of both alloys after varying degrees of CR can be found in Appendix A. These microstructures show the prior austenite grains of the steels after heat treatment, quenching, and subsequent etching with picral solution. The average intercept length (AIL) was measured for each condition. Because average PAGS is proportional to AIL, the results and discussion will refer to the trends with respect to PAGS based on the observed changes in AIL.

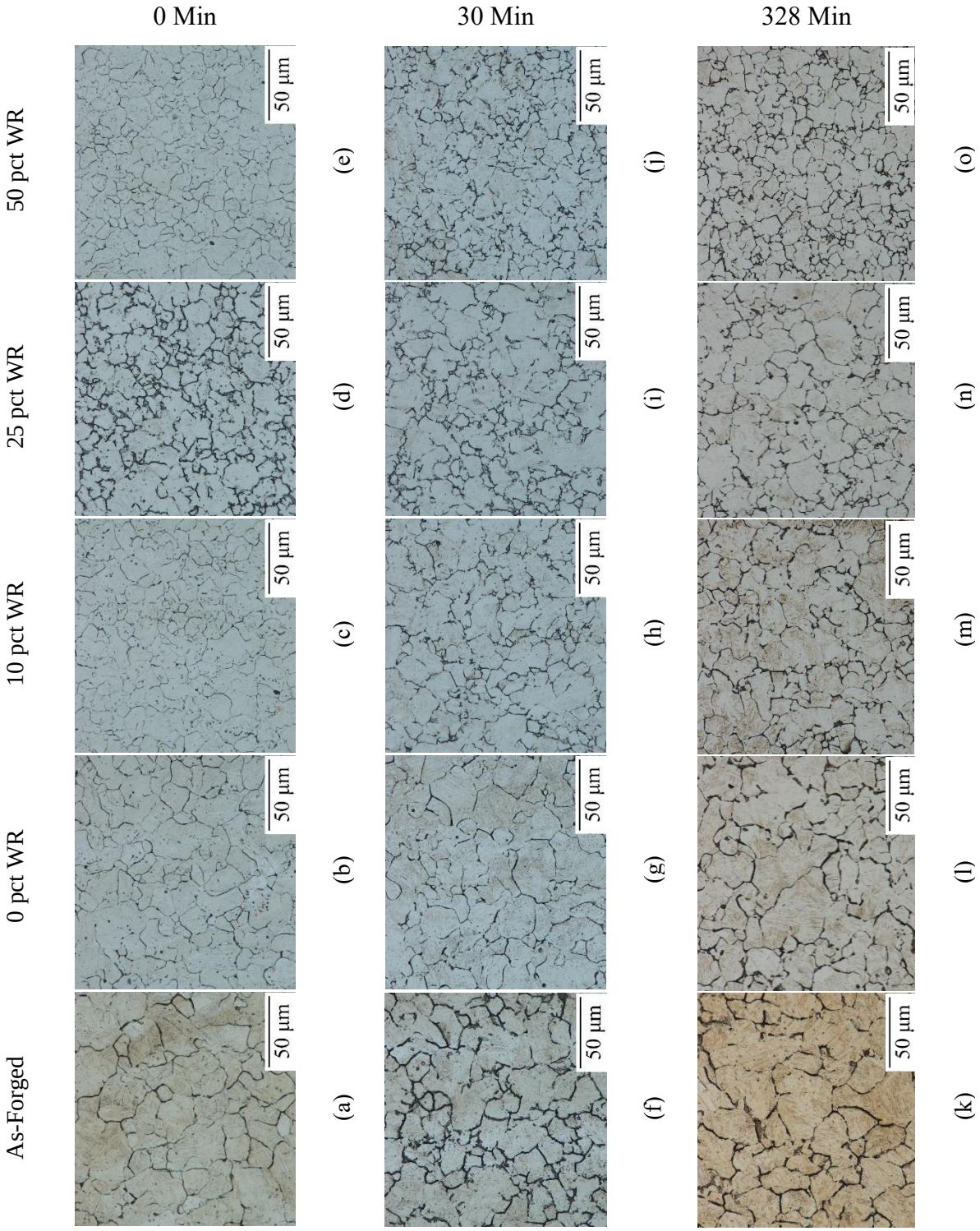


Figure 4.4 Micrographs of each WR condition and the as-forged condition of 4121Al after 0 pct CR and picral etching at 1664x magnification. (a)-(e) depict the 0 min dwell time condition, (f)-(j) depict the 30 min dwell time condition, and (k)-(o) depict the 328 min dwell time condition. Olympus® DSX500 light optical micrographs.

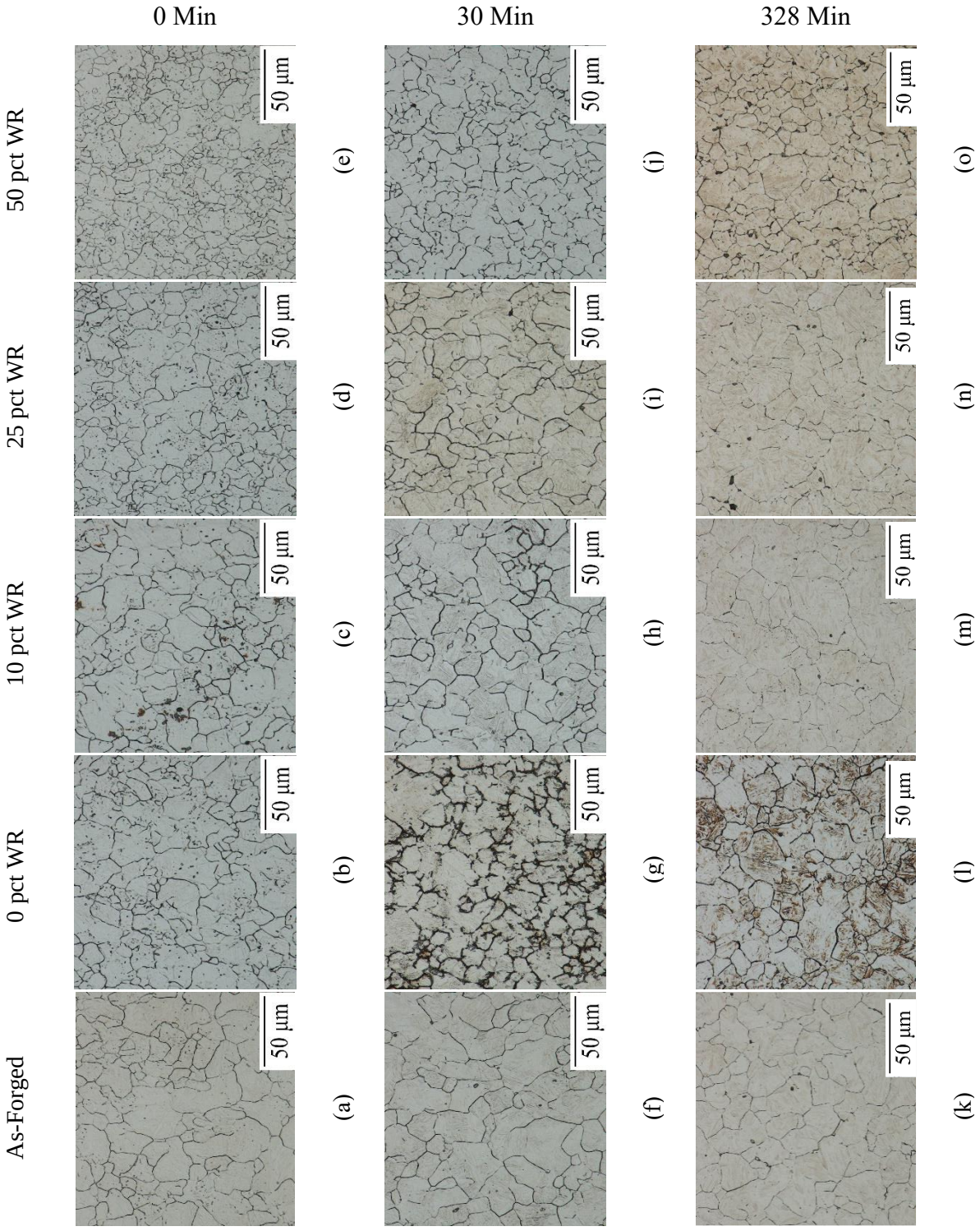


Figure 4.5 Micrographs of each WR condition and the as-forged condition of 4121Nb after 0 pct CR and picral etching at 1664x magnification. (a)-(e) depict the 0 min dwell time condition, (f)-(j) depict the 30 min dwell time condition, and (k)-(o) depict the 328 min dwell time condition. Olympus® DSX500 light optical micrographs.

The average PAGS consistently increased with hold time, which was expected due to the time dependence of grain coarsening. The average PAGS also consistently decreased in proportion to the amount of WR, similar to the refinement in the initial WR microstructures. The 0 pct WR condition, for a given hold time, had the coarsest average PAGS, and the 50 pct WR condition had the finest average PAGS. AGG is visible in the micrographs of the 0, 10, and 25 pct WR conditions of both alloys for all hold times. Some abnormal grains can also be observed in 4121Nb after 50 pct WR and 328 min of simulated carburization, shown in Figure 4.5(o). However, on average, AGG was observed most frequently in the 0, 10, and 25 pct WR conditions. The as-forged conditions of both alloys for all hold times had large average PAGS, which was likely a result of these conditions having coarser relative initial microstructures. Figures comparing micrographs of further conditions can be found in Appendix A.

Figure 4.6 and Figure 4.7 show 3D surface plots of AIL with respect to WR and CR for 4121Al and 4121Nb, respectively. These plots are in agreement with microstructural observations in showing that average PAGS of both alloys decreased as both WR and CR increased, refining the microstructure roughly the same amount proportional to percent reduction. The refinement due to WR was likely a result of the increase in nucleation sites from the increase in grain boundary area. The refinement due to CR may be due to plastic deformation increasing the amount of deformation substructure within the microstructure, also creating more nucleation sites. In both alloys, the average PAGS also increases with hold time across all conditions.

Differences in average PAGS trends can also be observed between the two alloys. Figure 4.6 shows that, after each hold time, there was a noticeable amount of grain refinement after either only 10 pct WR or 5 pct CR in 4121Al, the lowest increments of work for each respective reduction method. Because of this noticeable decrease in average PAGS after any amount of work, the most notable peak after any hold time in Figure 4.6 is after 0 pct WR+0 pct CR. In contrast, the average PAGS of 4121Nb is also noticeably refined by 5 pct CR but actually increases after 10 pct WR, as can be seen in Figure 4.7. This trend is less prominent after the 328 min hold time, as the drop in average PAGS is not as sharp after this hold time, but Figure 4.7(a) and (b) show a clear elevated region of higher average PAGS across the 0 pct CR conditions.

The condition with the largest average PAGS in each hold time of 4121Nb is after 10 pct WR+0 pct CR. Overall, the 4121Nb has a slightly finer average PAGS across a majority of conditions for the 0 and 30 minute hold times and coarser average PAGS after 328 min.

Cold reduction appeared to reduce the amount of microstructural refinement associated with WR. Figure 4.8 shows average PAGS with respect to WR of both alloys after 0 pct CR and 10 pct CR. In the 0 pct CR condition (Figure 4.8(a) and (c)), for all hold times, the average PAGS decreases consistently as WR increases with the exception of 4121Nb after 10 pct WR, where the average PAGS increases slightly for all hold times. Figure 4.8(b) and (d) show that, after 10 pct CR, the average PAGS decreases less as WR increases between 0 and 25 pct WR. After 50 pct WR, the average PAGS of both alloys for all hold times decreases to the same degree as in the 0 pct CR condition. In both alloys subjected to cold reduction, increasing hold time appears to make this effect more pronounced.

Relative to the 0 pct CR conditions of the same hold times, the average PAGS of the 0 min hold times decrease less between 0 and 25 pct WR, the average PAGS of the 30 min hold times decrease even less between 0 and 25 pct WR, and the average PAGS of the 328 min hold times change very little between 0 and 25 pct WR. The 0 min hold time of 4121Nb appeared affected more by the addition of CR than the same hold time in 4121Al. After the 30 and 328 minute hold times, these trends were the same with respect to each alloy after any amount of CR.

The reason why CR appears to reduce refinement done by WR could be due to the deformation substructures created by cold reduction being more effective austenite nucleation sites than the increased boundary and phase interface area associated with warm reduction, resulting in austenite nucleation and resultant PAGS being dependent on degree of CR, rather than WR. The decrease in average PAGS after 50 pct WR may be due to the grain and phase boundary area increasing to such a degree that these sites become more critical to the resultant austenite grain size.

2D plots of average PAGS and degree of AGG of both alloys for each WR and CR condition can be found in Appendix B.

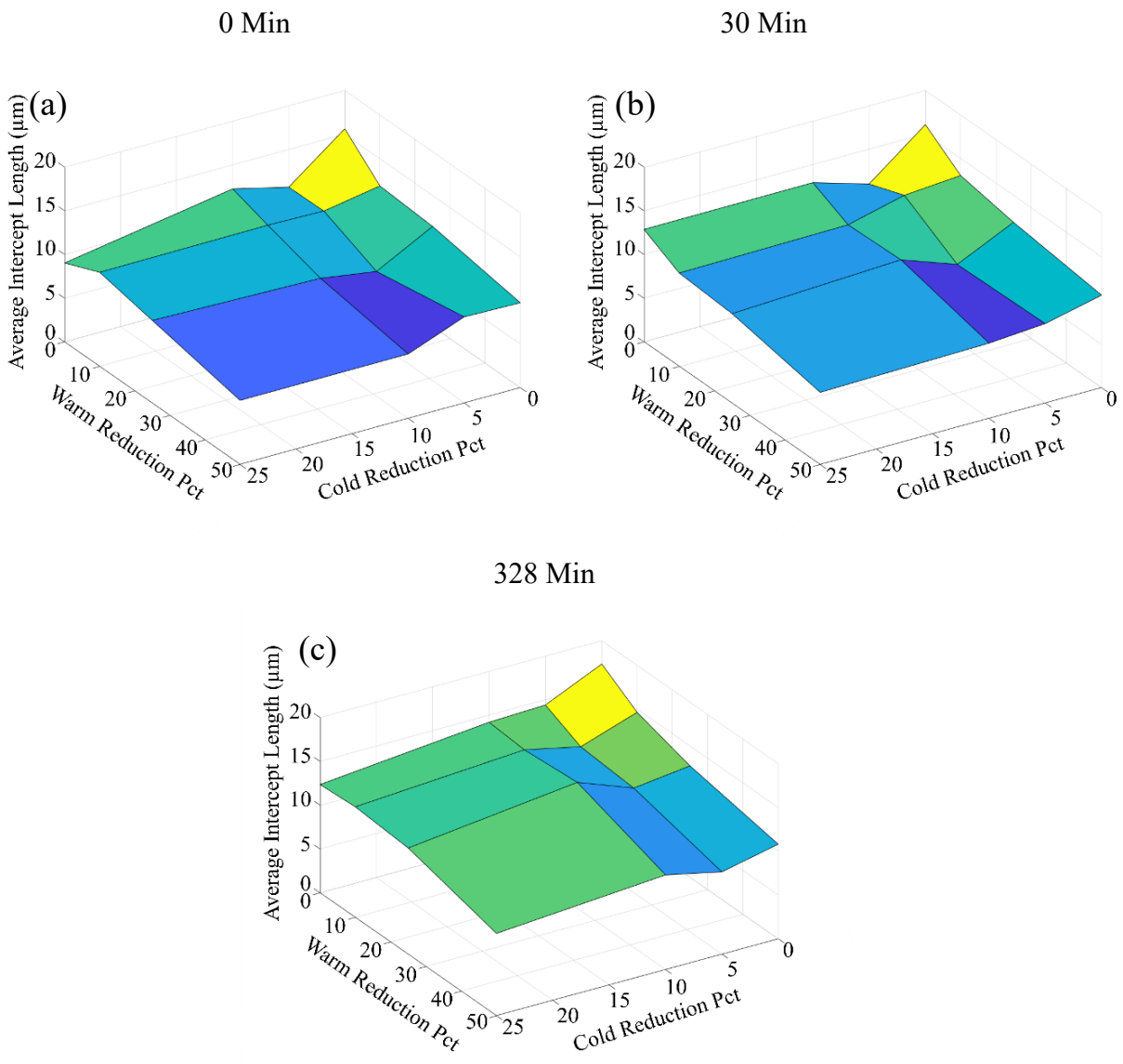


Figure 4.6 3D surface plots that depict the average intercept length with respect to both WR and CR for 4121Al after (a) 0 min, (b) 30 min, and (c) 328 min. The color of the surface varies according to the heights specified by AIL, with lighter such as yellow being high AIL and darker colors such as blue being lower AIL.

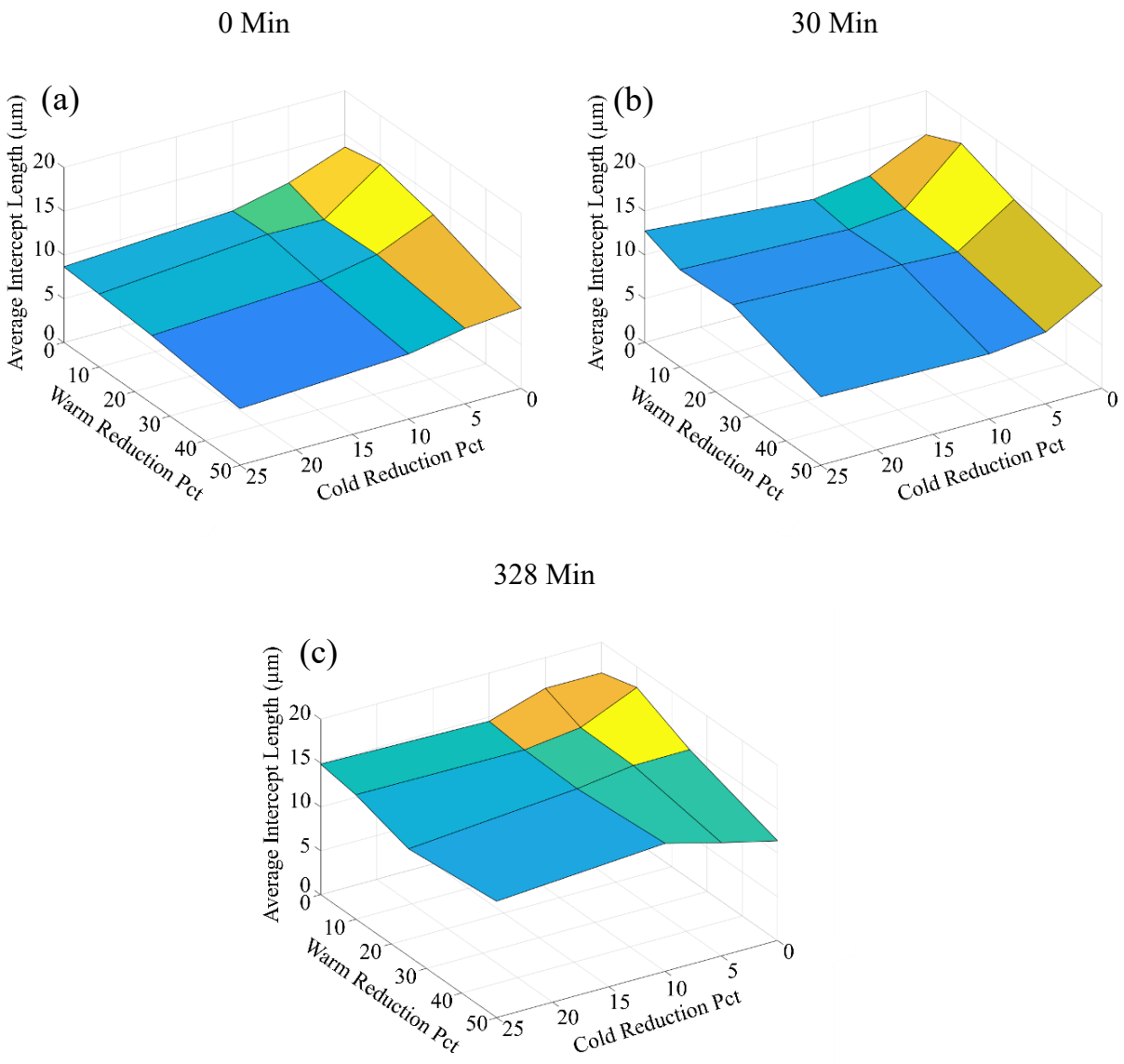


Figure 4.7 3D surface plots that depict the average intercept length with respect to both WR and CR for 4121Nb after (a) 0 min, (b) 30 min, and (c) 328 min. The color of the surface varies according to the heights specified by AIL, with lighter such as yellow being high AIL and darker colors such as blue being lower AIL.

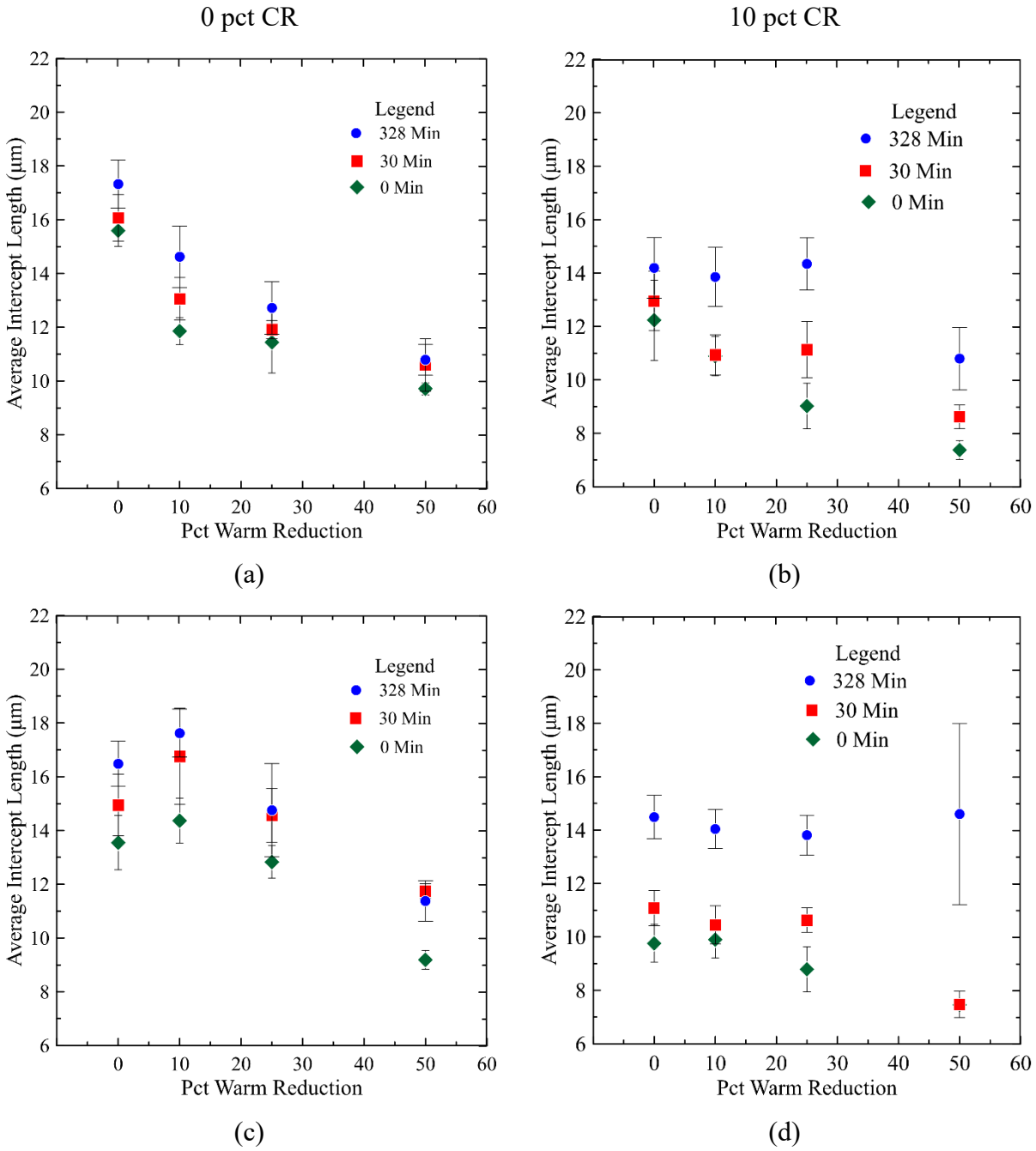


Figure 4.8 (a) AIL of 4121Al after 0 pct CR and (b) 10 pct CR with respect to WR and (c)AIL of 4121Nb after 0 pct CR and (d) 10 pct CR with respect to WR.

Figure 4.9 and Figure 4.10 depict AGG normalized over total grain area for 4121Al and 4121Nb, respectively. AGG was present in both alloys in most WR conditions. AGG generally decreased with increased WR and CR, similarly to PAGS. Some distinctions between AGG of 4121Al and 4121Nb are similar to those observed in average PAGS. After the 0 and 30 min hold times, the degree of AGG closely matched the same trends observed for average PAGS for the

same hold times for both alloys. In 4121Al, AGG peaks at 0 pct WR+ 0 pct CR, decreases relatively quickly after 5 pct CR and 10 pct WR, and decreases gradually as CR and WR increase. In 4121Nb, there are regions of relatively high AGG in the 0 pct CR conditions which decrease relatively quickly after 5 pct CR, followed by a gradual decrease in AGG as WR and CR increase.

There are exceptions to this gradual decrease in AGG after 30 min hold times in both alloys. AGG in 4121Al increases after 10 pct WR+5 pct CR and AGG in 4121Nb increases after 0 pct WR+25 pct CR. After 328 min, however, there were more distinct differences in AGG between 4121Al and 4121Nb. 4121Al, as shown in Figure 4.9(c), has distinct peaks of AGG that are aberrant from the average PAGS trends of the same hold time seen in Figure 4.6(c).

4121Nb, after 328 min, has a small peak of AGG at low percentages of work and changed relatively little across the different WR and CR conditions, still matching the trends in average PAGS with peaks at 0 pct WR+25 pct CR and 50 pct WR+10 pct CR present in Figure 4.10(c). Besides these peaks, AGG decreases with WR and CR. Figure 4.10(c) shows that 4121Nb had the highest amount of AGG on average after the 328 min hold time compared to any other condition between the two alloys. The exact values used to plot Figure 4.6-Figure 4.10 can be found in Appendix C.

To compare the effects of warm reduction vs. cold reduction on PAGS and AGG, Figure 4.11 depicts plots of average PAGS data from both this work and from data obtained by Lee *et al.* in their work. Lee *et al.* observed a distinct peak in both average PAGS and AGG after 10 pct CR for the same alloys; no warm work was performed in this study. This peak is shown in Figure 4.11(a) and (c) [5]. The data from this work features average PAGS of both alloys after being subjected to 50 pct WR and a range of CR, as it was the only WR condition that showed a trend similar to that observed by Lee *et al.* This data is plotted in Figure 4.11(b) and (d). In both data sets, for most CR conditions, 4121Nb has a coarser grain size than 4121Al.

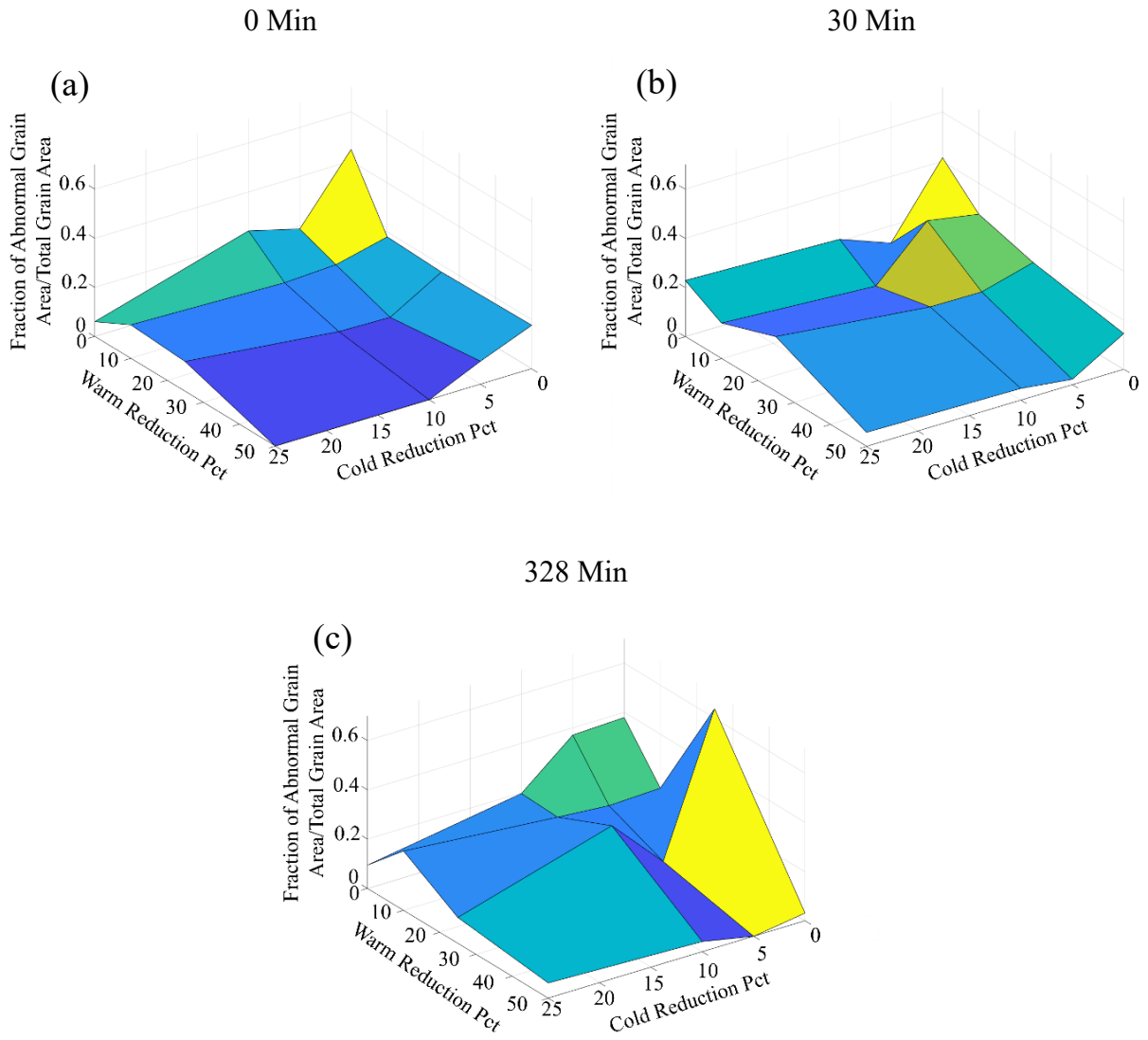


Figure 4.9 3D surface plots that depict the number density of abnormally grown grains with respect to both WR and CR for 4121Al after (a) 0 min, (b) 30 min, and (c) 328 min. The color of the surface varies according to the heights specified by AIL, with lighter such as yellow being high AIL and darker colors such as blue being lower AIL.

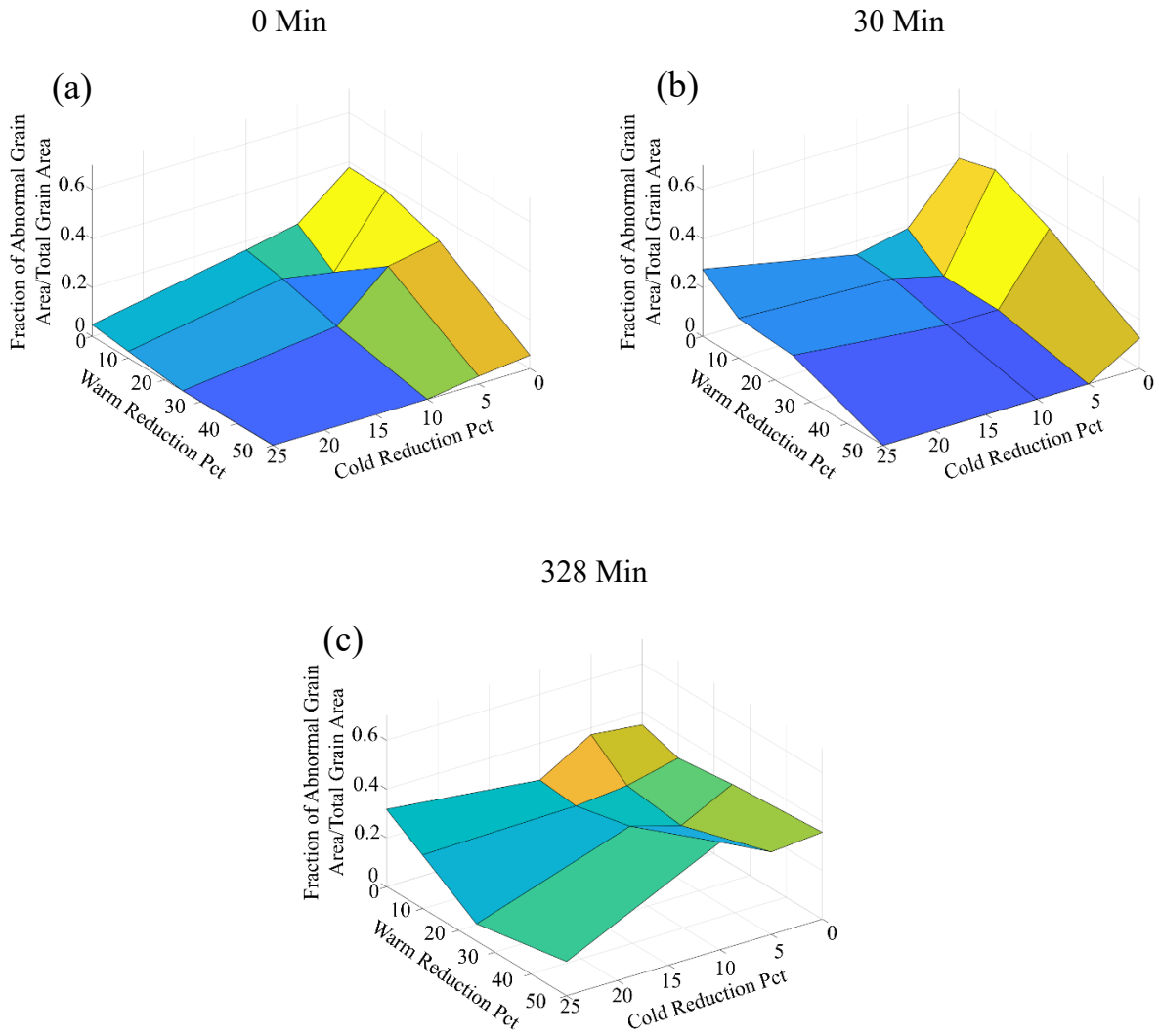


Figure 4.10 3D surface plots that depict the number density of abnormally grown grains with respect to both WR and CR for 4121Nb after (a) 0 min, (b) 30 min, and (c) 328 min. The color of the surface varies according to the heights specified by AIL, with lighter such as yellow being high AIL and darker colors such as blue being lower AIL.

Figure 4.11(b) and (d) show that when subjected to 50 pct WR and 328 min of simulated carburization, the average PAGS of both 4121Al and 4121Nb peak after 10 pct CR. The 0 and 30 min hold times, which were only conducted on the 10 pct CR condition in the work by Lee *et al.*, did not show the same trend as CR increased. As seen in Figure 4.11(b) and (d), grain refinement generally decreased with increased CR for the 0 and 30 min hold times.

In the work by Lee *et al.*, the initial thermomechanical pre-treatment history consisted of a subcritical anneal at 700 °C for three hours, 50 pct CR, and a second subcritical anneal at

700 °C for three hours prior to cold reduction ranging from 0-50 pct CR, and subsequent simulated carburization. This pre-treatment resulted in finer initial microstructures and finer resultant average PAGS than those in this work, which can be seen when comparing Figure 4.11(a) and (c) with Figure 4.11(b) and (d), respectively. Figure 4.12(a) shows the initial microstructure of 4121Nb after the second subcritical anneal in the work by Lee *et al.*, and Figure 4.12(b) shows the much coarser initial microstructure of 4121Nb after 0 pct WR from the current work.

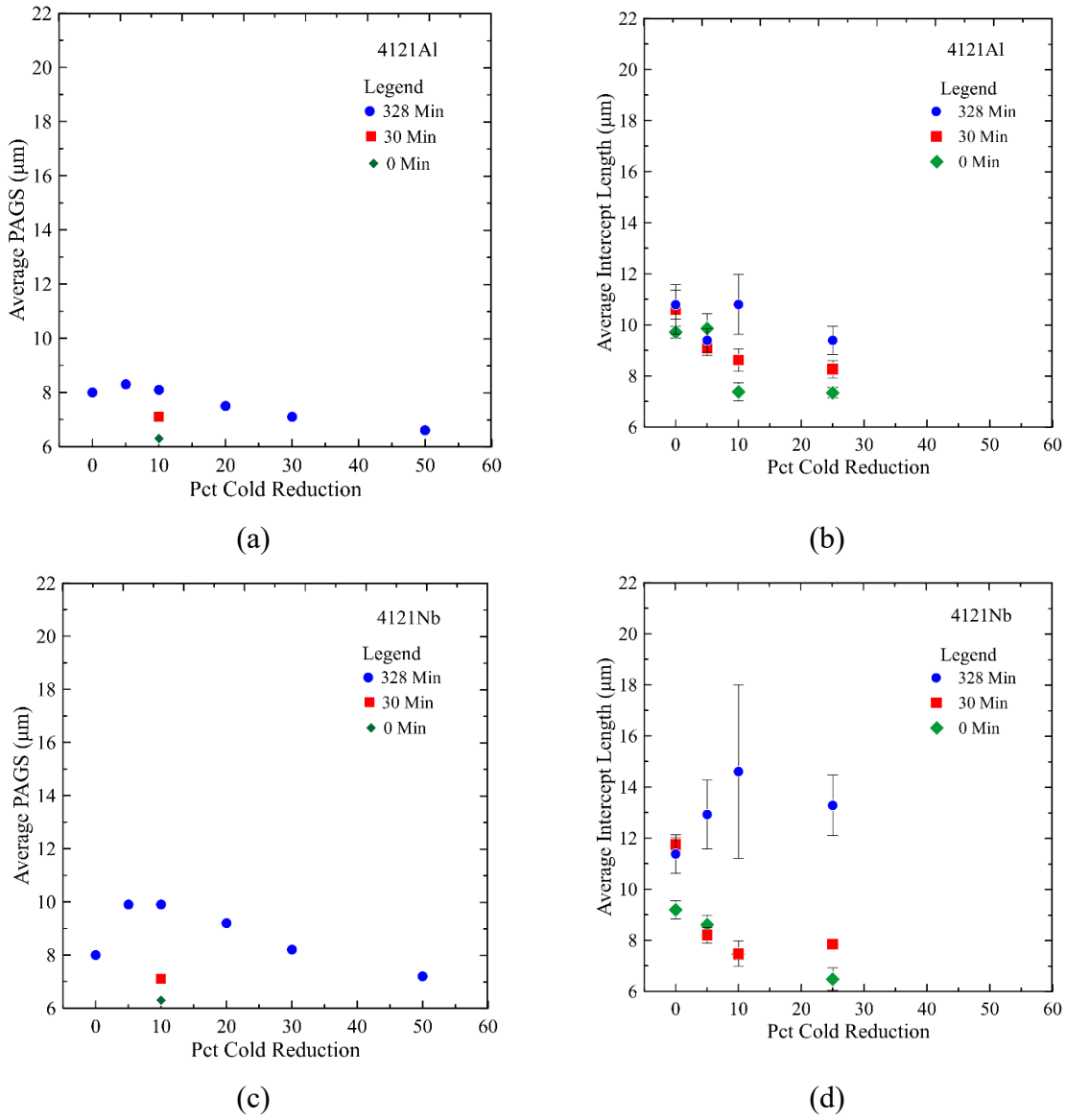


Figure 4.11 Comparison of (a) PAGS of 4121Al and (c) PAGS of 4121Nb observed by Lee *et al.* after simulated carburization with (b) AIL of 4121Al after 50 pct WR and (d) AIL of 4121Nb after 50 pct WR [35].

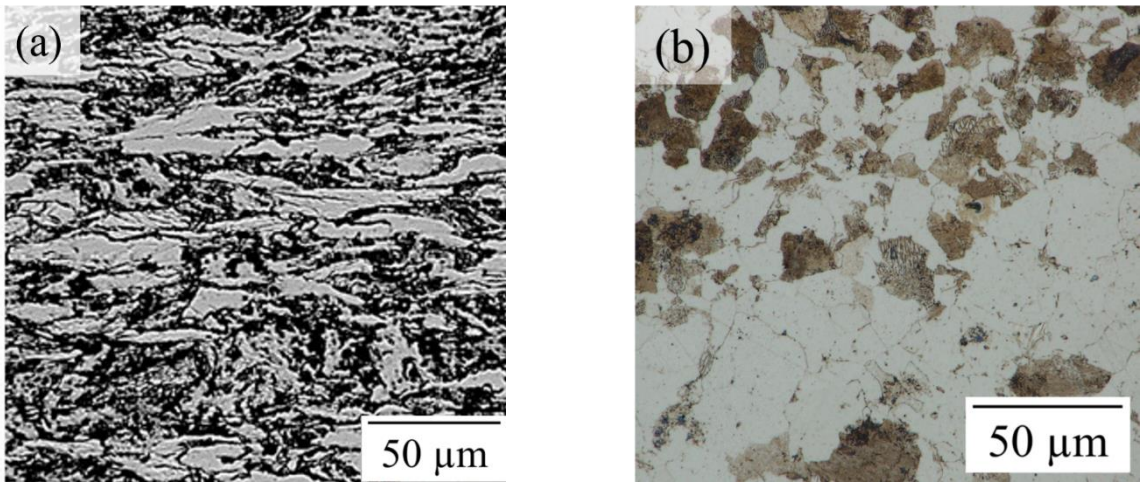


Figure 4.12 Comparison of the microstructures of 4121Nb after (a) the thermomechanical pre-treatment done by Lee *et al.* [5] and (b) 0 pct WR prior to cold reduction and simulated carburization in the current work.

4.2 Precipitate Size and Compositional Evolution

Thermo-Calc was utilized to predict the theoretical volume fraction and phase composition of precipitates in the two alloys. The simulation focused on AlN and Nb(C,N) precipitation. Mo is not predicted to be incorporated into precipitates until temperatures higher than those used in this work, so the Nb(C,N) carbonitride does not include Mo in its denotation (i.e. (Nb,Mo)(C,N)). It should be noted that in previous work by Seo *et al.* and Enloe *et al.*, similar heat treatment conditions resulted in Nb(C,N) precipitates with a small amount of Mo incorporation measured through EDS and atom probe tomography.

Figure 4.13 and Figure 4.14 depict precipitate volume fraction as a function of temperature in both alloys for AlN and Nb(C,N), respectively. The temperatures of primary concern in this work are 900 °C, 930 °C, and 1230 °C, which are, in order, the temperatures that warm reduction, simulated carburization, and initial homogenization take place. These specific temperatures are denoted in Figure 4.13 and Figure 4.14 by vertical dashed lines.

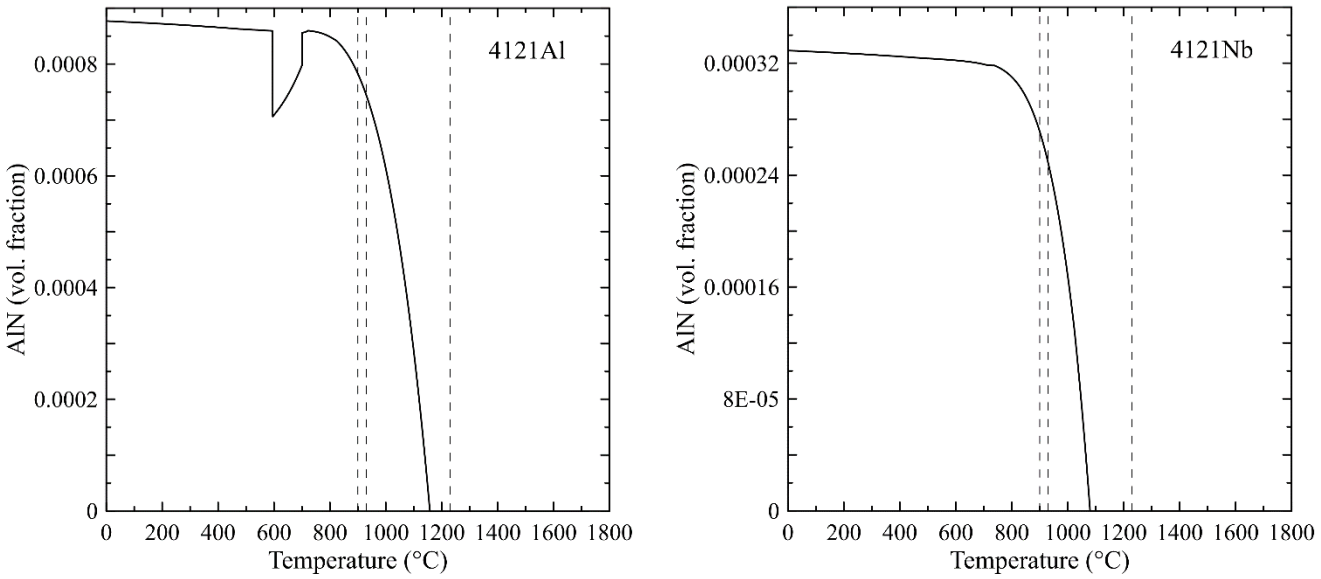
In 4121Al at 900 and 930 °C, there is a negligible difference in volume fraction of AlN, which is $7 \cdot 10^{-4}$ pct. This volume fraction of AlN in 4121Al is three times as much as is present in 4121Nb in the same temperature range. Nb(C,N) is negligible in 4121Al between 900 and 930 °C, but the volume fraction of Nb(C,N) in the same temperature range in 4121Nb is $4.5 \cdot 10^{-4}$ pct.

The phase composition with respect to temperature was predicted for Nb(C,N) and is shown in Figure 4.15. Because Nb(C,N) was negligible in 4121Al, Figure 4.15 only depicts the phase composition of Nb(C,N) in 4121Nb. Figure 4.15 shows that C is present in greater mass pct than N, likely due to the simultaneous development of AlN in the alloy additionally utilizing available N.

Using calculated values for diffusivity coefficients of Al and Nb in austenite based on models by Gómez *et al.* and San Martín *et al.*, assuming the interfacial energy of Al is the same as Nb (0.8 J/m^3) and identical initial particle radii, the coarsening rates of AlN and Nb(C,N) precipitates were approximated using the LSW equation. The factors used in this calculation can be found in Table 4.1. It should be acknowledged that the competing factors of interfacial energy and initial particle radii could significantly alter the coarsening rates, as increasing the interfacial energy proportionally increases coarsening rate and increasing the initial particle radius proportionally decreases the coarsening rate. At 930 °C, the ratio of coarsening rates of Nb(C,N) to AlN was $9.9 \cdot 10^{-4}$, meaning that Nb(C,N) coarsens many times slower than AlN. With a slower coarsening rate, it can be expected that Nb(C,N) precipitates will be finer and more stable than AlN precipitates in both alloys [2], [3].

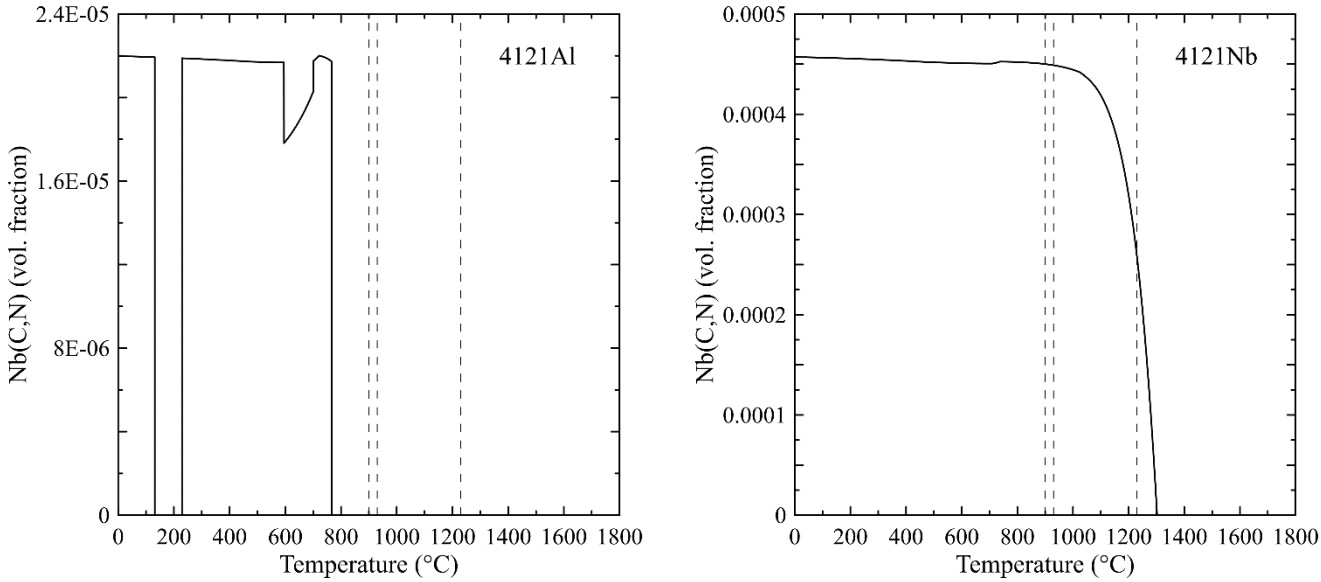
Table 4.1 Mean Lineal Intercept of Tempered Alloys Following Ramp to Specified Temperature, Soaking for Specified Time, and Water Quench

Element	T (K)	$\gamma_{P/M}$ (J/m^2)	[M] (%) at 930 °C	Ω (m^3/mol)	D_M (m^2/s) at 930 °C
Al	1203	0.8	$3.53 \cdot 10^{-3}$	$1.34 \cdot 10^{-5}$	$1.95 \cdot 10^{-16}$
Nb	1203	0.8	$7.41 \cdot 10^{-3}$	$1.25 \cdot 10^{-5}$	$1 \cdot 10^{-13}$



(a) (b)

Figure 4.13 Plots of volume fraction of AlN with respect to temperature in (a) 4121Al and (b) 4121Nb with vertical dashed lines denoting 900 ℃, 930 ℃, and 1230 ℃, respectively.



(a) (b)

Figure 4.14 Plots of volume fraction of Nb(C,N) with respect to temperature in (a) 4121Al and (b) 4121Nb with vertical dashed lines denoting 900 ℃, 930 ℃, and 1230 ℃, respectively.

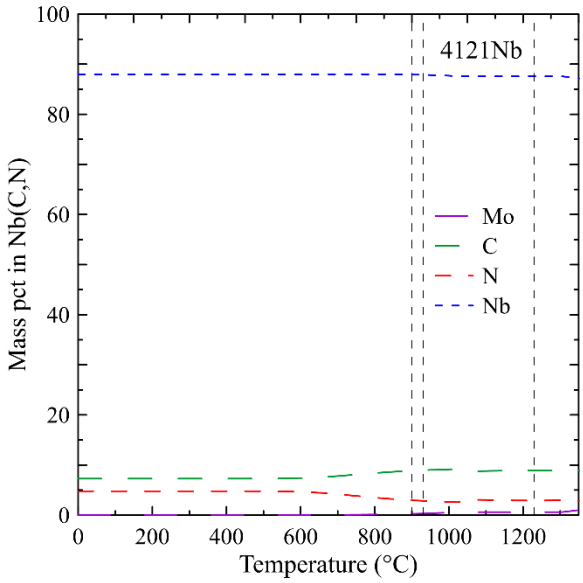
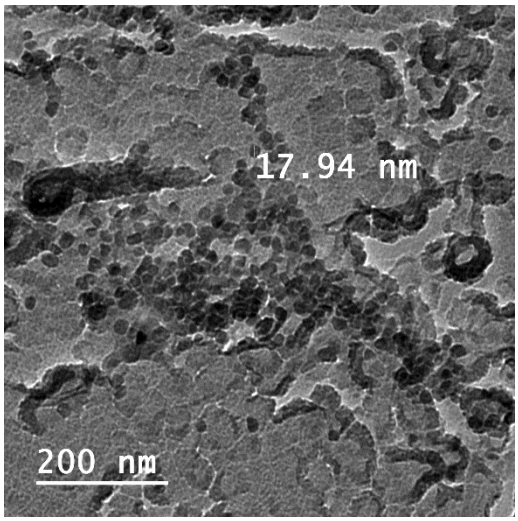


Figure 4.15 Plot showing respective mass percentage of Nb, Mo, N, and C in Nb(C,N) with respect to temperature in 4121Nb with vertical dashed lines denoting 900 °C, 930 °C, and 1230 °C, respectively.

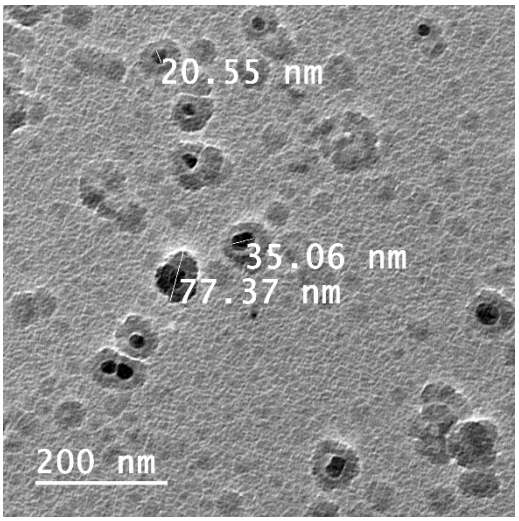
Precipitates were observed through carbon extraction replicas of the 0 pct WR+0 pct CR condition of each of the alloys after 328 min of carburization to compare precipitate size between 4121Al and 4121Nb. Figure 4.16 shows three sites with precipitates present in the 4121Al 0 pct WR+0 pct CR condition. Figure 4.16(a) shows a cluster of finer precipitates that are likely clustered as such due to the folding of the carbon film substrate the precipitates lie on, which was observed at several sites. Most precipitates at this site are under 20 nm in diameter. The two sites shown in Figure 4.16(b) and (c) are more similar to each other, and more representative of the majority of precipitate sites observed in TEM. Precipitates at these sites were coarser in general, reaching diameters in excess of 70 nm, with a wide range of diameters in between 20 nm and 70 nm. All the precipitates observed in 4121Al are likely AlN due to the relatively low amount of Nb in 4121Al and the negligible amount of Nb(C,N) predicted to be present in the alloy.

Figure 4.17 shows three sites with precipitates in 4121Nb 0 pct WR+0 pct CR. The distribution of precipitate sizes in 4121Nb is more distinct, with the most commonly observed sizes being relatively fine (<15 nm in diameter) with some larger particles also present. As discussed, Nb(C,N) precipitates are predicted to coarsen more slowly than AlN, which would suggest that the fine precipitates are likely Nb(C,N), though Nb was not picked up by EDS. The larger precipitates are likely AlN as Thermo-Calc estimated that some AlN should be present in

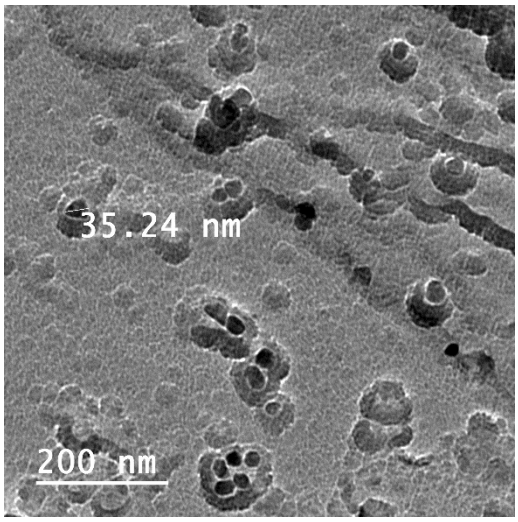
the 4121Nb alloy, and Al was detected in EDS spectra of each site. The range of sizes of AlN observed in 4121Al indicate that some of the fine precipitates seen in 4121Nb are likely AlN as well.



(a)

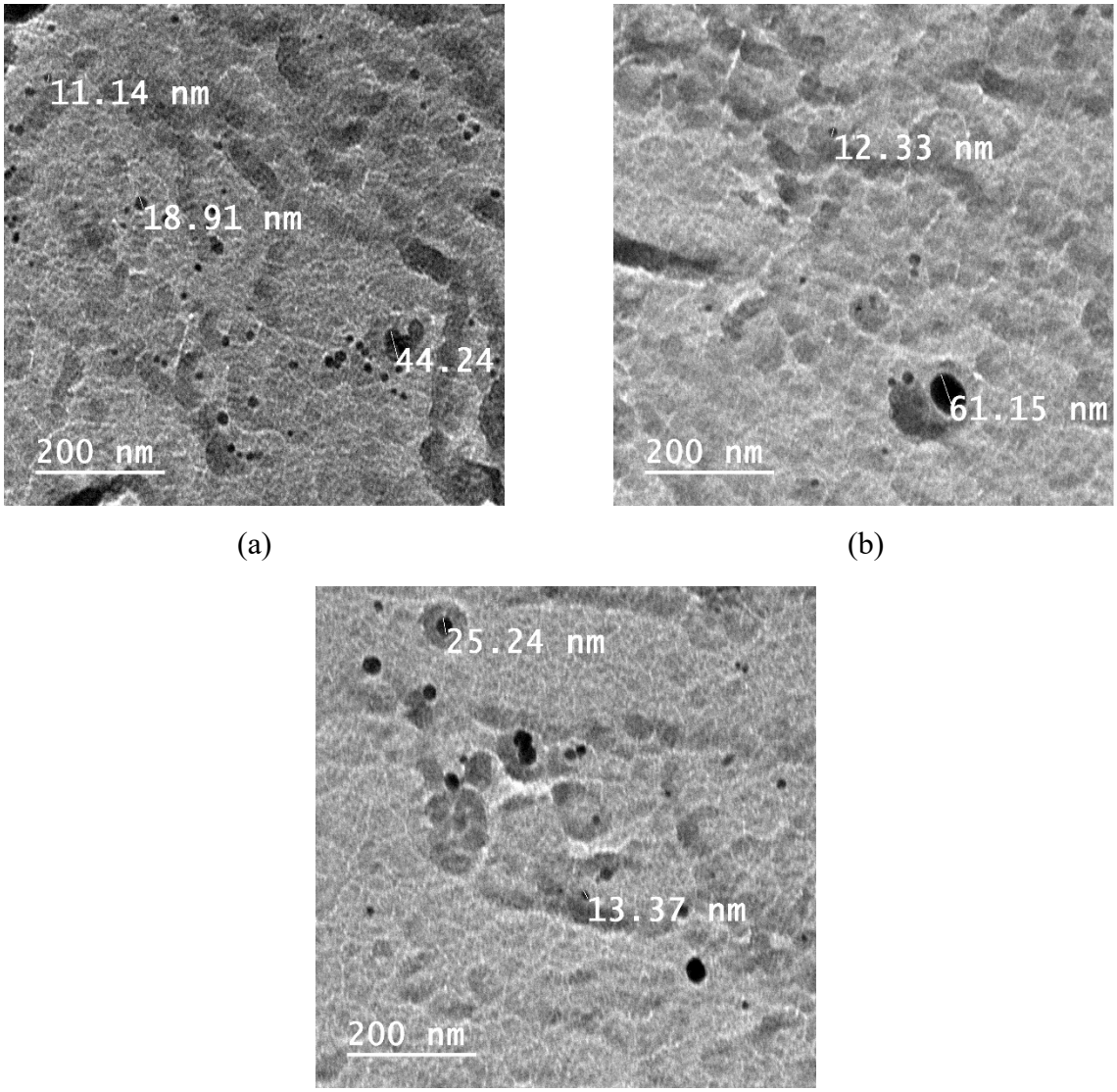


(b)



(c)

Figure 4.16 CER sites with precipitates present in 0 pct WR+0 pct CR 4121Al at 30 kx magnification. Bright field images taken with FEI Tecnai T12 Transmission Electron Microscope.



(a) (b)

(c)

Figure 4.17 CER sites with precipitates present in 0 pct WR+0 pct CR 4121Nb at 30 kx magnification. Bright field images taken with FEI Tecnai T12 Transmission Electron Microscope.

Due to the relatively large spot size used for EDS compared to precipitate size, the only element picked up by EDS besides the copper of the CER grid was Al in a very small concentration. An example of these EDS spectra is shown in Figure 4.18.

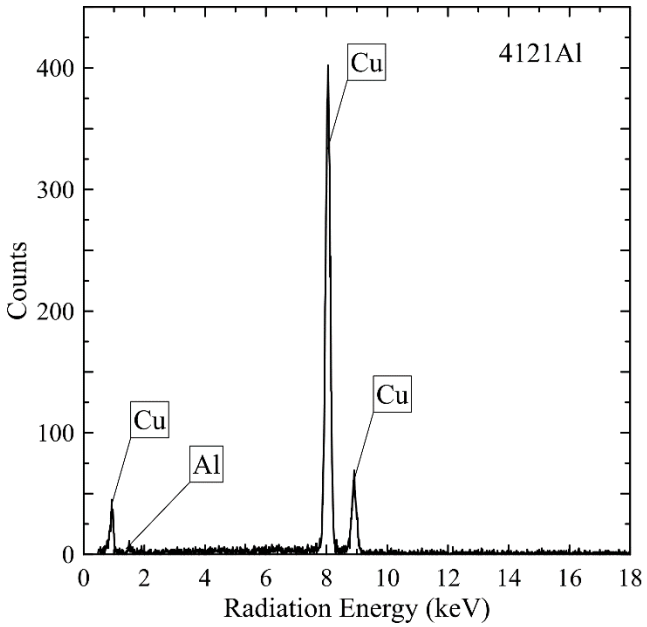


Figure 4.18 EDS spectrum of precipitate site shown in Figure 4.16(a).

The range of AlN precipitate diameters observed in 4121Al and possibly observed in 4121Nb indicate that these precipitates formed at different times and coarsened to varying degrees during the thermomechanical processing history. Assuming equilibrium volume fraction as predicted by Thermo-Calc, some Nb(C,N) likely formed during the homogenization step due to its high dissolution temperature (1300 °C). No AlN should have remained in either 4121Al or 4121Nb after homogenization due to its complete dissolution at 1150 °C. During the air-cooling after homogenization, however, both AlN and Nb(C,N) precipitates may have nucleated and coarsened, along with the Nb(C,N) that was retained after homogenization.

After the homogenizing step and air-cooling, both alloys were heated to 900 °C and soaked for 45 minutes. During the ramp up to soaking temperature, precipitate dissolution of AlN and to a lesser degree Nb(C,N) was possible to the equilibrium volume fraction. At the hold temperature, however, remaining precipitates may have coarsened further. During the slow-cooling that followed this step, coarsening of precipitates may have occurred in addition to additional precipitation of AlN and Nb(C,N).

Finally, the precipitates that were retained after forming and coarsening at different times and rates were subjected to simulated carburization. During the ramping process, there may have been coarsening and dissolution of these existing precipitates, dissolution of AlN being more

likely due to its lower dissolution temperature. The most likely retained precipitates to dissolve are those with the smallest radii at the initiation of heat treatment. Holding at 930 °C for simulated carburization would have likely resulted in further coarsening of existing precipitates. AlN, due to its higher coarsening rate and lower dissolution temperatures, would have been more likely to coarsen to a wide range of precipitate sizes as well as nucleate and dissolve at more points in the heat treatment process.

It has been observed in past work that a process known as reversion could also be occurring during certain intercritical steps in the heat treatment process. Reversion is the process by which dissolution and reprecipitation of very fine precipitates occurs at intercritical temperatures during slow heating. "Slow" in this instance being a heating rate ≤20 °C min^{-1}. The mechanism for dissolution in reversion has been attributed to changes in interphase interfacial free energies as a result of phase changes in the intercritical temperature region. Reversion could have resulted in Nb(C,N) and finer AlN precipitates that precipitated in the ferritic matrix dissolving below predicted equilibrium volume fractions in austenite once surpassing the Ac_1 temperature. Once austenite grains begin to nucleate, these precipitates would renucleate, resulting in a larger number of fine precipitates. Reversion could have occurred at any step of the process where austenitization takes place [20], [38], [39]. In the discussion above, reversion is not accounted for with respect to the formation and size of precipitates at various steps in the thermomechanical process history.

4.3 Analysis of the Effects of Thermomechanical Pretreatment and Microalloying Additions on Microstructural Evolution

This section further discusses the impacts of warm and cold reduction on microstructural evolution, as well as how these factors likely affected the precipitate evolution of both alloys.

Section 4.2 outlined the precipitate evolution of AlN and Nb(C,N) solely based on the effects of the heat treatment processing. As discussed in Chapters 2.3 and 2.4, strain induced precipitation occurs in strained microstructures similar to those in this work that were warm and cold worked. This strain induced precipitation accelerates the rate at which precipitates form, decreases their initial radius, and increases rate at which they coarsen and dissolve due to the smaller relative initial radius and introduction of strain energy. The rapid development of these fine precipitates which dissolve more easily has been shown to impact PAGS and AGG. These

fine precipitates effectively pin grain growth during austenitization, refining microstructures prior to their dissolution. As they begin to dissolve, though, the dissolution of these precipitates rapidly increases the number of abnormal grains [5], [29], [31], [32], [34].

The effects of strain induced precipitation are not clear from the results in this work, however. In regards to average PAGS and degree of AGG, the amount of work done was the clearest contributor to changes in microstructural development. At low amounts of work, microstructures had high amounts of AGG and a large average PAGS. At high amounts of work, the microstructures were refined and AGG was mitigated. For the same pre-treatment condition, the microalloying composition did not appear to change the PAGS or AGG noticeably besides some specific differences noted in Section 4.1. The lack of difference between the alloys would indicate that, for most processing conditions used in this work, the different compositions of 4121Al and 4121Nb did not significantly alter the final microstructure. One exception where composition did appear to make a distinct difference is in the degree of AGG observed after a 328 min hold time in 4121Nb, as AGG did not strictly decrease with increased WR and CR. This difference in resultant AGG would indicate that, after a full carburization cycle, the evolution of Nb(C,N) and its resultant grain pinning effects are more likely to initiate AGG than AlN subjected to the same heat treatment processing.

Warm reduction and cold reduction affected PAGS refinement to the same degree, which is notable due to the mechanisms of refinement being different. The effect of CR on the effectiveness of WR refinement, as discussed in Section 4.1., is notable as well. The degree of AGG decreased with WR and CR, unlike results produced by Lee *et al.*, who observed a peak at 10 pct CR [35].

CHAPTER 5: CONCLUSIONS

This chapter summarizes the main observations and interpretations of the results found in this work. These results show the effects of warm and cold reduction on PAGS and AGG during simulated carburization as well as the effects of composition on those same characteristics.

5.1 Effects of Warm and Cold Reduction on Microstructural Development

The initial microstructures observed after warm reduction were optically affected by warm reduction, with the average grain size being refined proportionally with warm work. This refinement resulted in finer PAGS as WR increased due to the increased grain boundary area that creates more sites for austenite nucleation during heating. Warm and cold reduction refined the microstructures to similar degrees.

This study can be compared to previous work, where cold reductions ranging from 0-50 pct were performed prior to simulated carburization and the highest measured average PAGS and AGG were at ~10 pct CR in 4121Al and 4121Nb. In this work, the average PAGS and AGG consistently decreased with respect to both WR and CR. Both warm and cold reduction were found to refine the microstructure. The conditions in this work that demonstrated the highest average PAGS and highest degree of AGG were those that were subjected to minimal work and simulated carburizing for 328 min. Cold reduction also decreased the effectiveness of refinement due to warm reduction in the range of 0-25 pct WR, with nucleation sites created by CR possibly being more preferable for nucleation than those created by WR. Because the most distinct difference between this work and that by Lee *et al.* is in the initial thermomechanical pre-treatments, it is possible that the thermomechanical history impacted propagation of AGG.

5.2 Effects of Composition on Precipitate and Microstructural Evolution

4121Al is a standard SAE 4121 steel with Al and N additions and 4121Nb is a modified SAE 4121 steel with microadditions of Mo and Nb added to its composition. The average PAGS was similar between alloys, but was slightly finer on average in 4121Al after 328 min. 4121Al had only AlN precipitates present in its final microstructures while 4121Nb had lower amounts of AlN and Nb(C,N) present in its final microstructures. Nb(C,N) was finer than AlN on average, and additionally AlN had a range of precipitate sizes present in both 4121Al and 4121Nb. The thermomechanical history of the alloys used in this work created multiple instances where, according to equilibrium volume fraction predictions, the precipitates could have nucleated and

dissolved. AlN would have dissolved and nucleated at more points than Nb(C,N) due to its lower dissolution temperature. This lower dissolution temperature in addition to the higher coarsening rate of AlN led to this wider range of precipitate sizes.

Nb(C,N), being a finer precipitate, likely led to a higher degree of AGG in 4121Nb, as evidenced by the highest average amount of AGG occurring after the 328 min hold time in 4121Nb. This could have been due to the increased coarsening and dissolution rate of the finer precipitates, though there were no coarse Nb(C,N) observed.

CHAPTER 6: FUTURE WORK

Prudent avenues of future research would be further investigation of the precipitate evolution across the differently worked conditions in order to assess the degree to which warm and cold reduction affect precipitation and coarsening rates in both alloys. Measuring precipitation at different steps in the pre-treatment process could also contribute to understanding the exact impacts of warm reduction and cold reduction on strain induced precipitation and reversion of AlN and Nb(C,N) in carburizing steels. Electrochemical dissolution and precipitate extraction such as that done by Enloe *et al.* would be an effective method of characterizing precipitates [19].

Use of a carburizing atmosphere as well as subsequent fatigue testing of these carburized samples would also be valuable in order to create conditions more analogous to those used industrially and to test industrially relevant characteristics after a variety of pretreatment conditions. Vacuum carburization at higher temperatures in conjunction with warm and cold work pre-treatments would also provide valuable information on how effectively AlN and Nb(C,N) mitigate austenitic grain coarsening at higher temperatures after warm and cold reduction that matches conditions used in industrial parts. The effects of pre-treatment thermal history and microstructure development should also be investigated.

REFERENCES

[1] S. G. Davidson, J. P. Wise, and J. G. Speer, "The Influence of Titanium on Grain Size in High-Temperature Carburized Steels," in *Proceedings of the ASM 20th Heat Treating Conference*, St. Louis, Missouri, 2000, p. 1.

[2] Y. Kurebayashi and S. Nakamura, "Development of Ultra Fine Grain Steel for Carburizing," SAE International, Detroit, Michigan, Technical Paper 950209, pp. 5-7, 1995.

[3] J. P. Wise and D. K. Matlock, "Bending Fatigue of Carburized Steels: A Statistical Analysis of Process and Microstructural Parameters," *SAE Trans.*, vol. 109, pp. 182–191, 2000, doi: https://doi.org/10.4271/2000-01-0611.

[4] E. A. Holm, T. D. Hoffmann, A. D. Rollett, and C. G. Roberts, "Particle-Assisted Abnormal Grain Growth," in *IOP Conference Series Materials Science and Engineering*, in 012005, vol. 89. Aug. 2015. doi: 10.1088/1757-899X/89/1/012005.

[5] S. Lee, E. J. Seo, R. L. Cryderman, D. K. Matlock, and J. G. Speer, "Effects of Cold Work on Abnormal Grain Growth During Simulated Carburizing of 4121 Steel Containing Nb," *HT2021*. pp. 229–237, Sep. 2021. doi: 10.31399/asm.cp.ht2021p0229.

[6] Y. Kang, H. Yu, K. Wang, and Z. Wang, "Morphology and precipitation kinetics of AlN in hot strip of low carbon steel produced by compact strip production," *Mater. Sci. Eng. A*, vol. 351, no. 1–2, pp. 265–271, 2003, doi: https://doi.org/10.1016/S0921-5093(02)00845-6.

[7] K. Obayashi, *Carburizing of Steels*, vol. 2. in Encyclopedia of Materials: Metals and Alloys, vol. 2. Elsevier, pp. 162-172 2022.

[8] O. Underwood, J. Madison, R. M. Martens, G. B. Thompson, S. Welsh, and J. Evans, "An Examination of Abnormal Grain Growth in Low Strain Nickel-200," *Metallogr. Microstruct. Anal.*, vol. 5, no. 4, pp. 302–312, 2016, doi: 10.1007/s13632-016-0290-0.

[9] M. A. Razzak, M. Perez, T. Sourmail, S. Cazottes, and M. Frotey, "Preventing Abnormal Grain Growth of Austenite in Low Alloy Steels," *ISIJ Int.*, vol. 54, no. 8, pp. 1927–1934, Aug. 2014, doi: 10.2355/ISIJINTERNATIONAL.54.1927.

[10] V. F. Zackay, M. W. Justusson, and D. Schmatz, "Strengthening Mechanisms in Solids," ASM, Metals Park, Ohio, pp. 179, 1962.

[11] G. Krauss, "Steel Heat Treatment and Processing Principles," ASM International, Materials Park, Ohio, pp. 194. 1990.

[12] G. Krauss, *Steels - Processing, Structure, and Performance*. ASM International, pp. 31, 2005.

[13] L.-Å. Norström, "The relation between microstructure and yield strength in tempered low-carbon lath martensite with 5% nickel," *Met. Sci.*, vol. 10, no. 12, pp. 429–436, 1976, doi: https://doi.org/10.1179/030634576790431868.

[14] S. C. Kennett, "Strengthening and Toughening Mechanisms in Low-C Microalloyed Martensitic Steel as Influenced by Austenite Conditioning," Colorado School of Mines, PhD Thesis, pp. 21, 2014.

[15] Y. Ohmori and T. Kunitake, "Effects of austenite grain size and grain boundary segregation of impurity atoms on high temperature ductility," *Met. Sci.*, vol. 17, no. 7, pp. 328–332, 1983, doi: https://doi.org/10.1179/030634583790420781.

[16] N. T. Baker, *Future Developments of Metals and Ceramics*. London: Institute of Materials, pp. 75, 1992.

[17] T. Gladman and F. G. Wilson, "Aluminum Nitride in Steel," *Int. Mater. Rev.*, vol. 33, no. 5, pp. 221–286, 1988.

[18] E. J. Seo, J. G. Speer, D. K. Matlock, and R. L. Cryderman, "Effect of Mo in Combination with Nb on Austenite Grain Size Control in Vacuum Carburizing Steels," *J. Mater. Eng. Perform.*, vol. 29, no. 6, pp. 3575–3584, Jun. 2020, doi: 10.1007/s11665-020-04751-8.

[19] C. M. Enloe, "The Effect of Molybdenum on Niobium, Titanium Carbonitride Precipitate Evolution and Grain Refinement in High-Temperature Vacuum Carburizing Alloys," Colorado School of Mines, PhD thesis, 2013.

[20] K. A. AlOgab, D. K. Matlock, and J. G. Speer, "Austenite Grain-Size Control at Elevated Temperature in Microalloyed Carburizing Steels," 2004.

[21] T. Gladman, *The Physical Metallurgy of Microalloyed Steels*. London: The Institute of Materials, pp. 82-101, 1997.

[22] M. Apel, B. Boettger, J. Rudnizki, P. Schaffnit, and I. Steinbach, "Grain Growth Simulations Including Particle Pinning Using the Multiphase-field Concept," *ISIJ Int.*, vol. 49, no. 7, pp. 1024–1029, 2009, doi: 10.2355/isijinternational.49.1024.

[23] M. Gómez, L. Rancel, and S. F. Medina, "Effects of aluminium and nitrogen on static recrystallisation in V-microalloyed steels," *Mater. Sci. Eng. A*, vol. 506, no. 1, pp. 165–173, 2009, doi: https://doi.org/10.1016/j.msea.2008.11.049.

[24] D. San Martín, F. G. Caballero, C. Capdevila, and C. García de Andrés, "Discussion on the Rate Controlling Process of Coarsening of Niobium Carbonitrides in a Niobium Microalloyed Stee," *Mater. Sci. Forum*, vol. 500–501, pp. 703–710, 2005, doi: 10.4028/www.scientific.net/MSF.500-501.703.

[25] B. Dutta, E. Valdes, and C. M. Sellars, "Mechanism and kinetics of strain induced precipitation of Nb(C,N) in austenite," *Acta Metall. Mater.*, vol. 40, no. 4, pp. 653–662, 1992, doi: https://doi.org/10.1016/0956-7151(92)90006-Z.

[26] W.-B. Lee, S.-G. Hong, C.-G. Park, and S.-H. Park, "Carbide precipitation and high-temperature strength of hot-rolled high-strength, low-alloy steels containing Nb and Mo," *Metall. Mater. Trans. A*, vol. 33, no. 6, pp. 1689–1698, Jun. 2002, doi: 10.1007/s11661-002-0178-2.

[27] A. M. H. S. Kurokawa J. E. Ruzzante and F. Dyment, "Diffusion of Nb in Fe and Fe alloys," *Met. Sci.*, vol. 17, no. 9, pp. 433–438, 1983, doi: 10.1179/030634583790420628.

[28] R. Uemori, R. Chijiiwa, H. Tamehiro, and H. Morikawa, "AP-FIM study on the effect of Mo addition on microstructure in Ti-Nb steel," *Appl. Surf. Sci.*, vol. 76–77, pp. 255–260, 1994, doi: https://doi.org/10.1016/0169-4332(94)90351-4.

[29] B. Dutta, E. Palmiere, and C. Sellars, "Modelling the Kinetics of Strain Induced Precipitation in Nb Microalloyed Steels," *Acta Mater.*, vol. 49, no. 5, pp. 785–794, Mar. 2001, doi: 10.1016.

[30] J. D. Robson, "Modelling the overlap of nucleation, growth and coarsening during precipitation," *Acta Mater.*, vol. 52, no. 15, pp. 4669–4676, 2004, doi: https://doi.org/10.1016/j.actamat.2004.06.024.

[31] J. W. Cahn, "Nucleation on Dislocations," *Acta Metall.*, vol. 5, no. 3, pp. 169–172, 1957, doi: https://doi.org/10.1016/0001-6160(57)90021-4.

[32] R. Gómez-Ramírez and G. M. Pound, "Nucleation of a second solid phase along dislocations," *Metall. Trans.*, vol. 4, pp. 1563–1570, 1973, doi: https://doi.org/10.1007/BF02668009.

[33] J. L. Pacheco and G. Krauss, "Microstructure and High Bending Fatigue Strength in Carburized Steel," *J. Heat Treat.*, no. 7, pp. 77–86, 1989, doi: https://doi.org/10.1007/BF02833192.

[34] X. Zhang, K. Matsuura, and M. Ohno, “Effect of Cold-Deformation on Austenite Grain Growth Behavior in Solution-Treated Low Alloy Steel,” *Metals*, vol. 8, no. 12, pp. 1004, Dec. 2018, doi: 10.3390/met8121004.

[35] S. Lee, R. L. Cryderman, D. K. Matlock, and J. G. Speer, “Controlling Austenite Grain Growth in Annealed and Cold Formed Steel During Carburizing,” Colorado School of Mines, ASPPRC Research Report No. MT-SRC-021-007, 2021.

[36] R. Barbosa, “The Influence of Chemical Composition on the Recrystallisation Behaviour of Microalloyed Steels,” *Process. Microstruct. Prop. HSLA Steels*, pp. 51–61, 1987.

[37] M. Gómez and S. F. Medina, “Role of microalloying elements in the microstructure of hot rolled steels,” *Int. J. Mater. Res.*, vol. 102, no. 10, pp. 1197–1207, 2011, doi: 10.3139/146.110585.

[38] M. D. Geib, D. K. Matlock, and G. Krauss, “The effect of intercritical annealing temperature on the structure of niobium microalloyed dualphase steel,” *Metall. Trans. A*, vol. 11, no. 10, pp. 1683–1689, Oct. 1980, doi: 10.1007/BF02660523.

[39] G. M. Michal and I. E. Locci, “Analysis of microalloy precipitate reversion in steels,” *Scr. Metall.*, vol. 22, no. 11, pp. 1801–1806, 1988, doi: https://doi.org/10.1016/S0036-9748(88)80288-6.

APPENDIX A: MICROGRAPHS OF EACH WARM REDUCTION AND COLD REDUCTION COMBINATION

This appendix provides micrographs representative of each WR+CR combination in both alloys for each hold time. Figures are sorted by the pct CR done to the samples prior to simulated carburization in order from 5 pct CR to 25 pct CR.

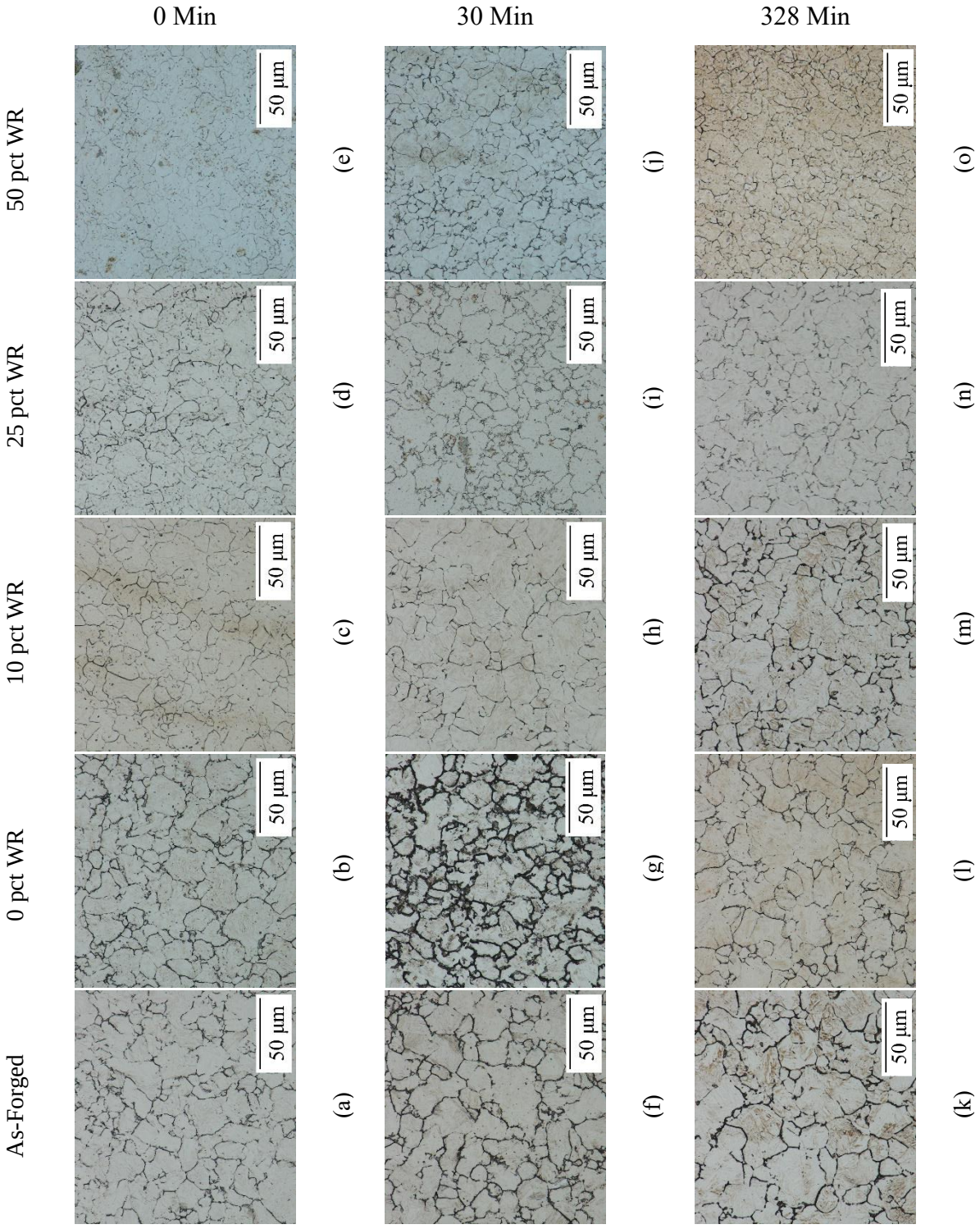


Figure A-1 Micrographs of each WR condition and the as-forged condition of 4121Al after 5 pct CR and picral etching at 1664x magnification. (a)-(e) depict the 0 min dwell time condition, (f)-(j) depict the 30 min dwell time condition, and (k)-(o) depict the 328 min dwell time condition. Olympus® DSX500 light optical micrographs.

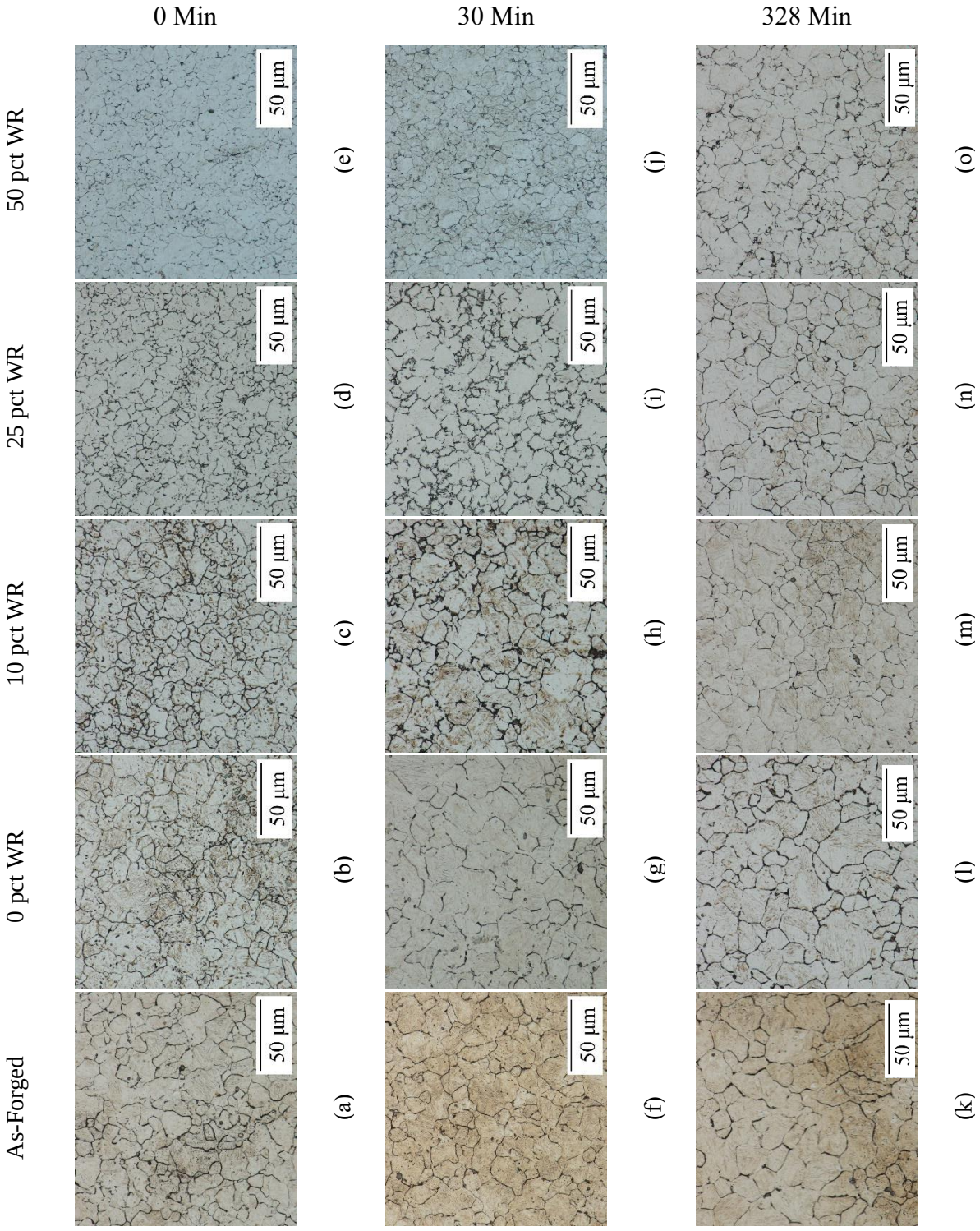


Figure A-2 Micrographs of each WR condition and the as-forged condition of 4121Nb after 5 pct CR and picral etching at 1664x magnification. (a)-(e) depict the 0 min dwell time condition, (f)-(j) depict the 30 min dwell time condition, and (k)-(o) depict the 328 min dwell time condition. Olympus® DSX500 light optical micrographs.

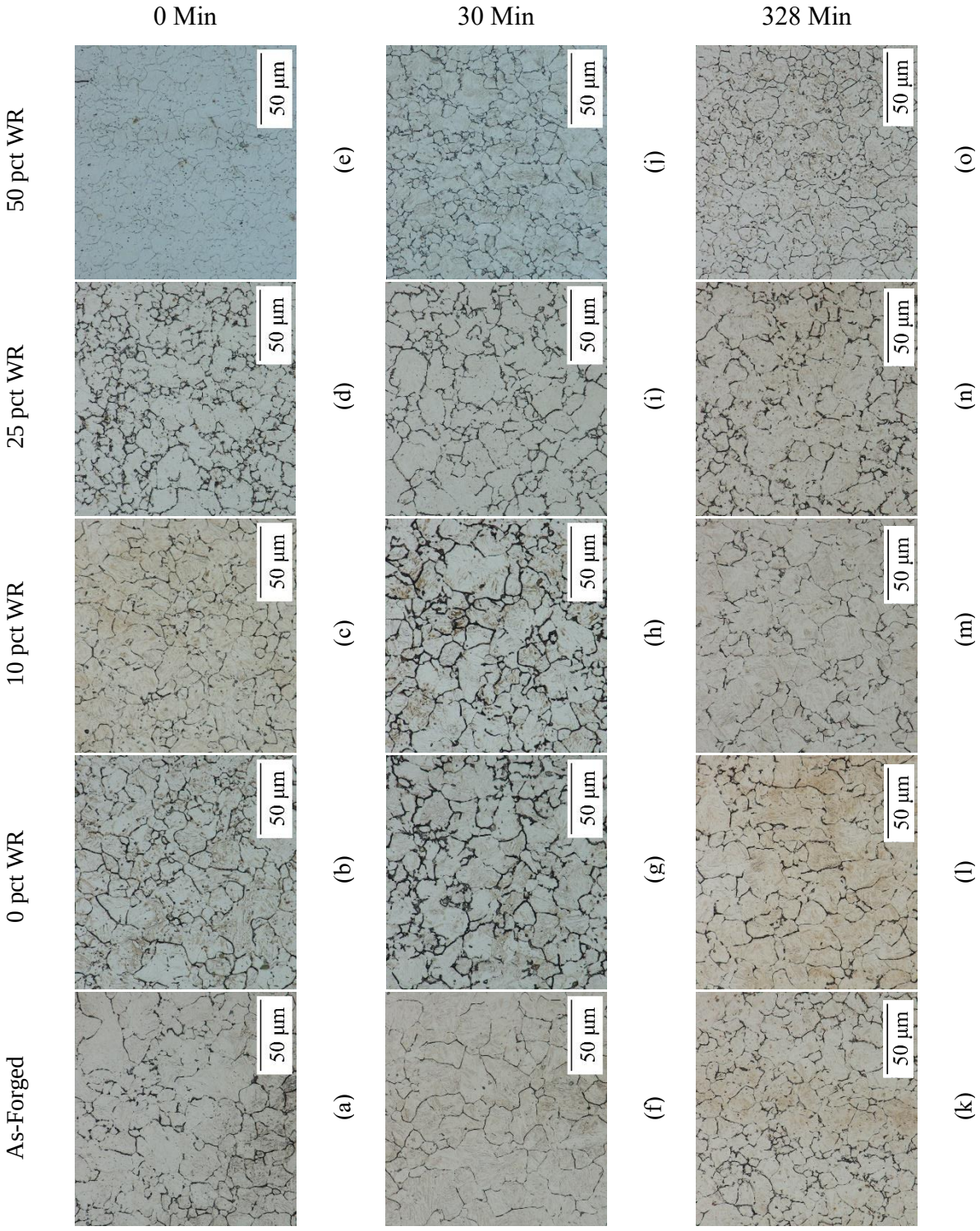


Figure A-3 Micrographs of each WR condition and the as-forged condition of 4121Al after 10 pct CR and picral etching at 1664x magnification. (a)-(e) depict the 0 min dwell time condition, (f)-(j) depict the 30 min dwell time condition, and (k)-(o) depict the 328 min dwell time condition. Olympus® DSX500 light optical micrographs.

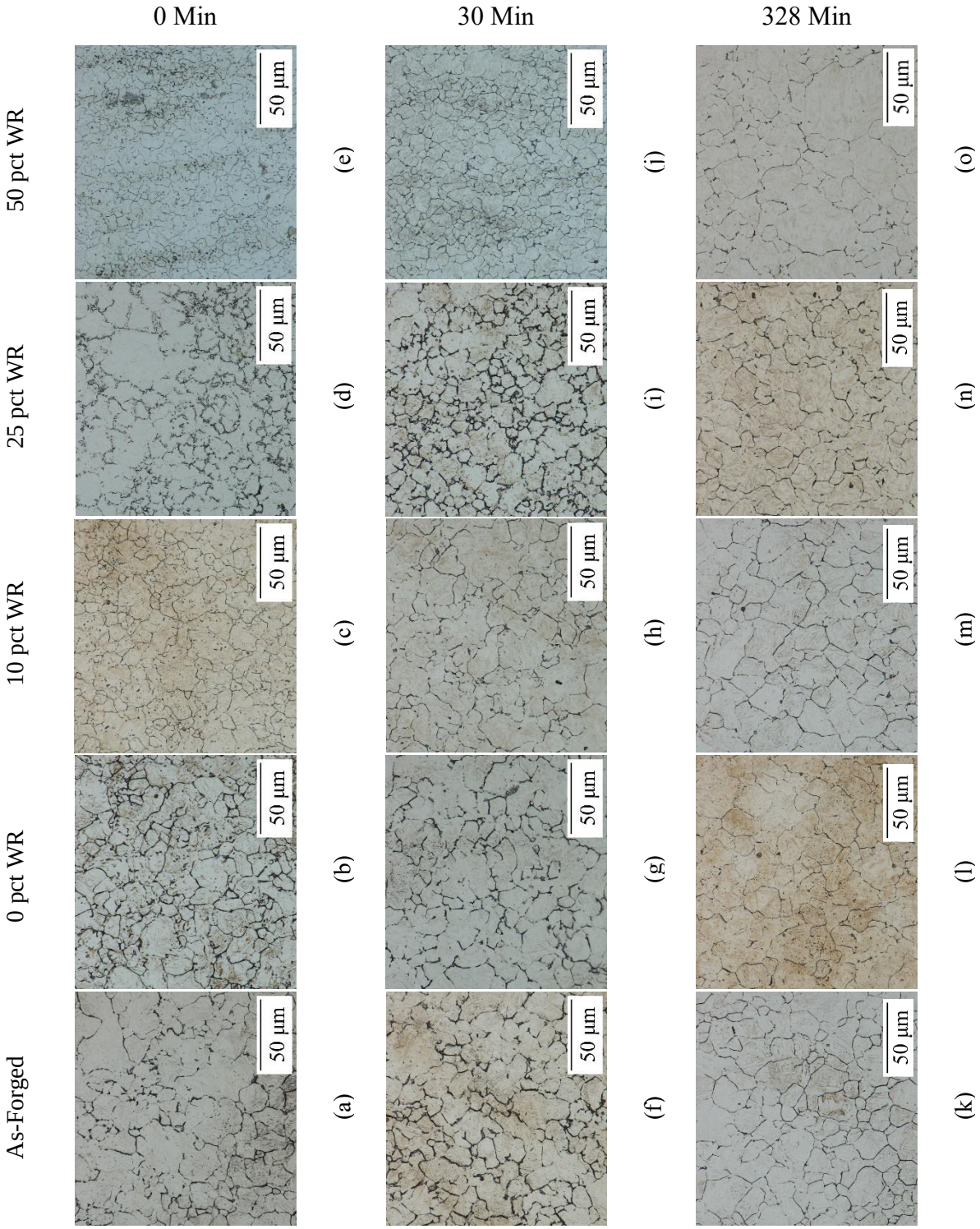


Figure A-4 Micrographs of each WR condition and the as-forged condition of 4121Nb after 10 pct CR and picral etching at 1664x magnification. (a)-(e) depict the 0 min dwell time condition, (f)-(j) depict the 30 min dwell time condition, and (k)-(o) depict the 328 min dwell time condition. Olympus® DSX500 light optical micrographs.

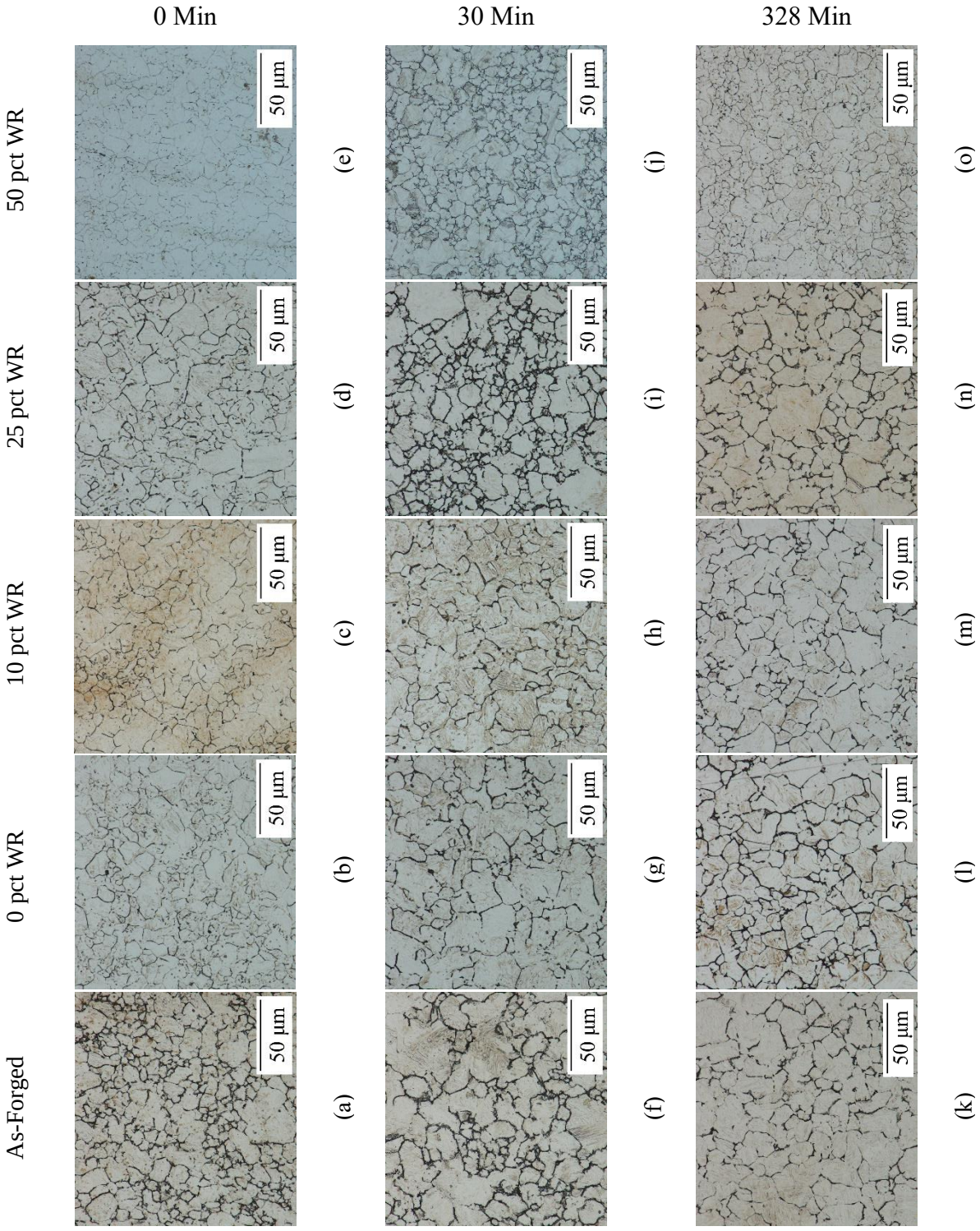


Figure A-5 Micrographs of each WR condition and the as-forged condition of 4121Al after 25 pct CR and picral etching at 1664x magnification. (a)-(e) depict the 0 min dwell time condition, (f)-(j) depict the 30 min dwell time condition, and (k)-(o) depict the 328 min dwell time condition. Olympus® DSX500 light optical micrographs.

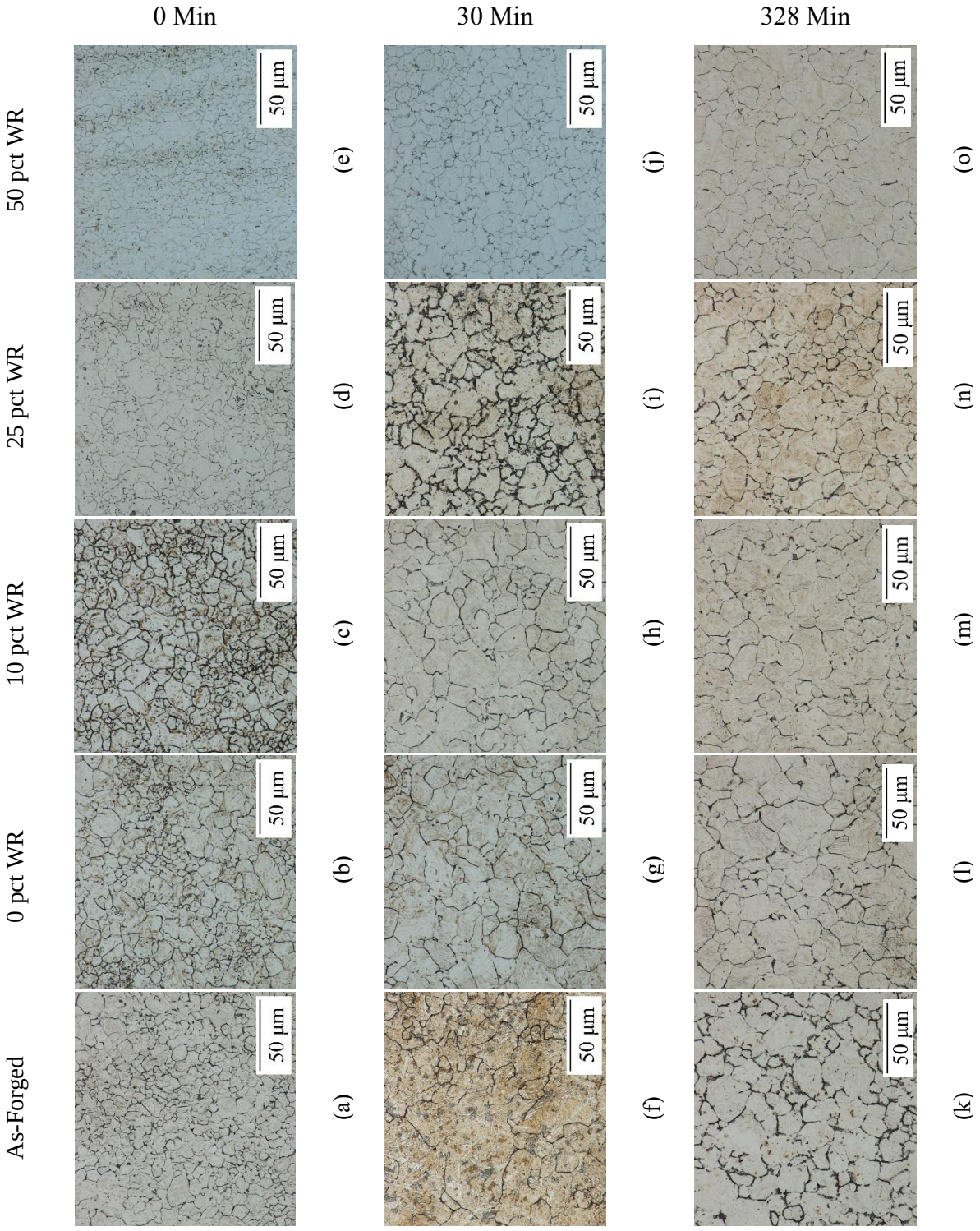


Figure A-6 Micrographs of each WR condition and the as-forged condition of 4121Nb after 25 pct CR and picral etching at 1664x magnification. (a)-(e) depict the 0 min dwell time condition, (f)-(j) depict the 30 min dwell time condition, and (k)-(o) depict the 328 min dwell time condition. Olympus® DSX500 light optical micrographs.

APPENDIX B: 2D PLOTS OF AIL AND AGG

This appendix provides 2D plots depicting the AIL and degree of AGG with respect to both warm and cold reduction. Figure B-1 and Figure B-2 plot AIL of 4121Al and 4121Nb with respect to WR and CR, respectively. Figure B-3 and Figure B-4 plot percentage total grain area taken up by abnormal grains for both 4121Al and 4121Nb with respect to WR and CR, respectively.

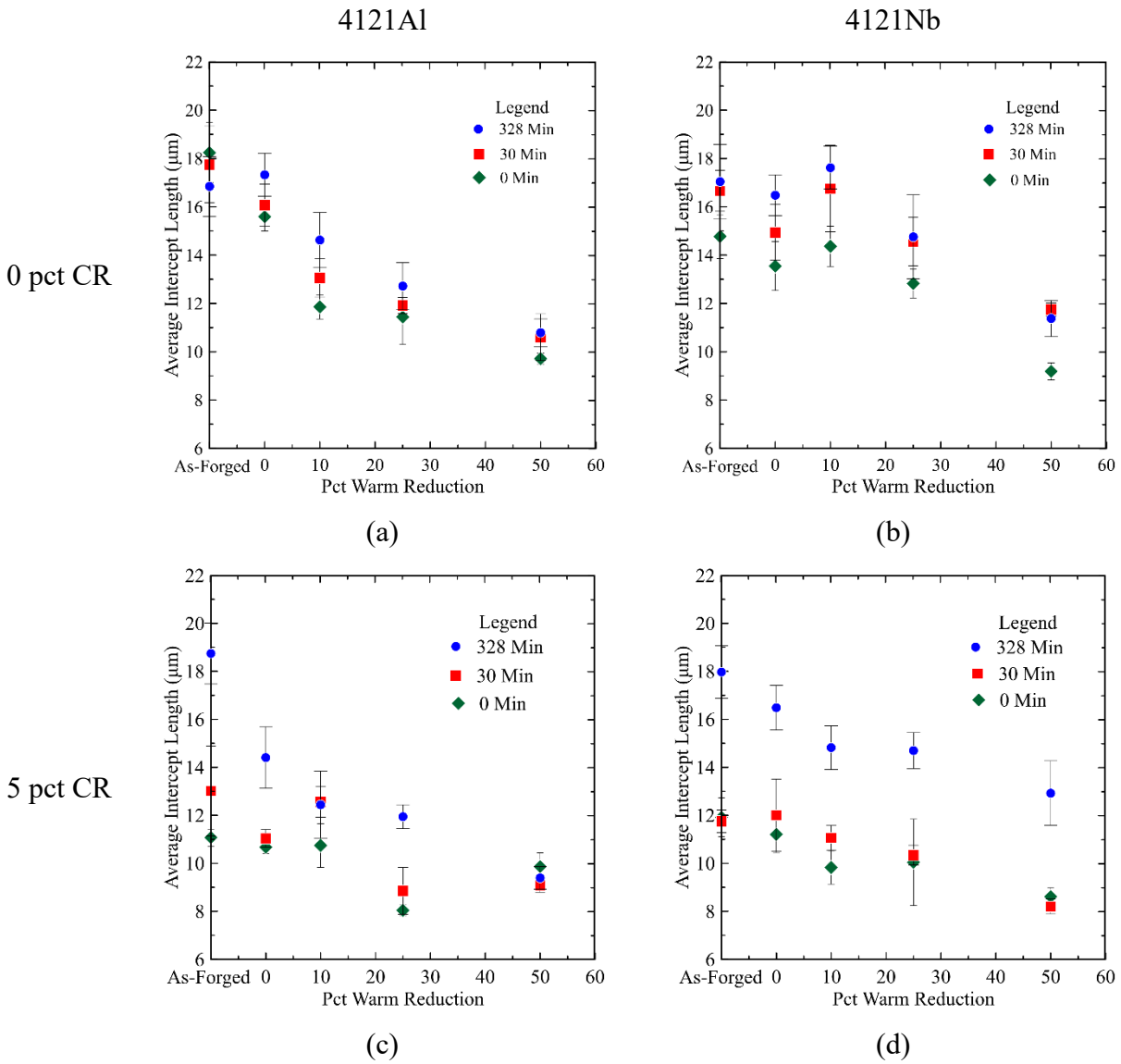
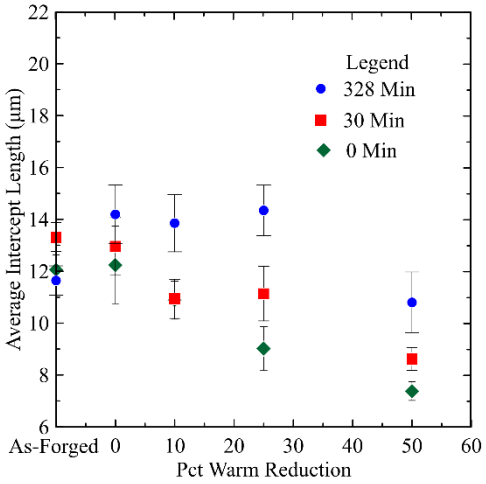


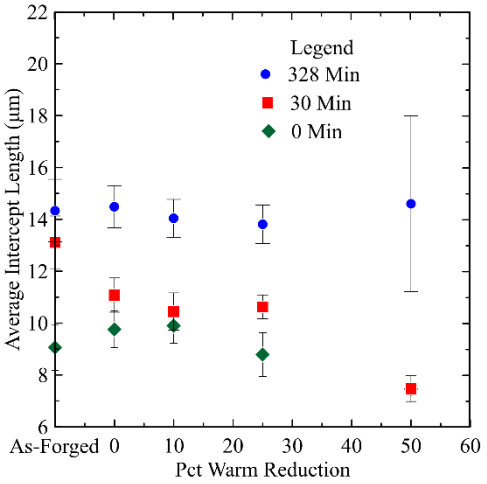
Figure B-1 Average intercept length of each CR condition with respect to WR for both alloys where 4121Al has been subjected to (a) 0 pct CR, (c) 5 pct CR, (e) 10 pct CR, and (g) 25 pct CR and 4121Nb after (b) 0 pct CR, (d) 5 pct CR, (f) 10 pct CR, and (h) 25 pct CR.

Figure B-1 Continued

10 pct CR

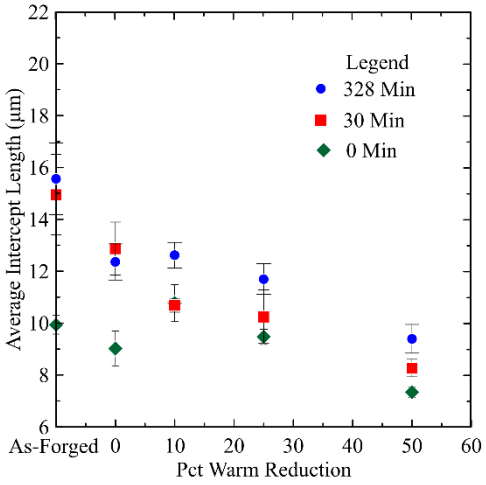


(e)

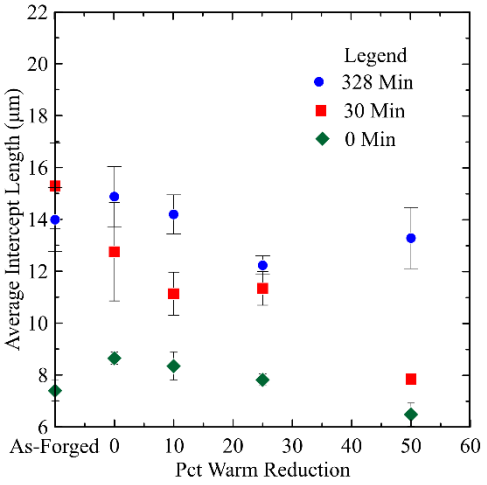


(f)

25 pct CR



(g)



(h)

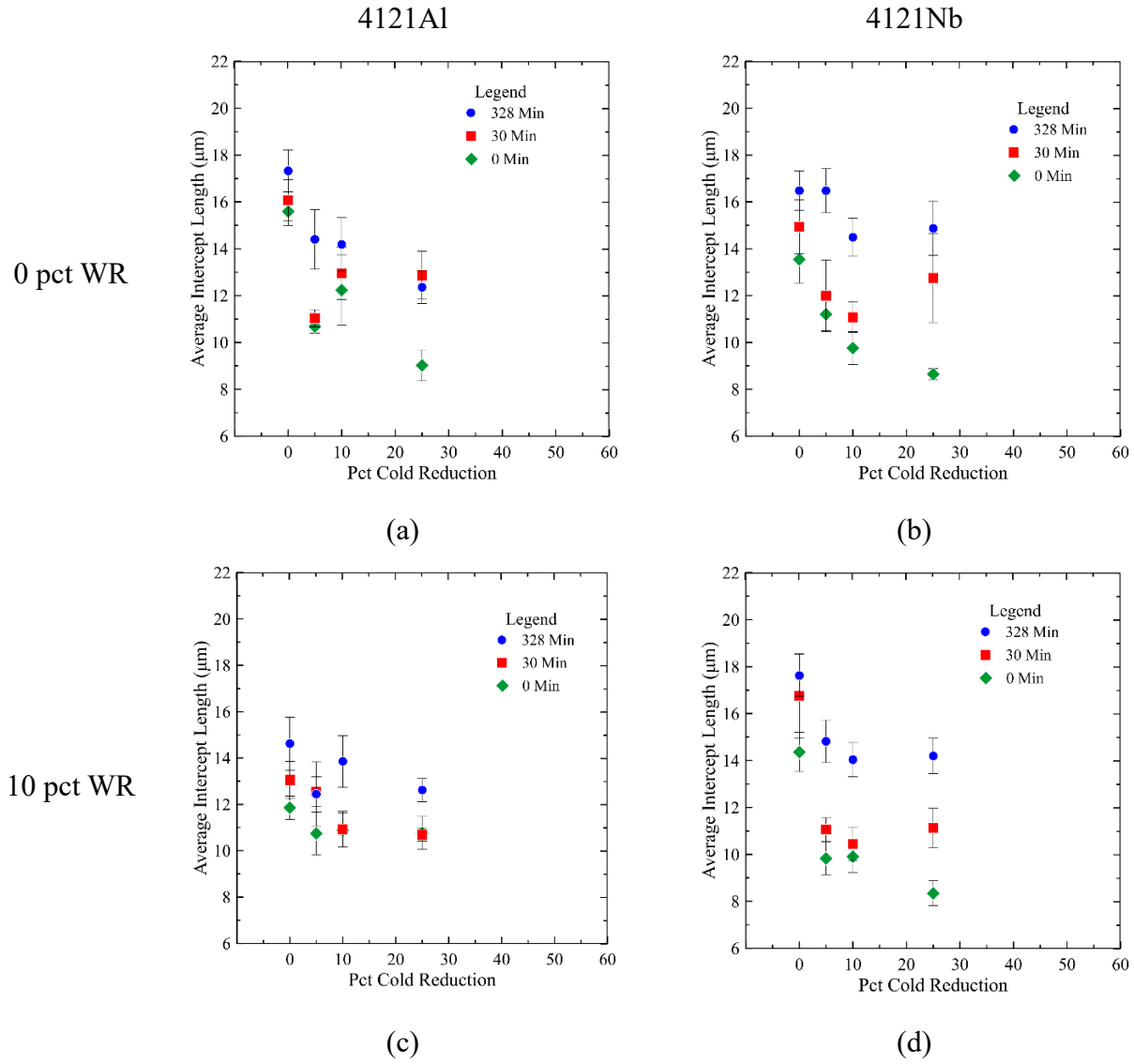
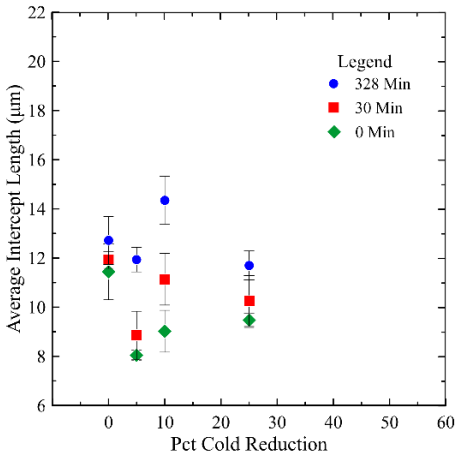


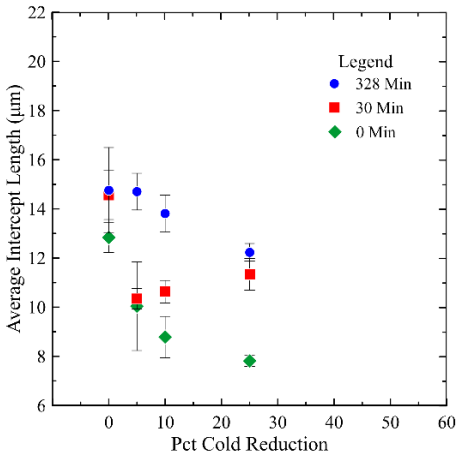
Figure B-2 Average intercept length of each WR condition with respect to CR for both alloys where 4121Al has been subjected to (a) 0 pct WR, (c) 10 pct WR, (e) 25 pct WR, (g) 50 pct WR, and (i) the as-forged condition and 4121Nb after (b) 0 pct WR, (d) 10 pct WR, (f) 25 pct WR, (h) 50 pct WR, and (j) the as-forged condition.

Figure B-2 Continued

25 pct WR

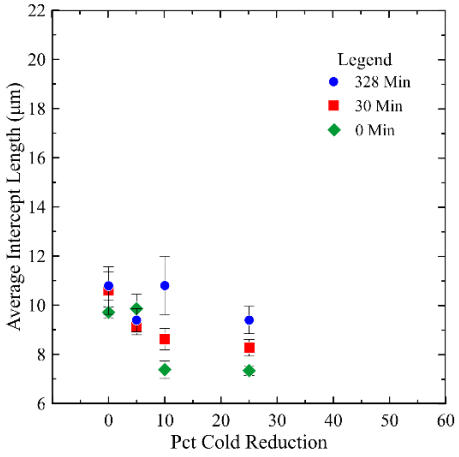


(e)

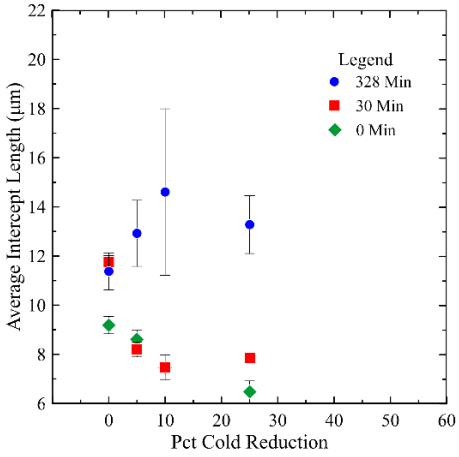


(f)

50 pct WR

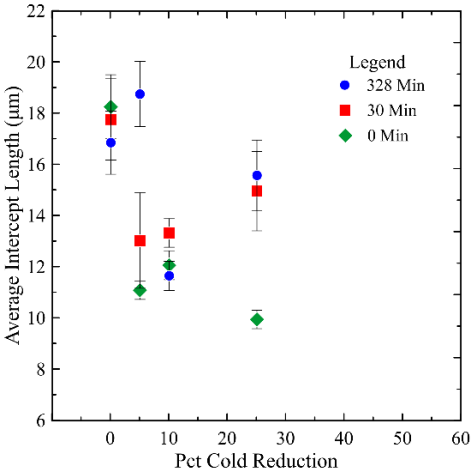


(g)

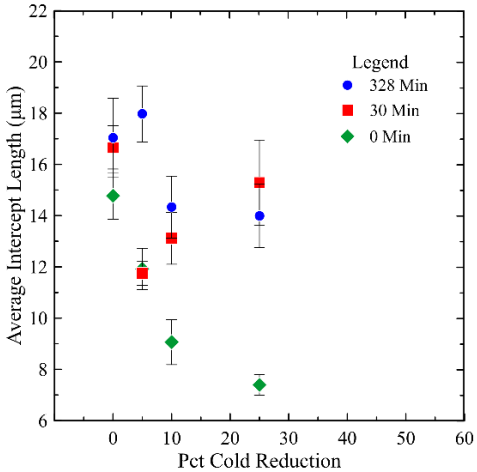


(h)

AF



(i)



(j)

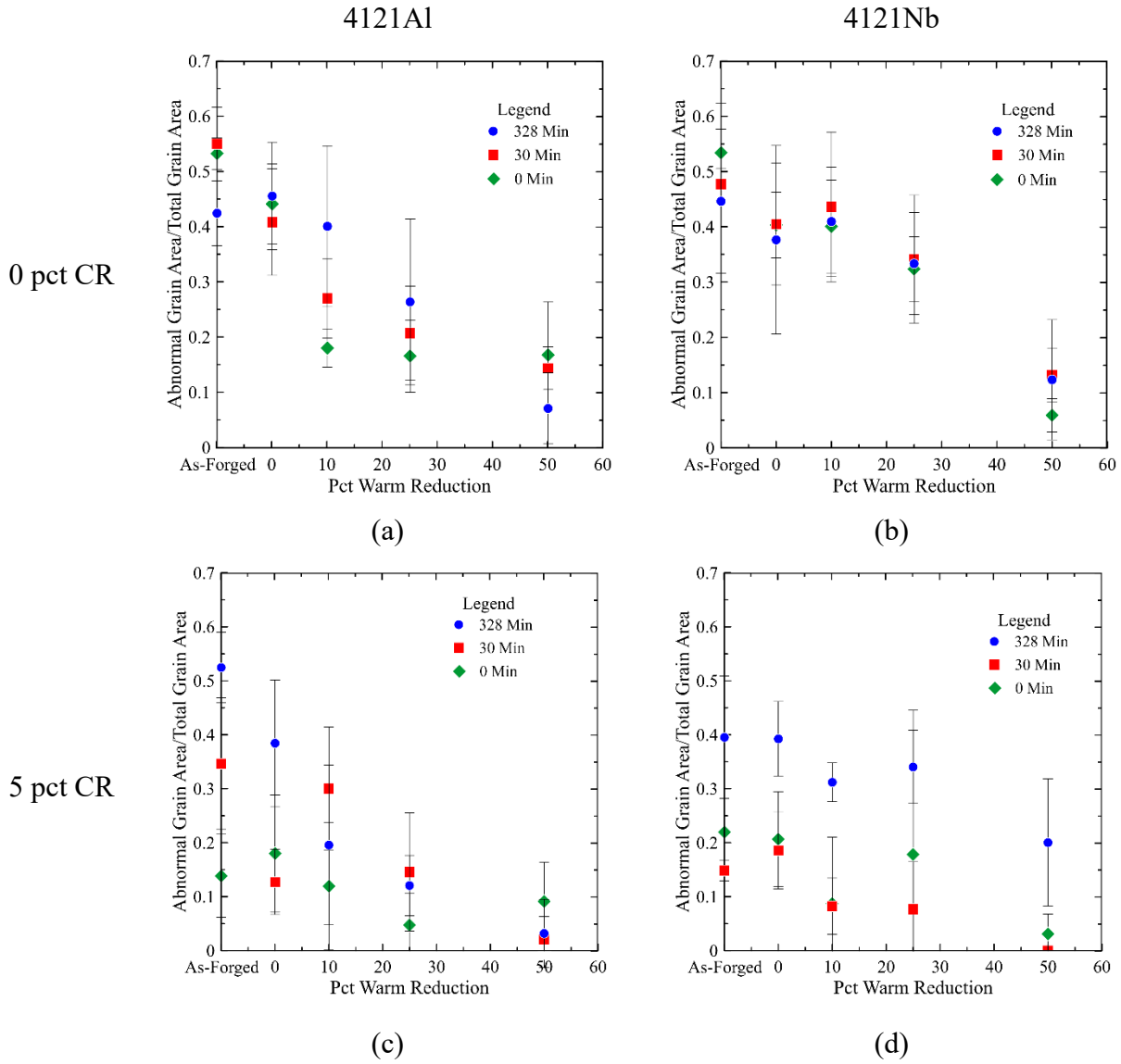
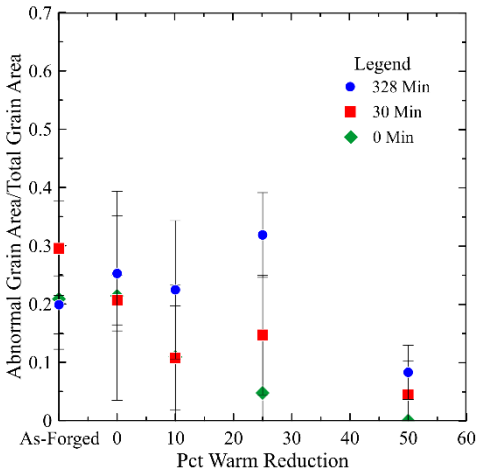


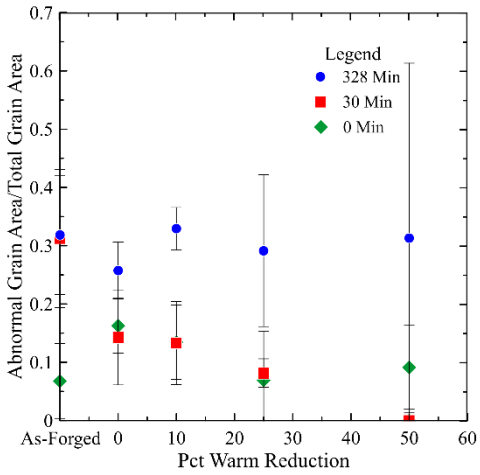
Figure B-3 Percentage area of abnormal grains normalized over the total microstructural area of each CR condition with respect to WR for both alloys where 4121Al has been subjected to (a) 0 pct CR, (c) 5 pct CR, (e) 10 pct CR, and (g) 25 pct CR and 4121Nb after (b) 0 pct CR, (d) 5 pct CR, (f) 10 pct CR, and (h) 25 pct CR.

Figure B-3 Continued

10 pct CR

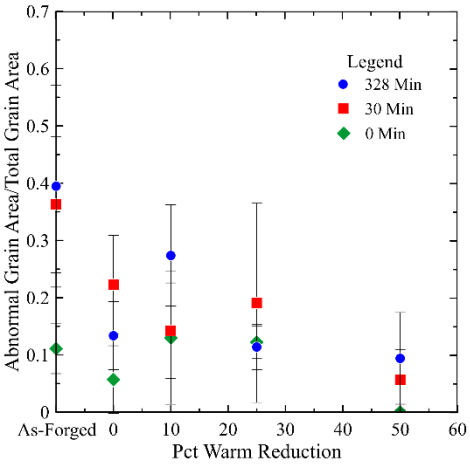


(e)

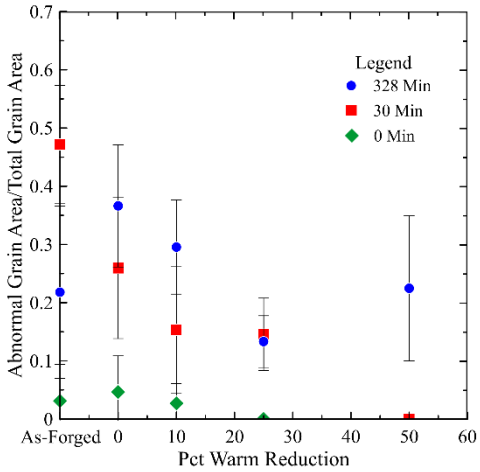


(f)

25 pct CR



(g)



(h)

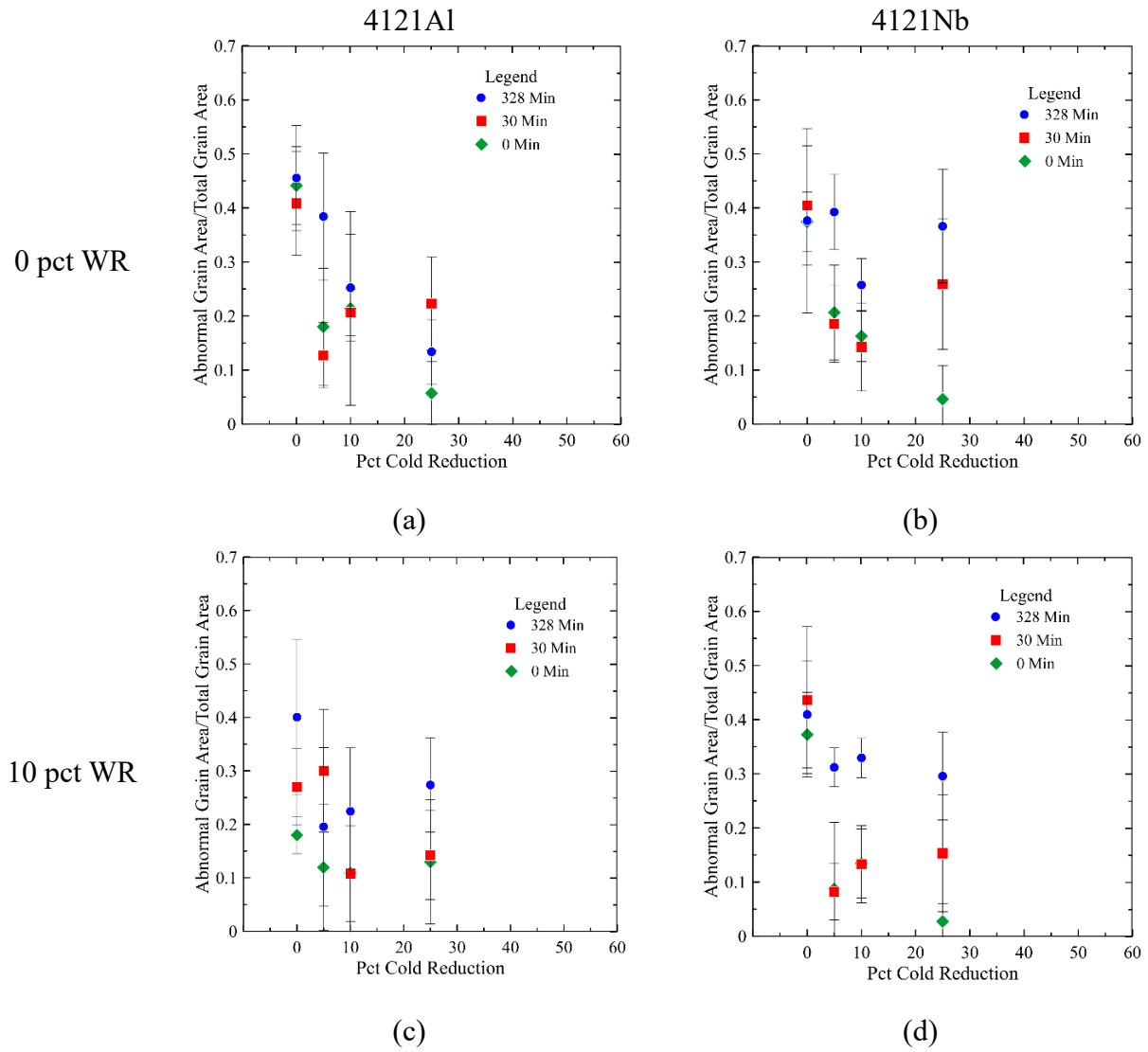
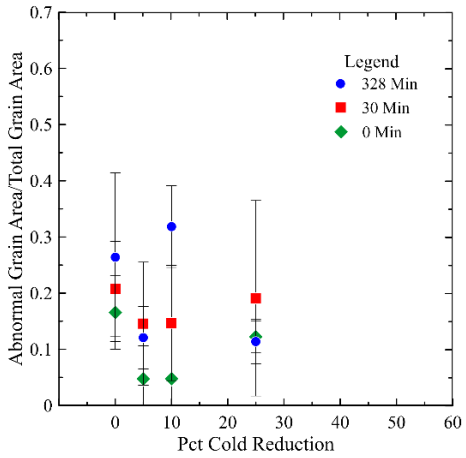


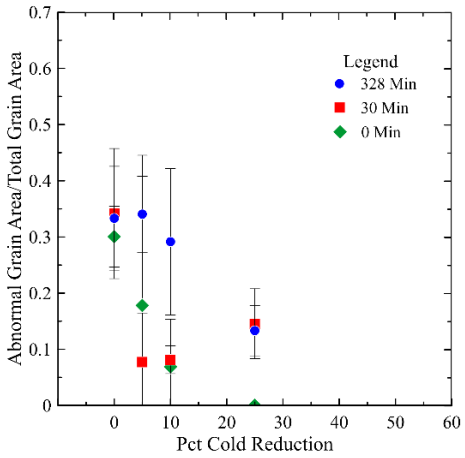
Figure B-4 Percentage area of abnormal grains normalized over the total microstructural area of each WR condition with respect to CR for both alloys where 4121Al has been subjected to (a) 0 pct WR, (c) 10 pct WR, (e) 25 pct WR, (g) 50 pct WR, and (i) the as-forged condition and 4121Nb after (b) 0 pct WR, (d) 10 pct WR, (f) 25 pct WR, (h) 50 pct WR, and (j) the as-forged condition.

Figure B-4 Continued

25 pct WR

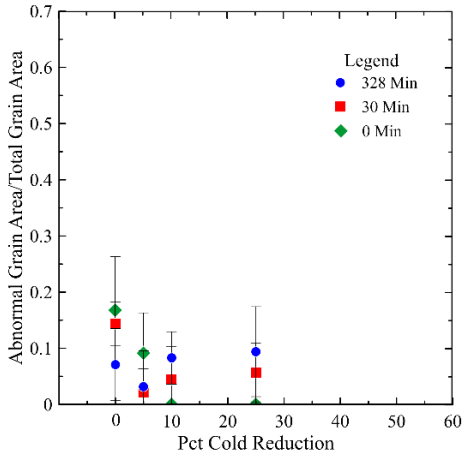


(e)

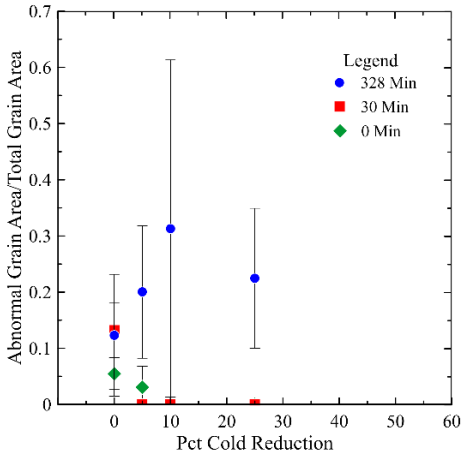


(f)

50 pct WR

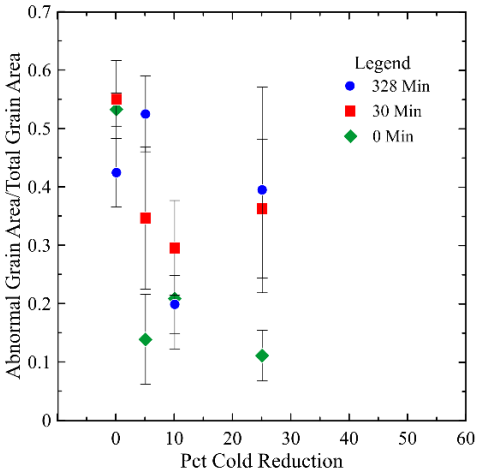


(g)

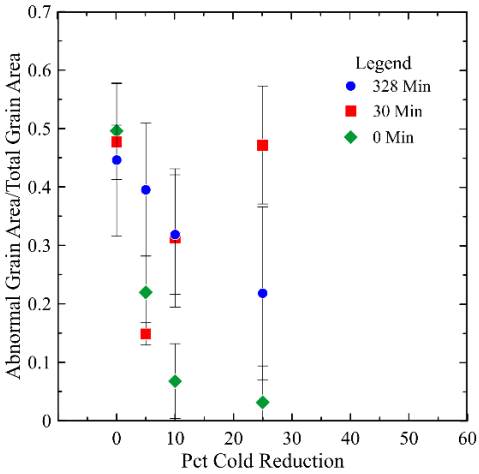


(h)

AF



(i)



(j)

APPENDIX C: AIL WITH RESPECT TO WARM AND COLD REDUCTION

This appendix contains tables with all intercept length data obtained from line-intercept measurements in MATLAB.

Table C-1 AIL of 4121Al by Warm Reduction

Dwell Time	Warm Reduction (pct)	AIL (μm)	Standard Deviation (μm)
0 Min	As-Forged	18.24	1.25
	0	15.59	0.60
	10	11.86	0.50
	25	11.44	1.14
	50	9.71	0.22
30 Min	As-Forged	17.75	1.58
	0	16.07	0.87
	10	13.06	0.79
	25	11.91	0.34
	50	10.60	0.97
328 Min	As-Forged	16.84	1.23
	0	17.32	0.89
	10	14.61	1.14
	25	12.71	0.98
	50	10.78	0.57

Table C-2 AIL of 4121Al by Warm Reduction

Dwell Time	Warm Reduction (pct)	AIL (μm)	Standard Deviation (μm)
0 Min	As-Forged	14.77	0.91
	0	13.55	1.01
	10	14.36	0.83
	25	12.83	0.60
	50	9.19	0.35
30 Min	As-Forged	16.66	0.84
	0	14.95	1.15
	10	16.76	1.79
	25	14.56	1.00
	50	11.75	0.27
328 Min	As-Forged	17.03	1.55
	0	16.47	0.84
	10	17.62	0.89
	25	14.75	1.74
	50	11.37	0.74

Table C-3 AIL of 4121Al After 5 pct Cold Reduction by WR

Dwell Time	Warm Reduction (pct)	AIL (μm)	Standard Deviation (μm)
0 Min	As-Forged	11.07	0.36
	0	10.67	0.28
	10	10.75	0.91
	25	8.04	0.22
	50	9.86	0.58
30 Min	As-Forged	13.02	1.86
	0	11.04	0.37
	10	12.55	0.64
	25	8.86	0.98
	50	9.10	0.30
328 Min	As-Forged	18.74	1.27
	0	14.40	1.28
	10	12.44	1.39
	25	11.94	0.50
	50	9.39	0.47

Table C-4 AIL of 4121Nb After 5 pct Cold Reduction by WR

Dwell Time	Warm Reduction (pct)	AIL (μm)	Standard Deviation (μm)
0 Min	As-Forged	11.92	0.81
	0	11.21	0.76
	10	9.83	0.69
	25	10.04	1.80
	50	8.61	0.37
30 Min	As-Forged	11.75	0.47
	0	12.00	1.51
	10	11.06	0.51
	25	10.34	0.41
	50	8.20	0.31
328 Min	As-Forged	17.97	1.09
	0	16.48	0.93
	10	14.82	0.91
	25	14.70	0.75
	50	12.92	1.34

Table C-5 AIL of 4121Al After 10 pct Cold Reduction by WR

Dwell Time	Warm Reduction (pct)	AIL (μm)	Standard Deviation (μm)
0 Min	As-Forged	12.06	0.57
	0	12.23	1.51
	10	10.89	0.73
	25	9.02	0.85
	50	7.37	0.36
30 Min	As-Forged	13.32	0.56
	0	12.95	1.11
	10	10.94	0.75
	25	11.14	1.05
	50	8.62	0.44
328 Min	As-Forged	11.64	0.57
	0	14.19	1.13
	10	13.85	1.11
	25	14.34	0.98
	50	10.80	1.17

Table C-6 AIL of 4121Nb After 10 pct Cold Reduction by WR

Dwell Time	Warm Reduction (pct)	AIL (μm)	Standard Deviation (μm)
0 Min	As-Forged	9.06	0.88
	0	9.76	0.71
	10	9.90	0.69
	25	8.78	0.84
	50	7.45	0.21
30 Min	As-Forged	13.12	1.01
	0	11.08	0.66
	10	10.45	0.72
	25	10.63	0.46
	50	7.47	0.50
328 Min	As-Forged	14.33	1.21
	0	14.49	0.81
	10	14.04	0.73
	25	13.81	0.75
	50	14.60	3.39

Table C-7 AIL of 4121Al After 25 pct Cold Reduction by WR

Dwell Time	Warm Reduction (pct)	AIL (μm)	Standard Deviation (μm)
0 Min	As-Forged	9.93	0.36
	0	9.02	0.67
	10	10.77	0.71
	25	9.47	0.29
	50	7.33	0.20
30 Min	As-Forged	14.95	1.55
	0	12.87	1.02
	10	10.69	0.27
	25	10.25	1.04
	50	8.27	0.34
328 Min	As-Forged	15.56	1.39
	0	12.36	0.69
	10	12.62	0.49
	25	11.70	0.59
	50	9.39	0.56

Table C-8 AIL of 4121Nb After 25 pct Cold Reduction by WR

Dwell Time	Warm Reduction (pct)	AIL (μm)	Standard Deviation (μm)
0 Min	As-Forged	7.39	0.40
	0	8.65	0.23
	10	8.35	0.53
	25	7.81	0.22
	50	6.47	0.44
30 Min	As-Forged	15.29	1.66
	0	12.76	1.90
	10	11.13	0.83
	25	11.34	0.65
	50	7.84	0.17
328 Min	As-Forged	13.99	1.24
	0	14.88	1.16
	10	14.19	0.75
	25	12.23	0.36
	50	13.28	1.18

APPENDIX D: GRAIN SIZE FREQUENCY

This appendix contains plots that show the grain size frequency measured across each experimental condition.

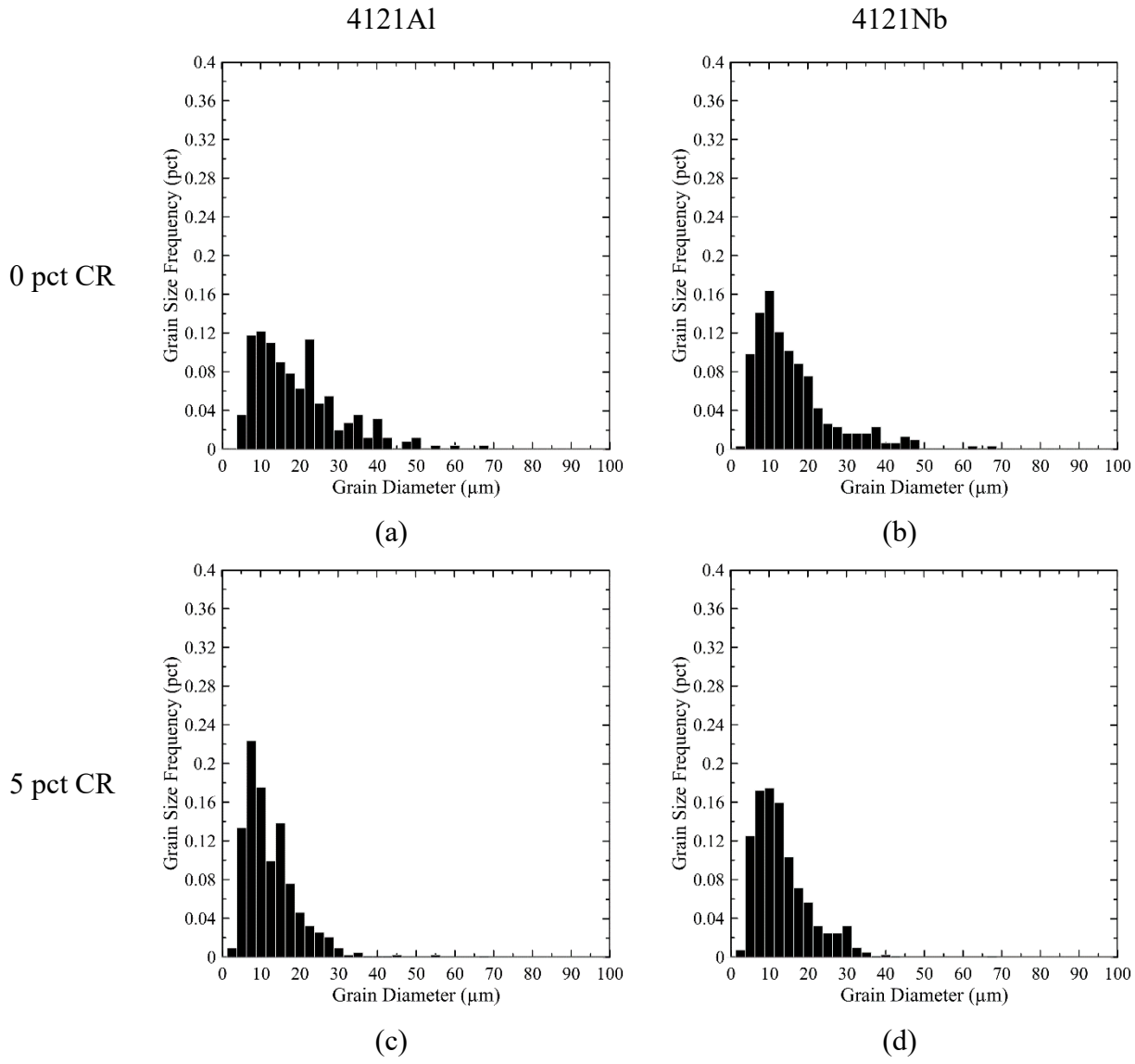
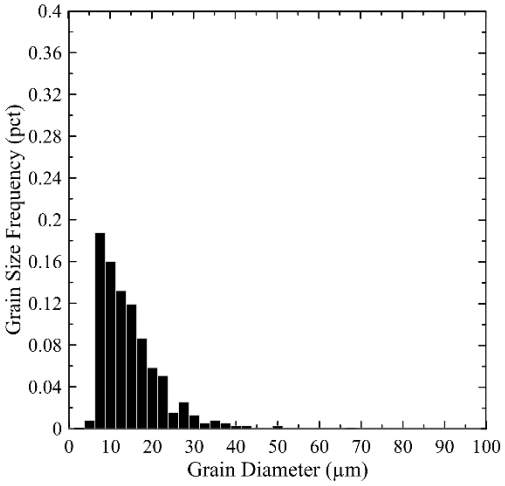


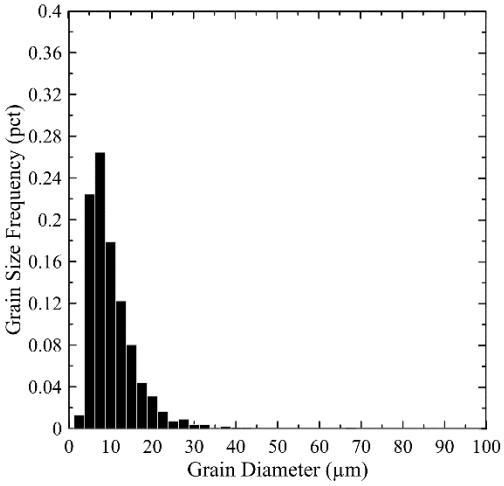
Figure D-1 Grain size frequency determined by line-intercept measurement in MATLAB of the as-forged condition for both alloys after 0 min of simulated carburization where 4121Al has been previously subjected to (a) 0 pct CR, (c) 5 pct CR, (e) 10 pct CR, and (g) 25 pct CR and 4121Nb after (b) 0 pct CR, (d) 5 pct CR, (f) 10 pct CR, and (h) 25 pct CR.

Figure D-1 Continued

10 pct CR

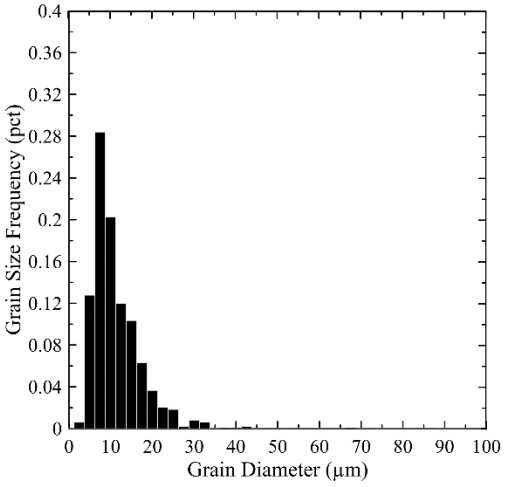


(e)

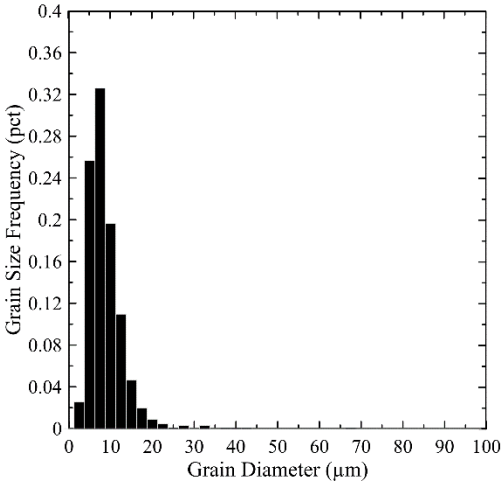


(f)

25 pct CR



(g)



(h)

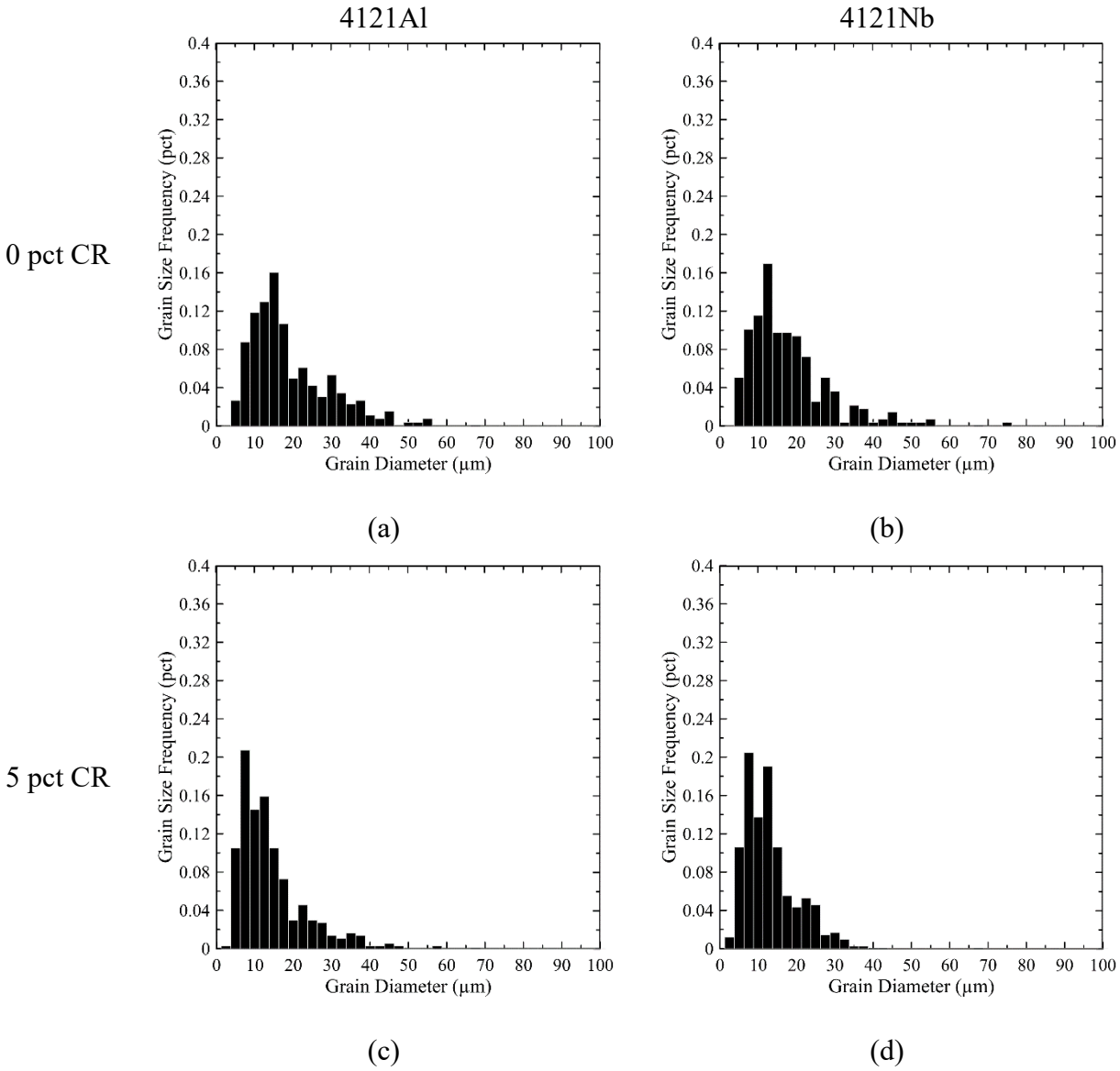
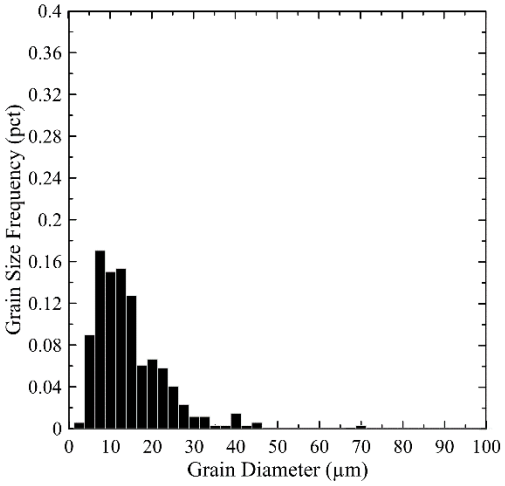


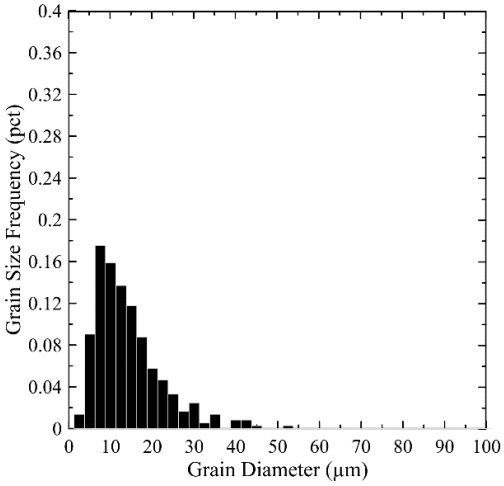
Figure D-2 Grain size frequency determined by line-intercept measurement in MATLAB of the as-forged condition for both alloys after 30 min of simulated carburization where 4121Al has been previously subjected to (a) 0 pct CR, (c) 5 pct CR, (e) 10 pct CR, and (g) 25 pct CR and 4121Nb after (b) 0 pct CR, (d) 5 pct CR, (f) 10 pct CR, and (h) 25 pct CR.

Figure D-2 Continued

10 pct CR

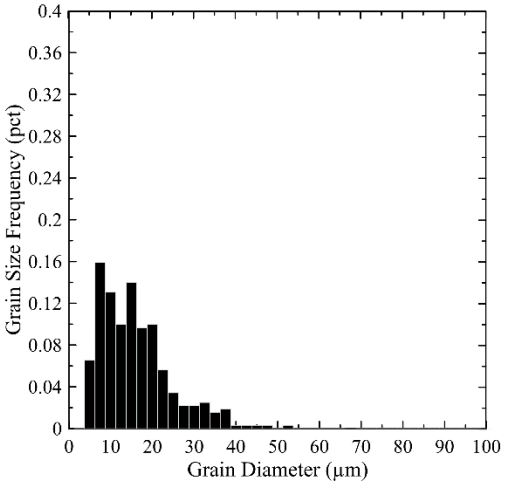


(e)

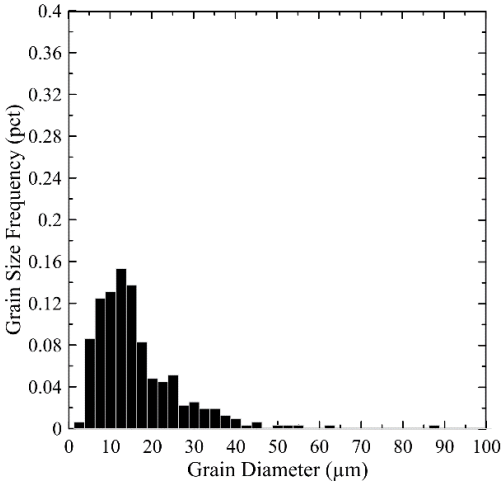


(f)

25 pct CR



(g)



(h)

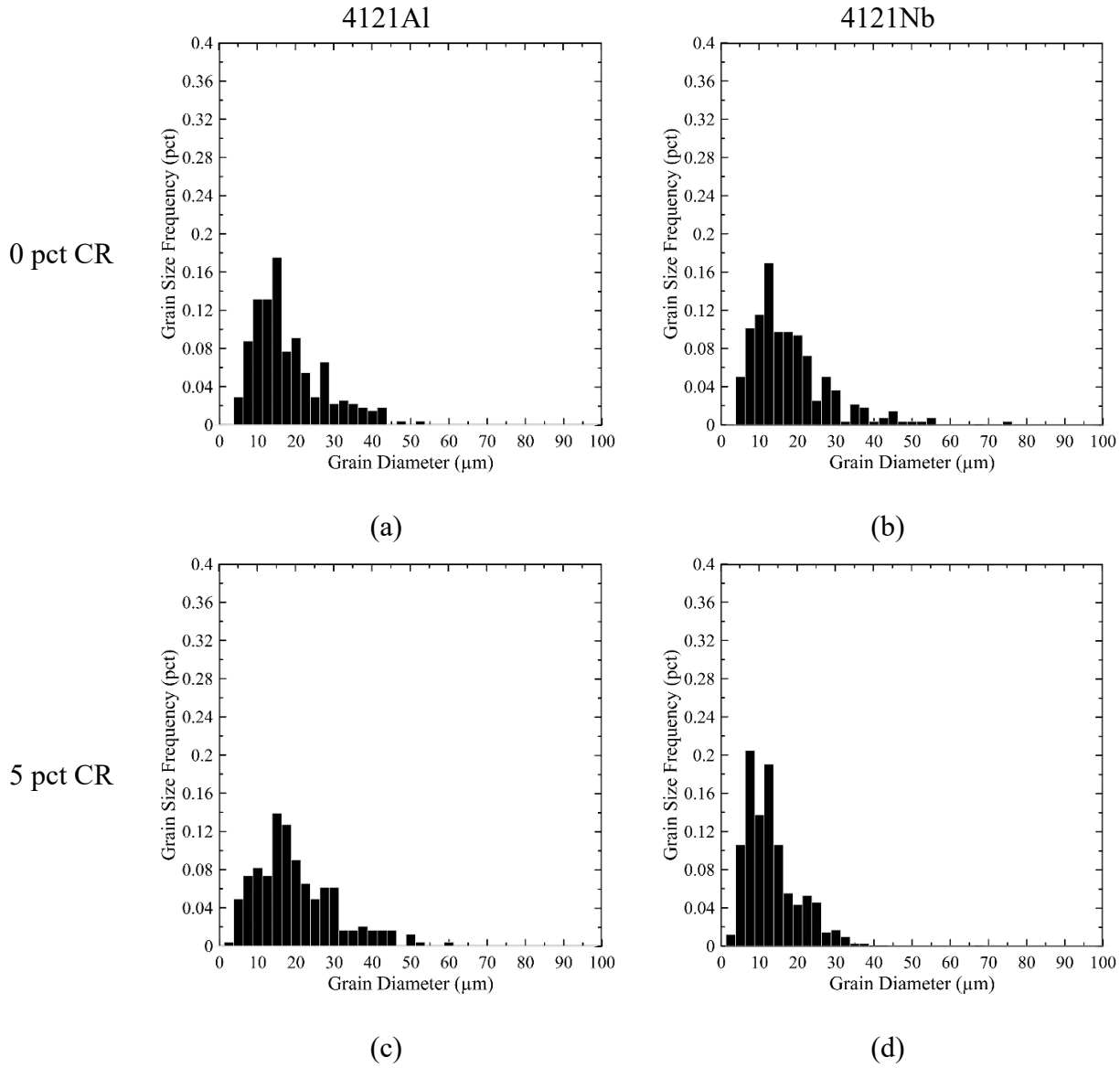
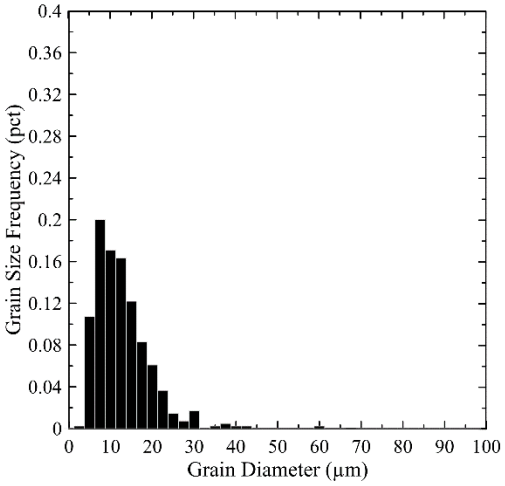


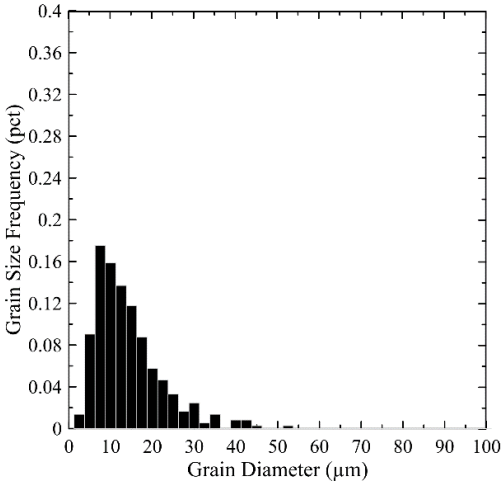
Figure D-3 Grain size frequency determined by line-intercept measurement in MATLAB of the as-forged condition for both alloys after 328 min of simulated carburization where 4121Al has been previously subjected to (a) 0 pct CR, (c) 5 pct CR, (e) 10 pct CR, and (g) 25 pct CR and 4121Nb after (b) 0 pct CR, (d) 5 pct CR, (f) 10 pct CR, and (h) 25 pct CR.

Figure D-3 Continued

10 pct CR

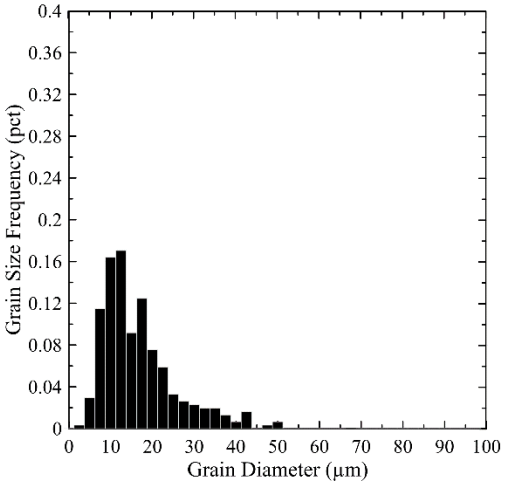


(e)

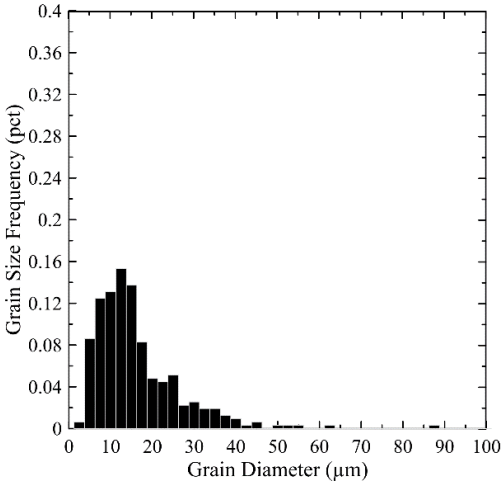


(f)

25 pct CR



(g)



(h)

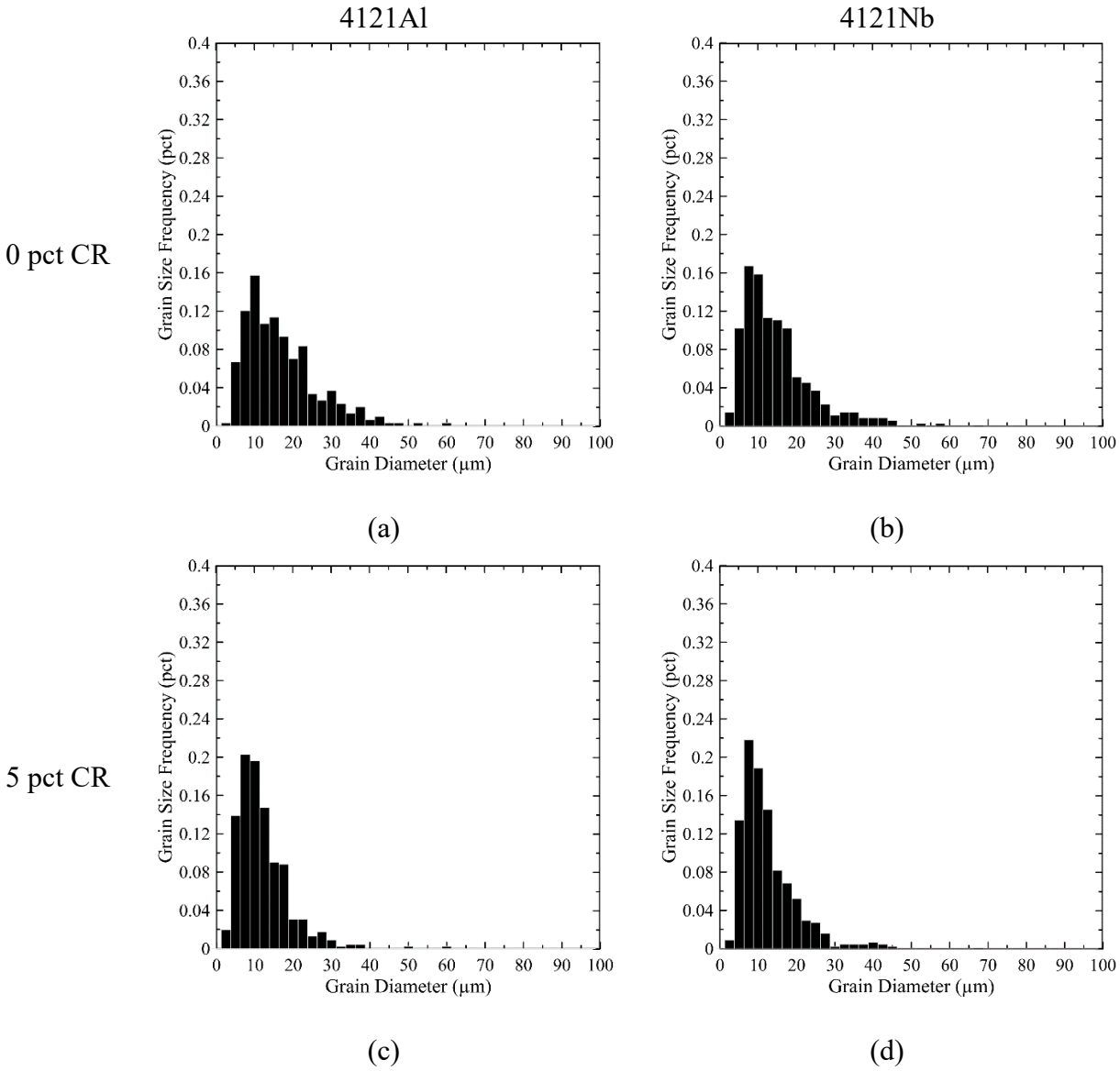
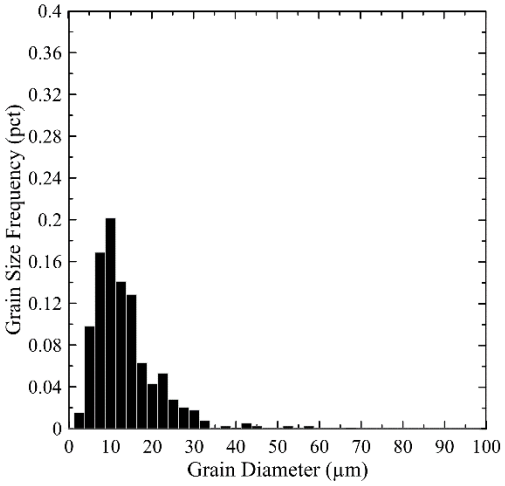


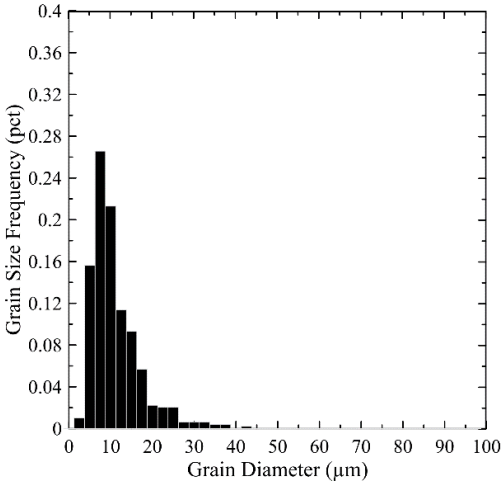
Figure D-4 Grain size frequency determined by line-intercept measurement in MATLAB of the 0 pct WR condition for both alloys after 0 min of simulated carburization where 4121Al has been previously subjected to (a) 0 pct CR, (c) 5 pct CR, (e) 10 pct CR, and (g) 25 pct CR and 4121Nb after (b) 0 pct CR, (d) 5 pct CR, (f) 10 pct CR, and (h) 25 pct CR.

Figure D-4 Continued

10 pct CR

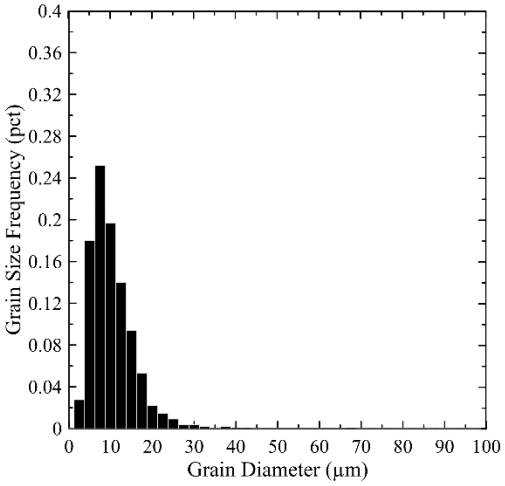


(e)

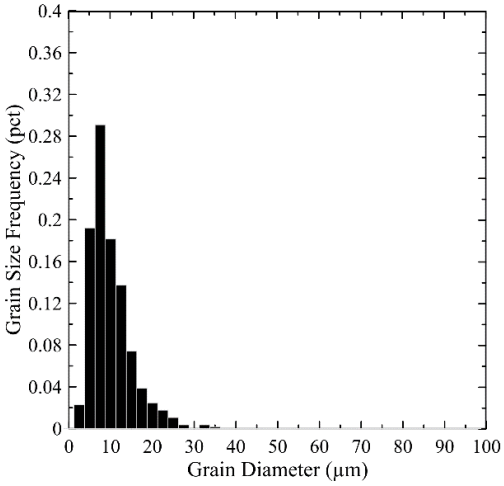


(f)

25 pct CR



(g)



(h)

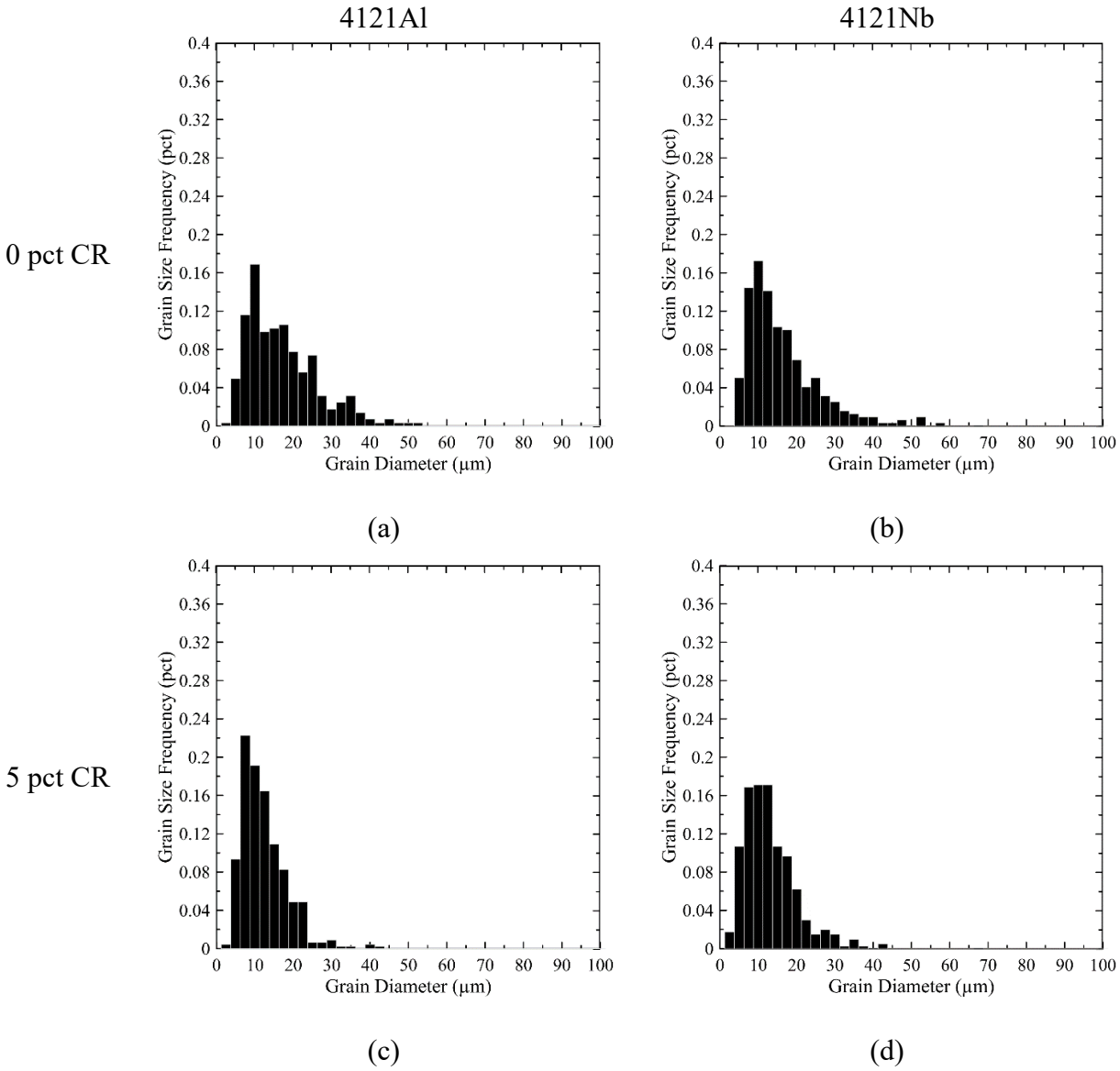
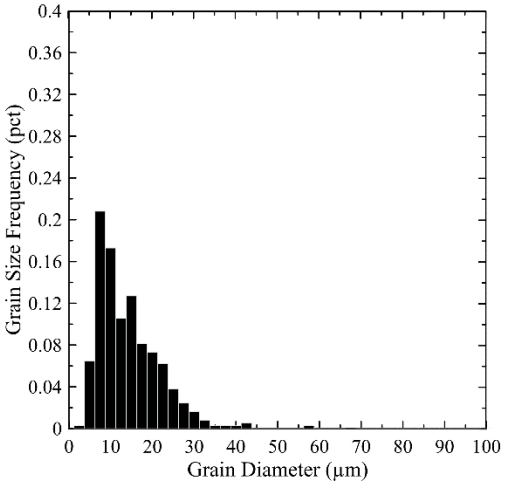


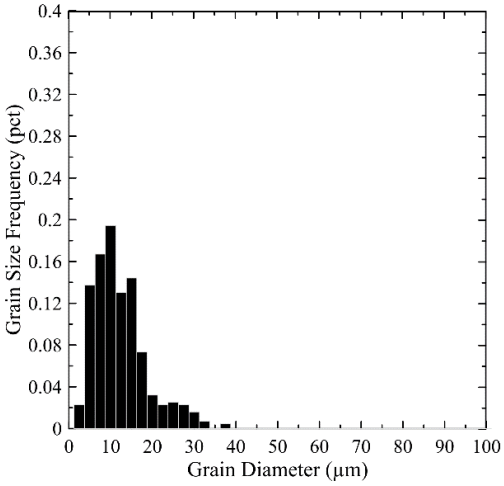
Figure D-5 Grain size frequency determined by line-intercept measurement in MATLAB of the 0 pct WR condition for both alloys after 30 min of simulated carburization where 4121Al has been previously subjected to (a) 0 pct CR, (c) 5 pct CR, (e) 10 pct CR, and (g) 25 pct CR and 4121Nb after (b) 0 pct CR, (d) 5 pct CR, (f) 10 pct CR, and (h) 25 pct CR.

Figure D-5 Continued

10 pct CR

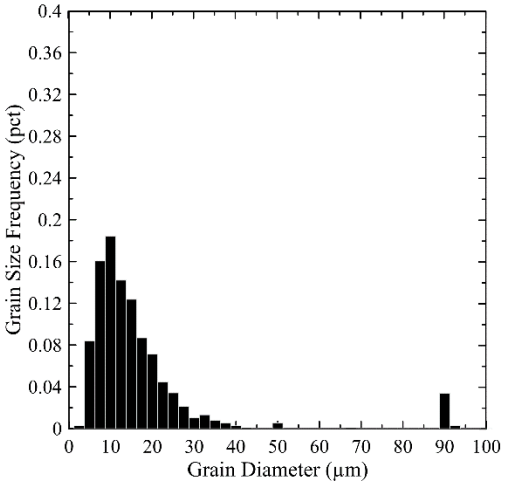


(e)

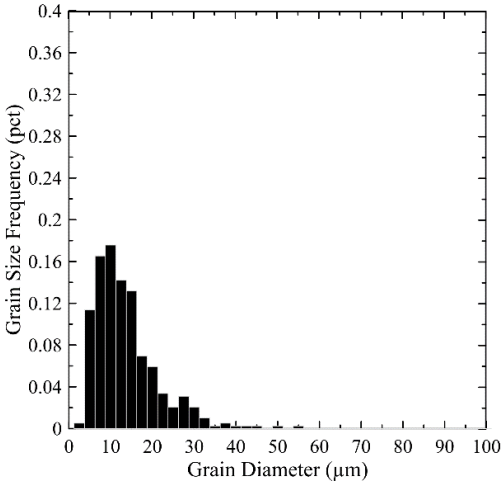


(f)

25 pct CR



(g)



(h)

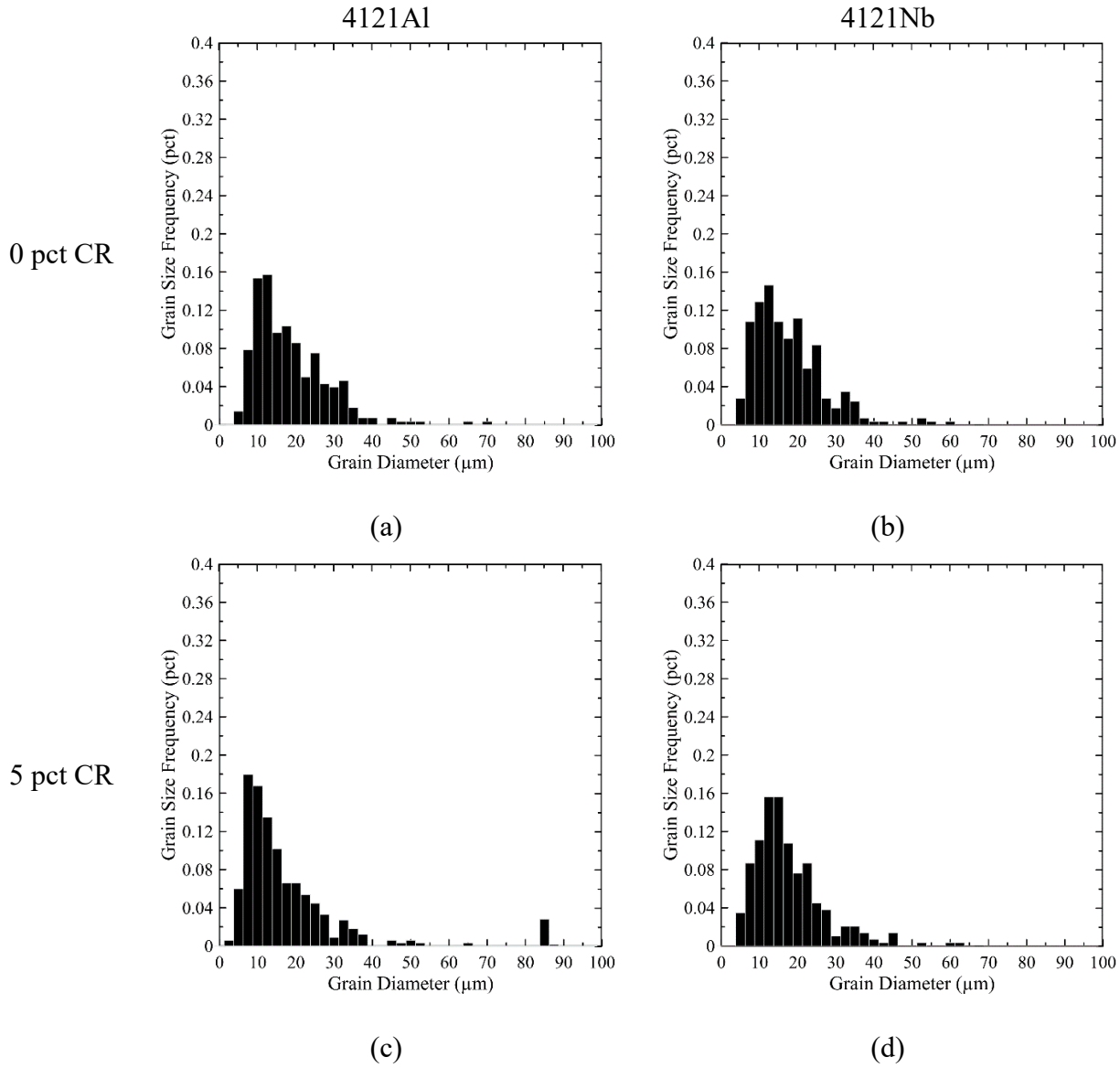
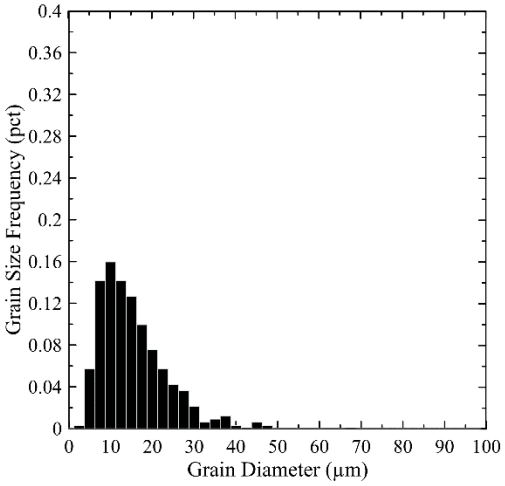


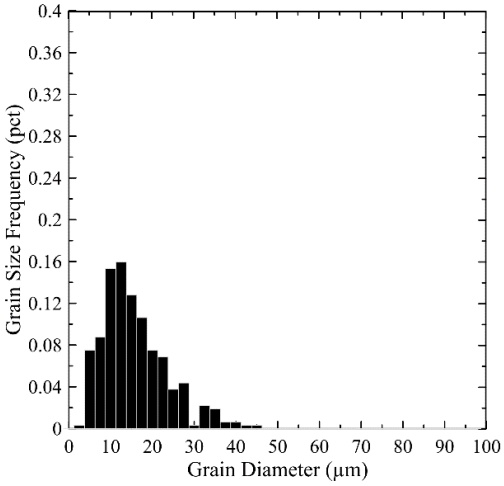
Figure D-6 Grain size frequency determined by line-intercept measurement in MATLAB of the 0 pct WR condition for both alloys after 328 min of simulated carburization where 4121Al has been previously subjected to (a) 0 pct CR, (c) 5 pct CR, (e) 10 pct CR, and (g) 25 pct CR and 4121Nb after (b) 0 pct CR, (d) 5 pct CR, (f) 10 pct CR, and (h) 25 pct CR.

Figure D-6 Continued

10 pct CR

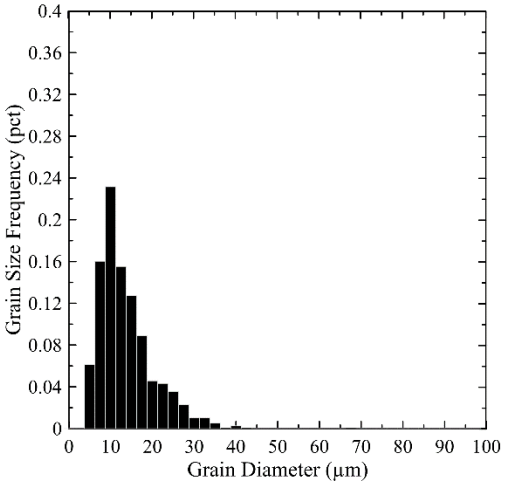


(e)

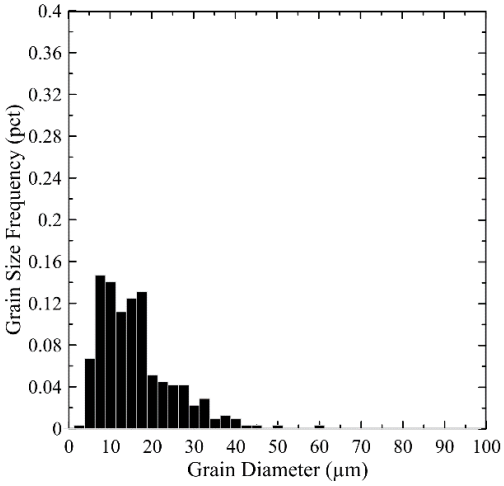


(f)

25 pct CR



(g)



(h)

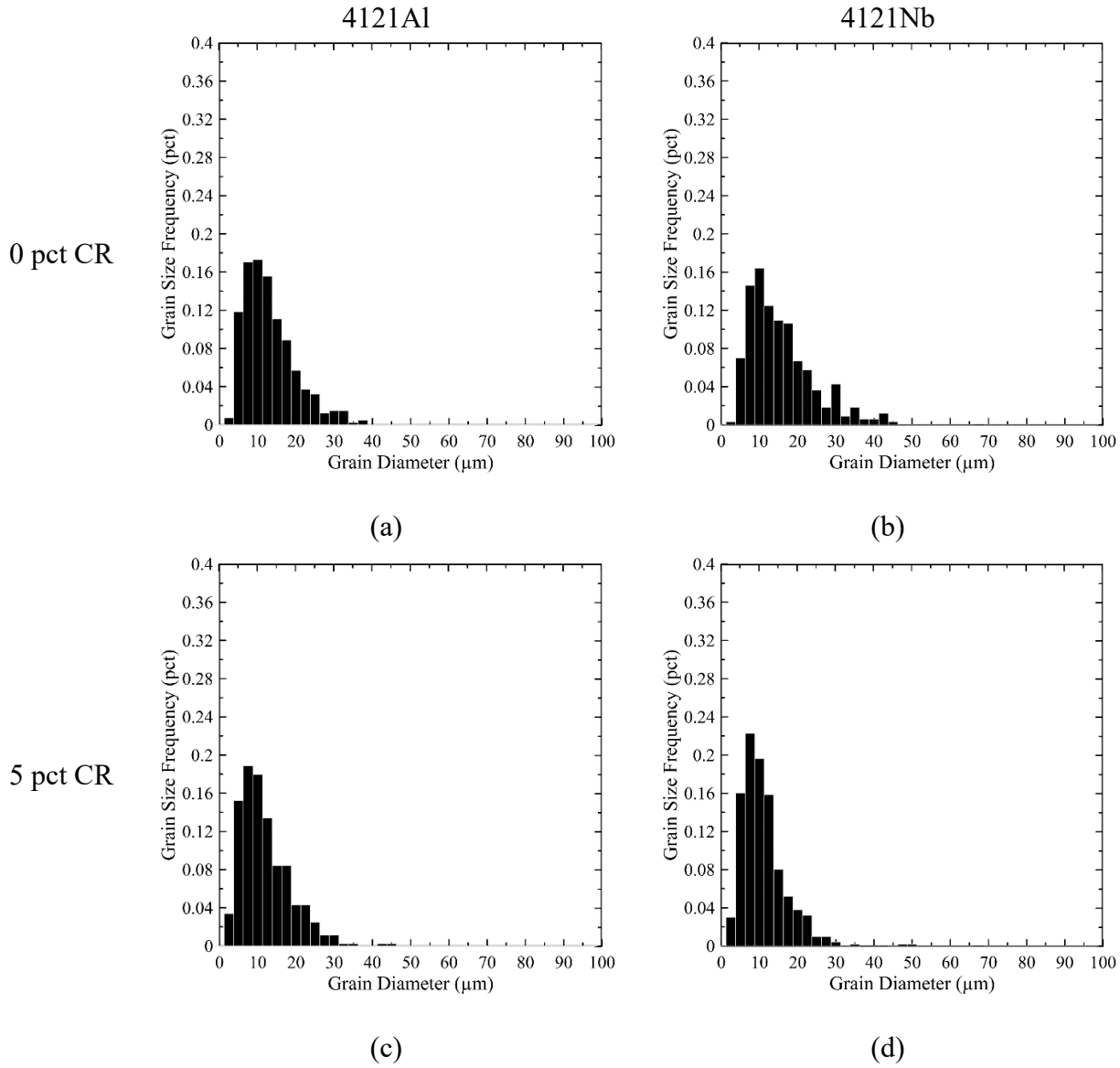
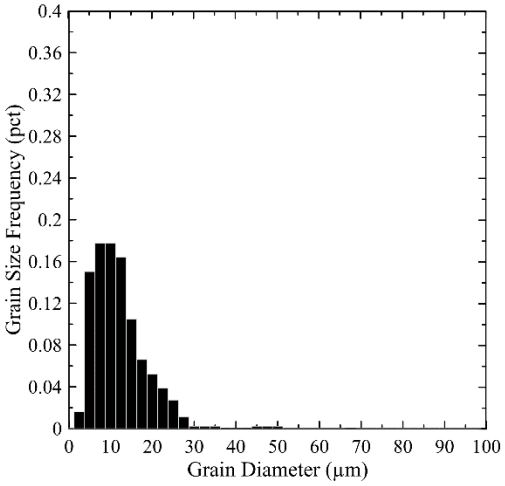


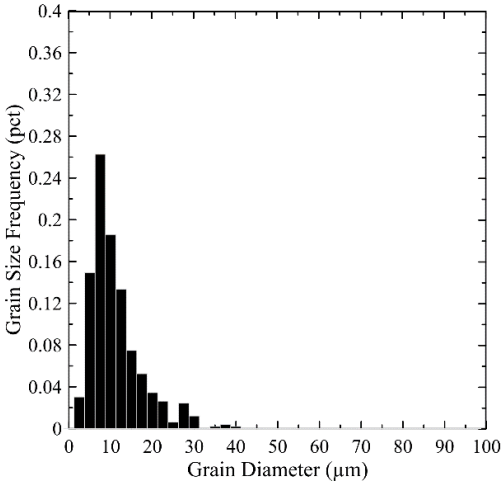
Figure D-7 Grain size frequency determined by line-intercept measurement in MATLAB of the 10 pct WR condition for both alloys after 0 min of simulated carburization where 4121Al has been previously subjected to (a) 0 pct CR, (c) 5 pct CR, (e) 10 pct CR, and (g) 25 pct CR and 4121Nb after (b) 0 pct CR, (d) 5 pct CR, (f) 10 pct CR, and (h) 25 pct CR.

Figure D-7 Continued

10 pct CR

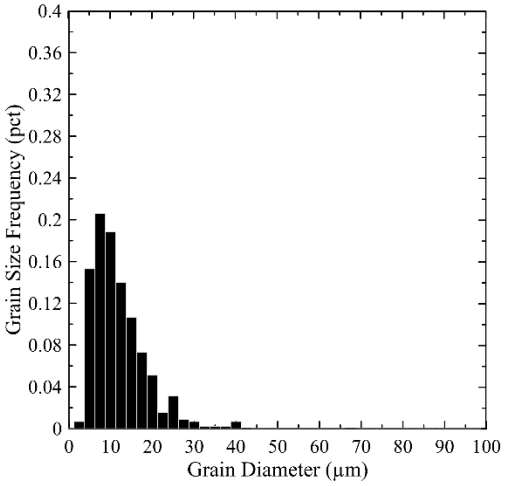


(e)

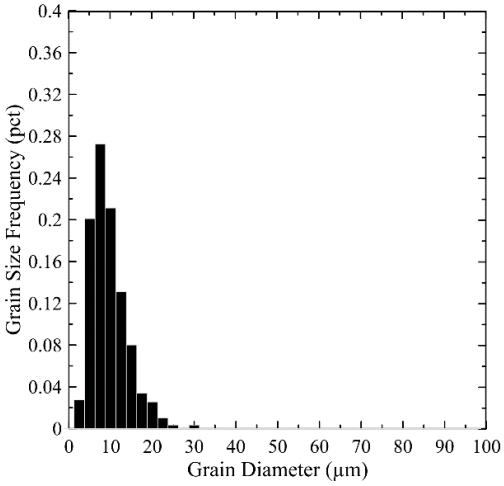


(f)

25 pct CR



(g)



(h)

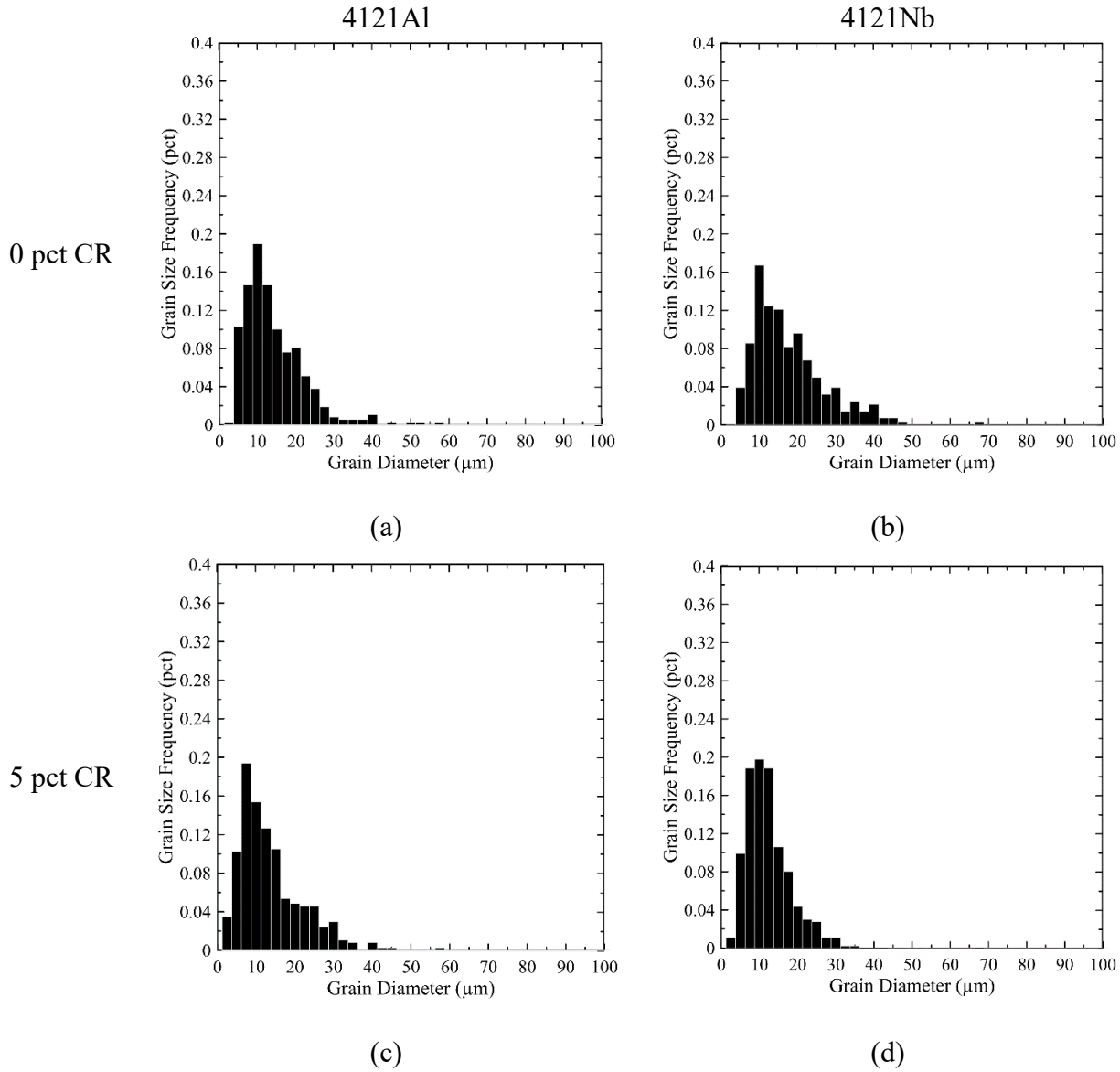
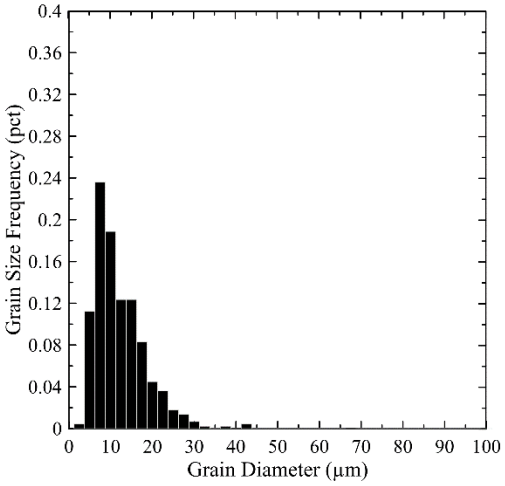


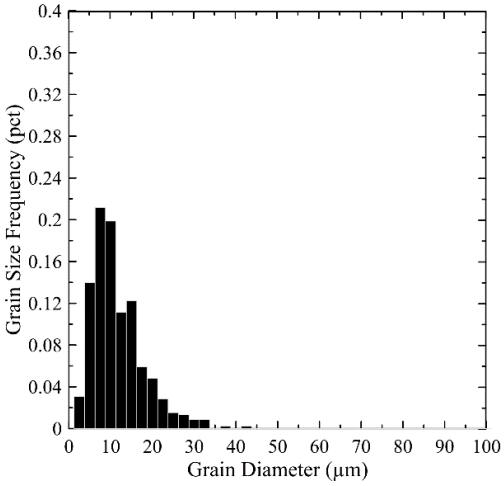
Figure D-8 Grain size frequency determined by line-intercept measurement in MATLAB of the 10 pct WR condition for both alloys after 30 min of simulated carburization where 4121Al has been previously subjected to (a) 0 pct CR, (c) 5 pct CR, (e) 10 pct CR, and (g) 25 pct CR and 4121Nb after (b) 0 pct CR, (d) 5 pct CR, (f) 10 pct CR, and (h) 25 pct CR.

Figure D-8 Continued

10 pct CR

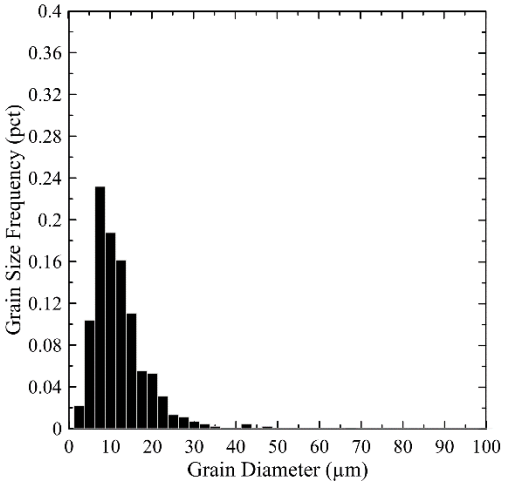


(e)

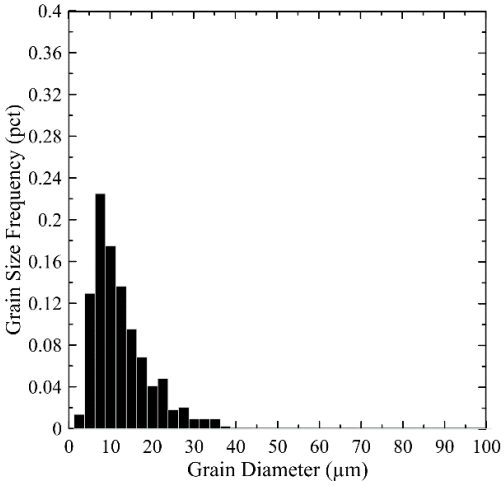


(f)

25 pct CR



(g)



(h)

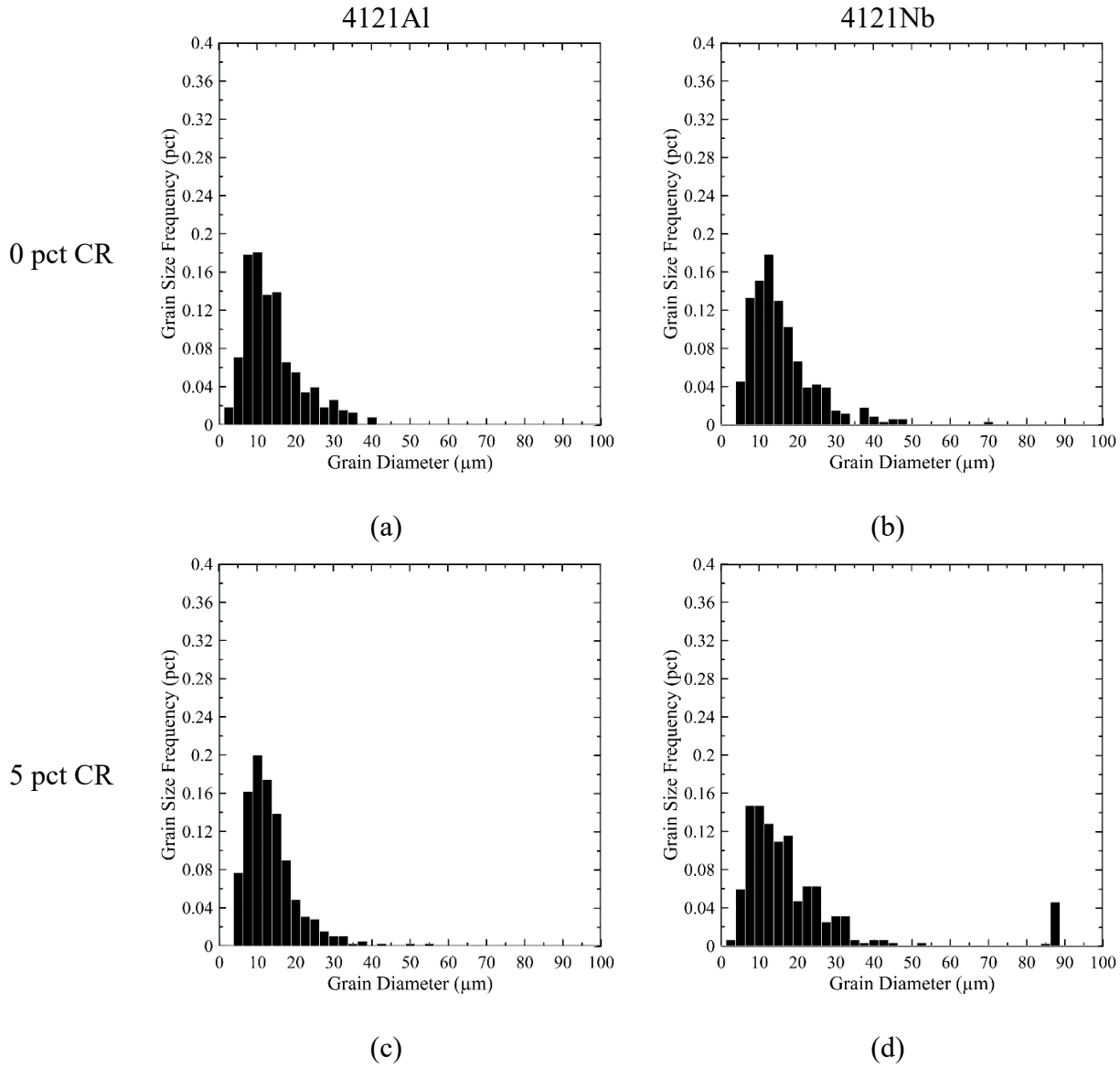
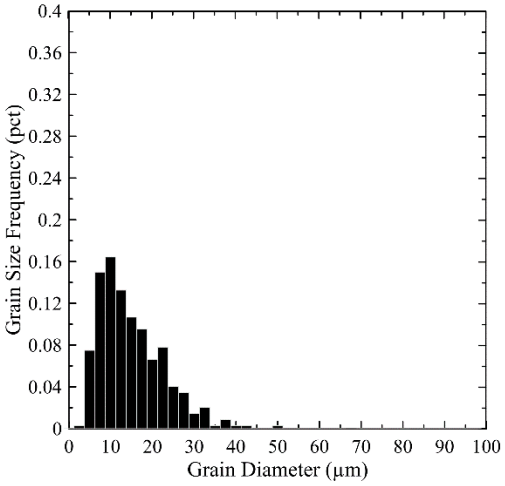


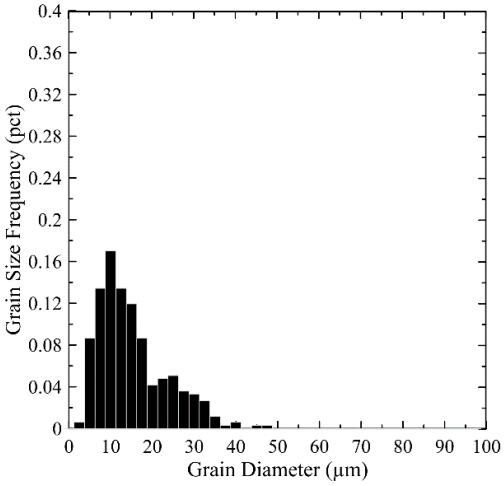
Figure D-9 Grain size frequency determined by line-intercept measurement in MATLAB of the 10 pct WR condition for both alloys after 328 min of simulated carburization where 4121Al has been previously subjected to (a) 0 pct CR, (c) 5 pct CR, (e) 10 pct CR, and (g) 25 pct CR and 4121Nb after (b) 0 pct CR, (d) 5 pct CR, (f) 10 pct CR, and (h) 25 pct CR.

Figure D-9 Continued

10 pct CR

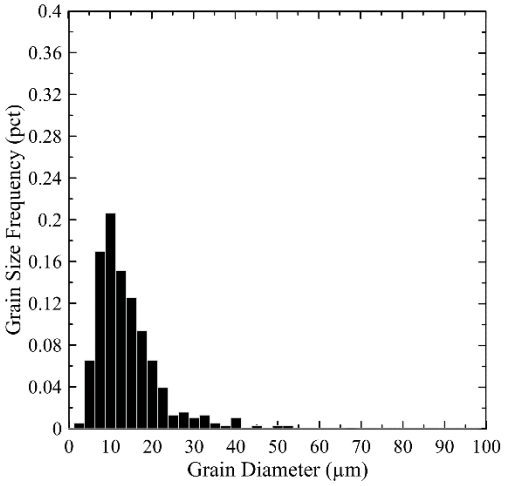


(e)

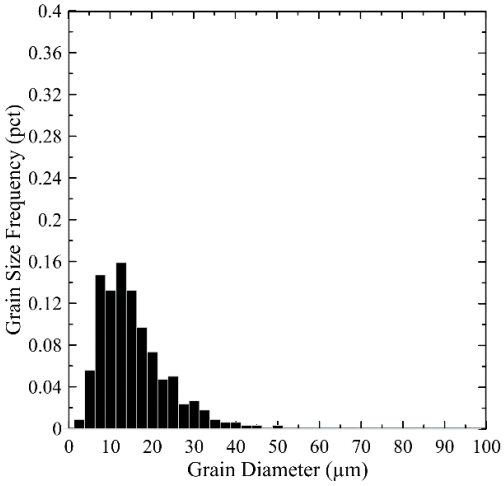


(f)

25 pct CR



(g)



(h)

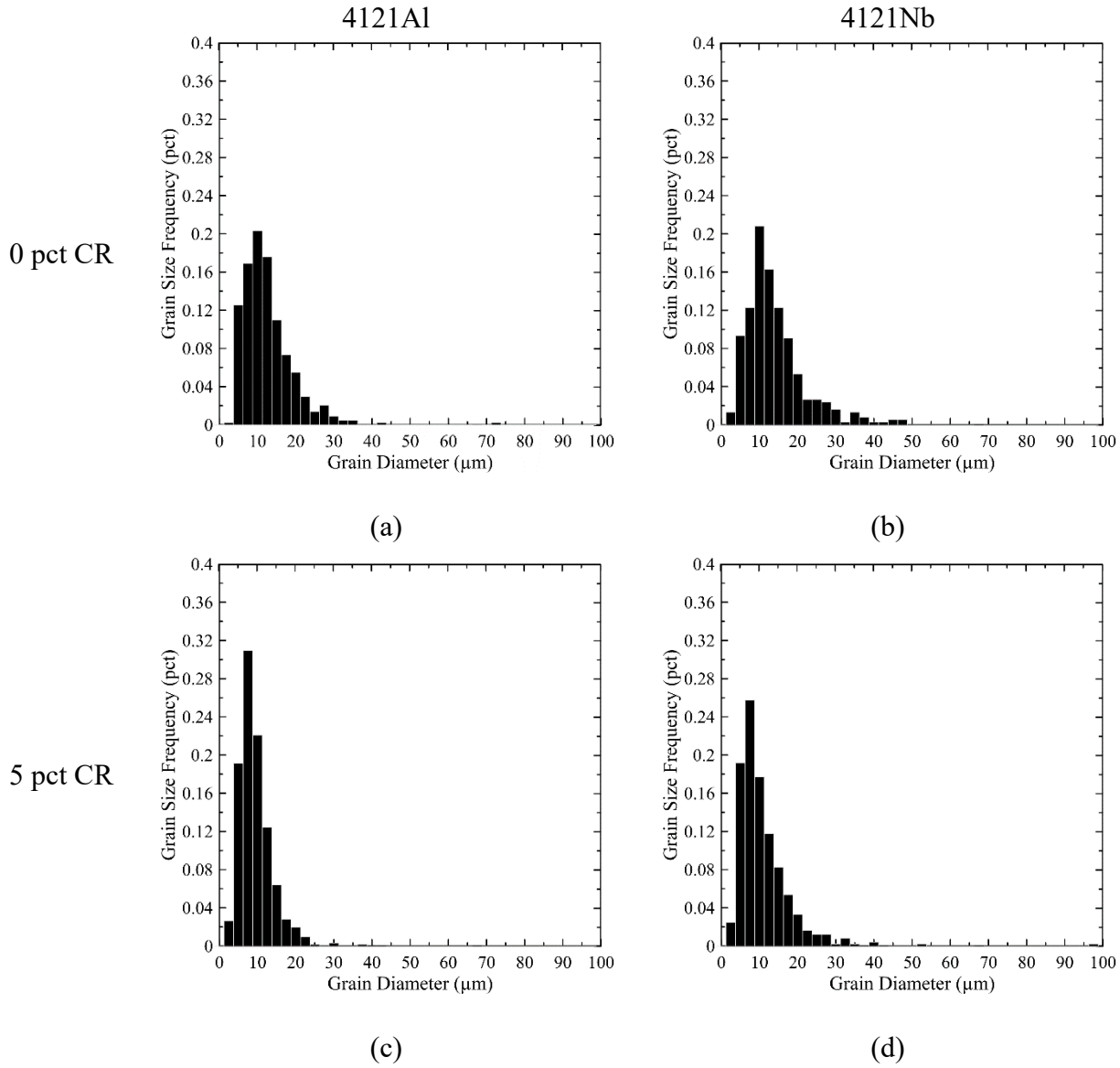
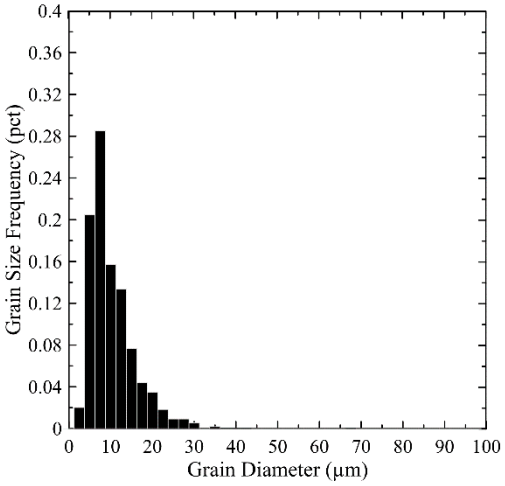


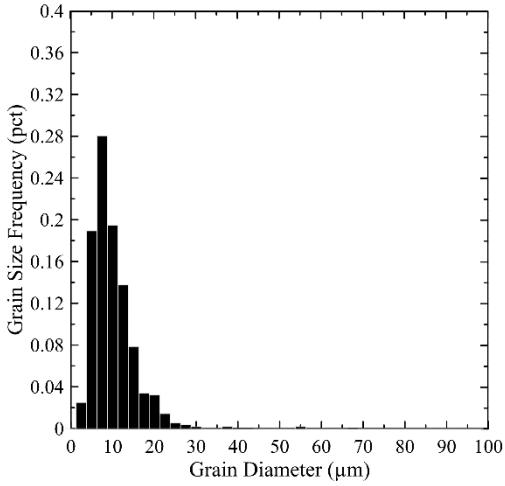
Figure D-10 Grain size frequency determined by line-intercept measurement in MATLAB of the 25 pct WR condition for both alloys after 0 min of simulated carburization where 4121Al has been previously subjected to (a) 0 pct CR, (c) 5 pct CR, (e) 10 pct CR, and (g) 25 pct CR and 4121Nb after (b) 0 pct CR, (d) 5 pct CR, (f) 10 pct CR, and (h) 25 pct CR.

Figure D-10 Continued

10 pct CR

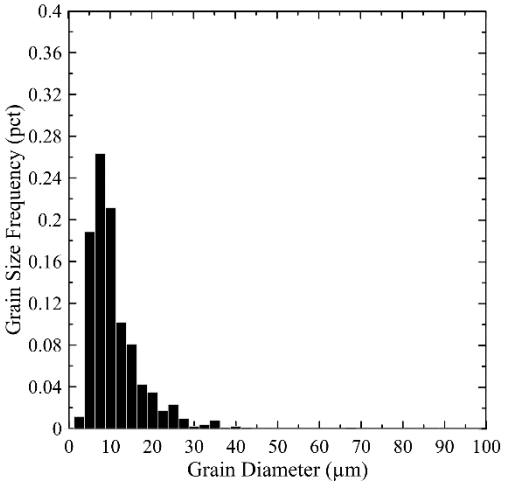


(e)

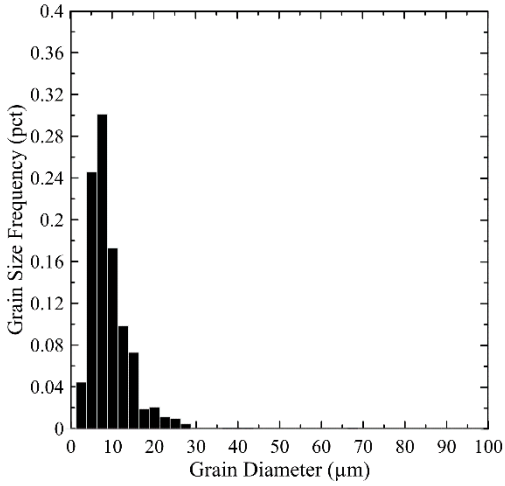


(f)

25 pct CR



(g)



(h)

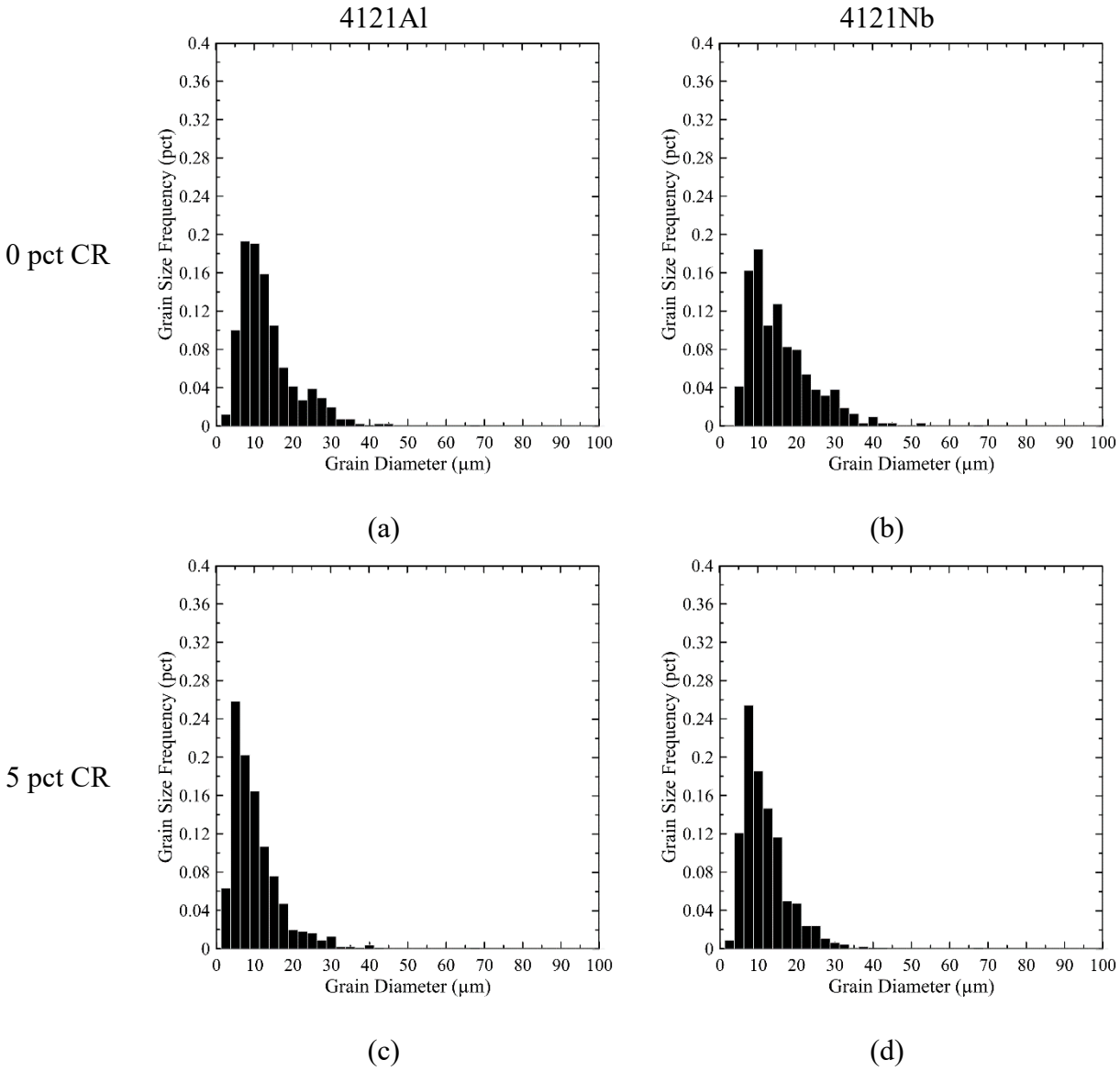
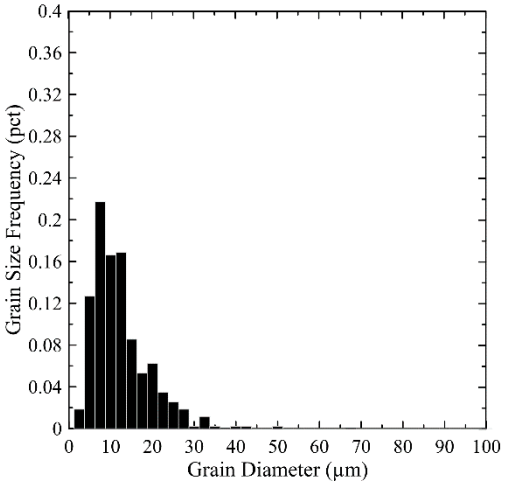


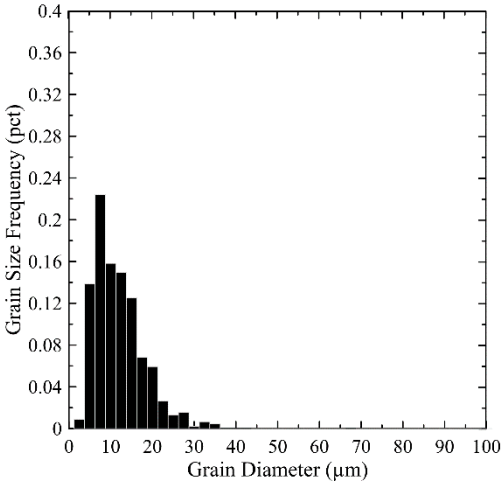
Figure D-11 Grain size frequency determined by line-intercept measurement in MATLAB of the 25 pct WR condition for both alloys after 30 min of simulated carburization where 4121Al has been previously subjected to (a) 0 pct CR, (c) 5 pct CR, (e) 10 pct CR, and (g) 25 pct CR and 4121Nb after (b) 0 pct CR, (d) 5 pct CR, (f) 10 pct CR, and (h) 25 pct CR.

Figure D-11 Continued

10 pct CR

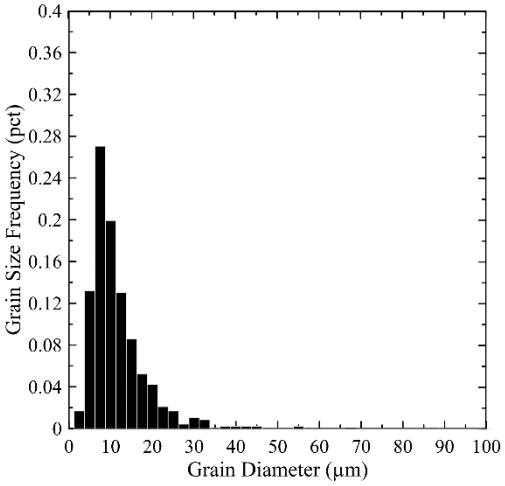


(e)

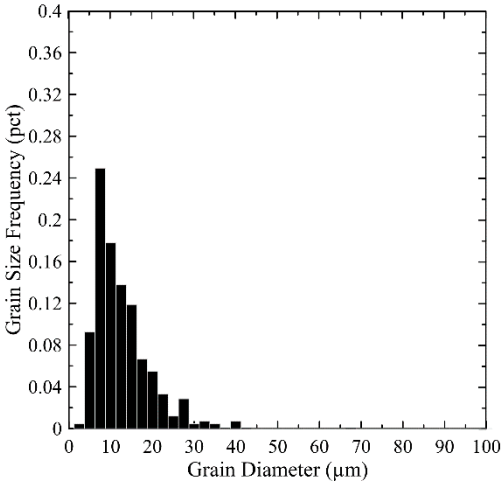


(f)

25 pct CR



(g)



(h)

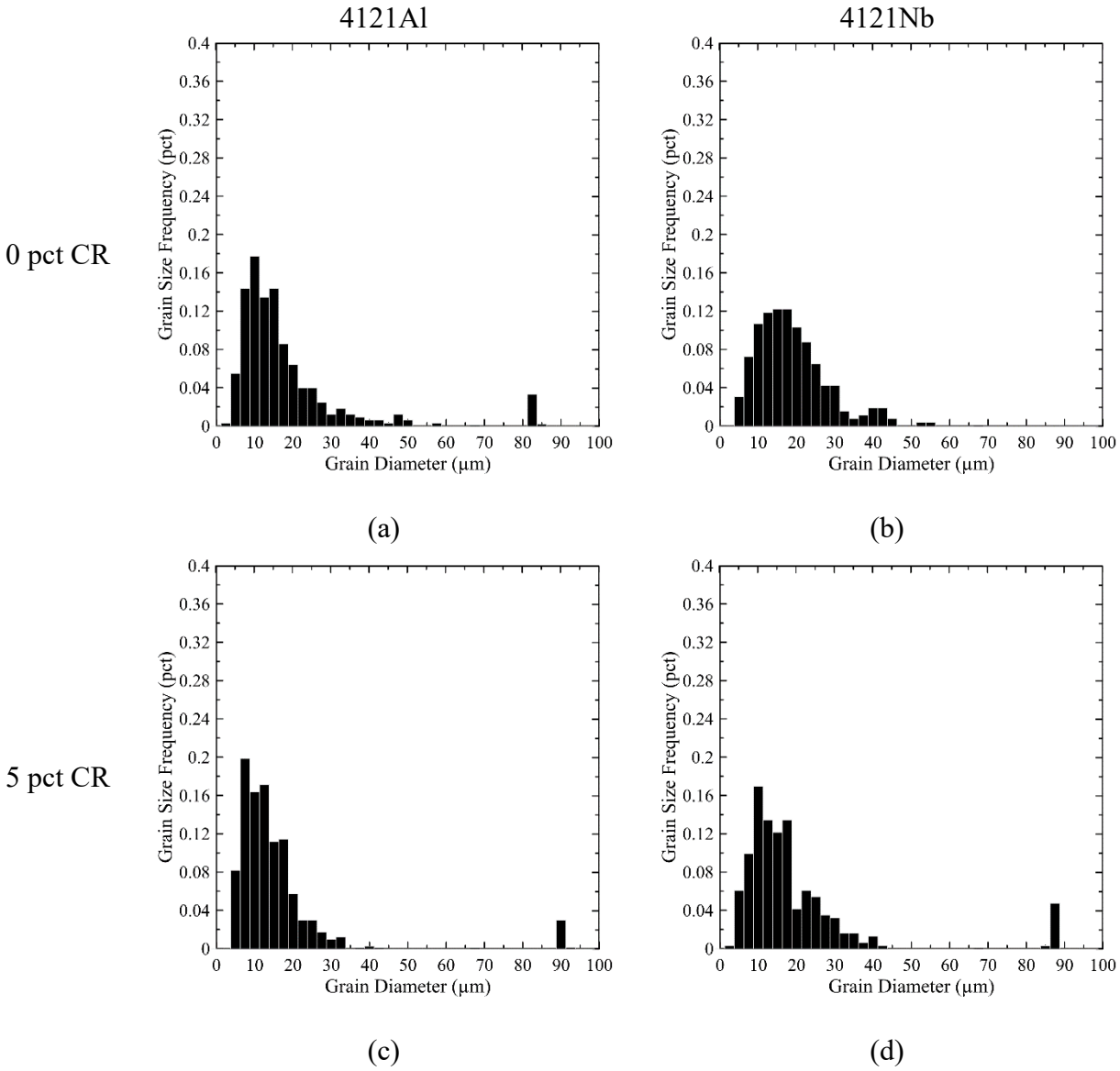
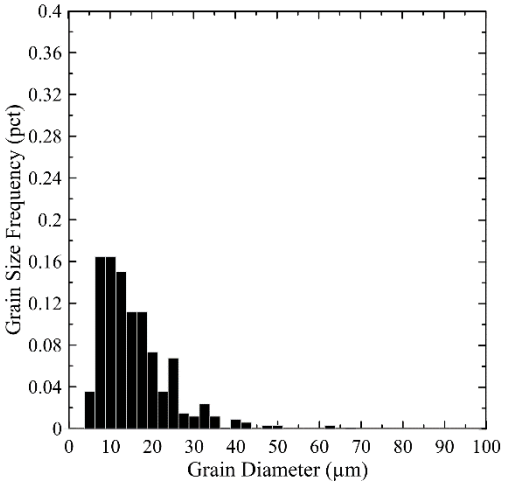


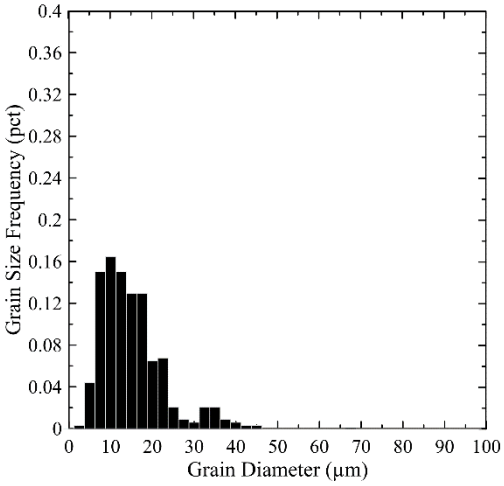
Figure D-12 Grain size frequency determined by line-intercept measurement in MATLAB of the 25 pct WR condition for both alloys after 328 min of simulated carburization where 4121Al has been previously subjected to (a) 0 pct CR, (c) 5 pct CR, (e) 10 pct CR, and (g) 25 pct CR and 4121Nb after (b) 0 pct CR, (d) 5 pct CR, (f) 10 pct CR, and (h) 25 pct CR.

Figure D-12 Continued

10 pct CR

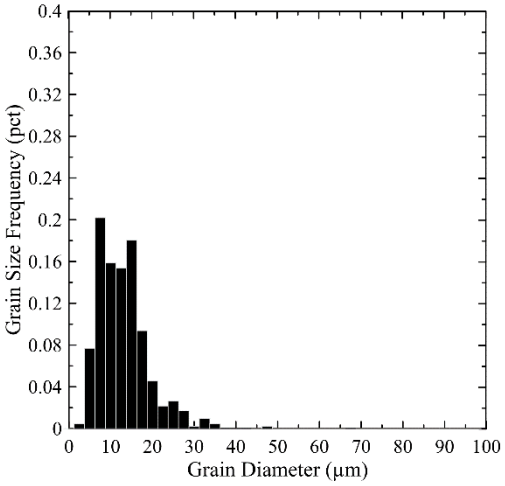


(e)

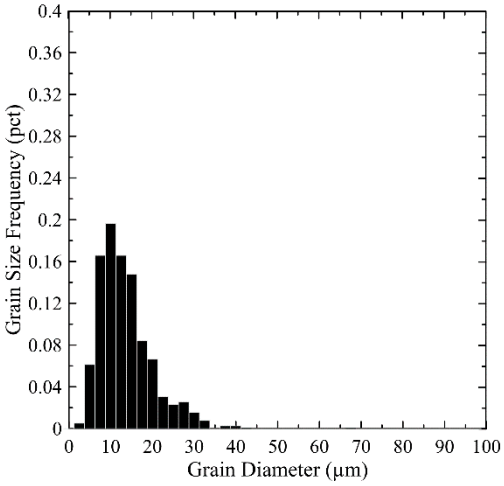


(f)

25 pct CR



(g)



(h)

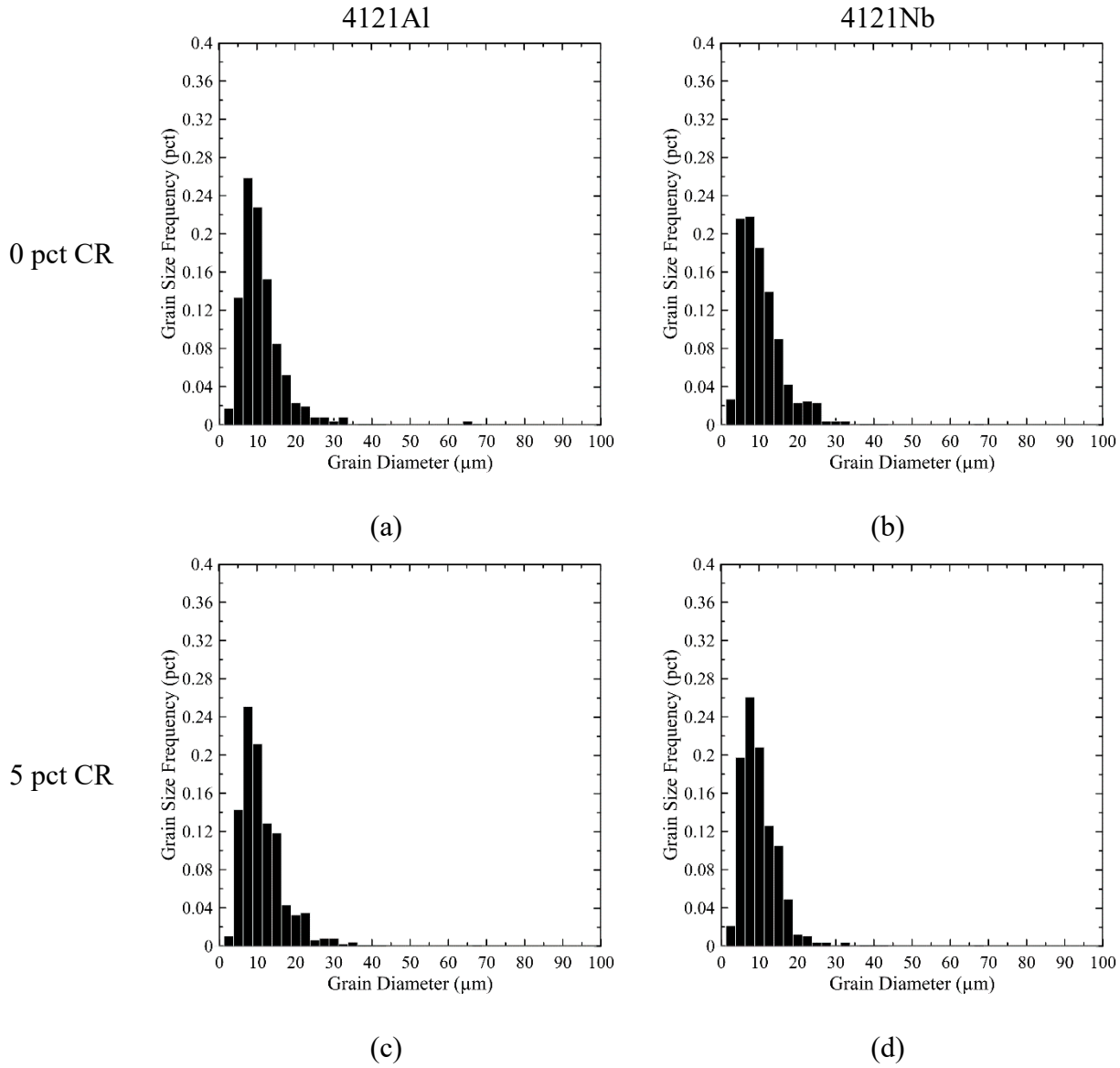
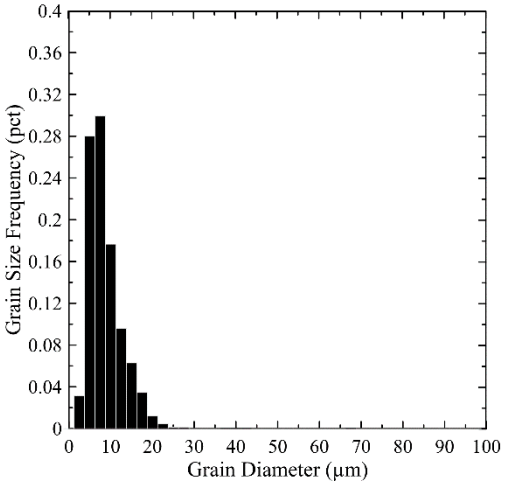


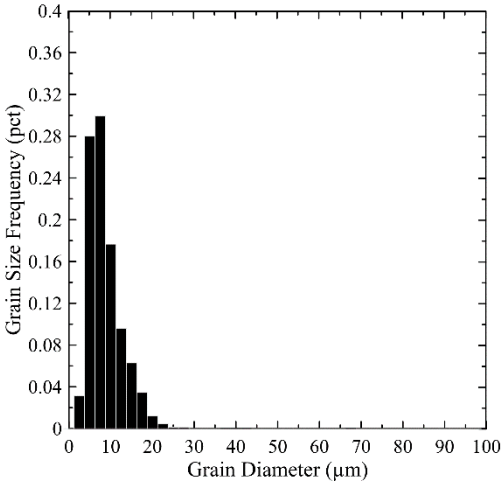
Figure D-13 Grain size frequency determined by line-intercept measurement in MATLAB of the 50 pct WR condition for both alloys after 0 min of simulated carburization where 4121Al has been previously subjected to (a) 0 pct CR, (c) 5 pct CR, (e) 10 pct CR, and (g) 25 pct CR and 4121Nb after (b) 0 pct CR, (d) 5 pct CR, (f) 10 pct CR, and (h) 25 pct CR.

Figure D-13 Continued

10 pct CR

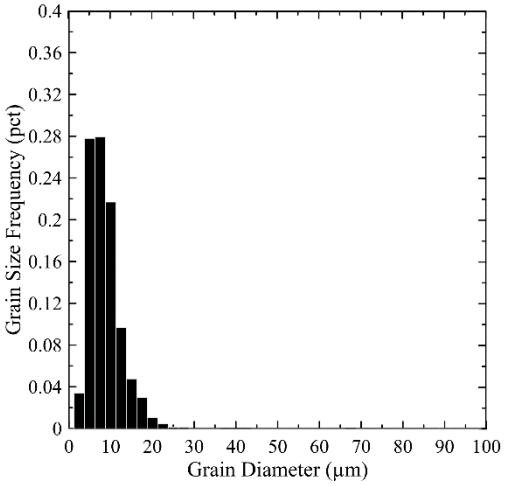


(e)

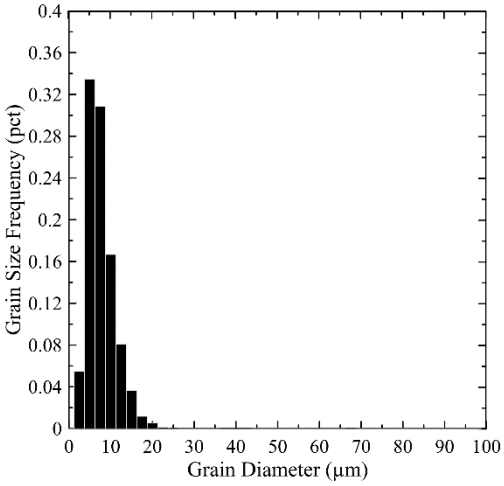


(f)

25 pct CR



(g)



(h)

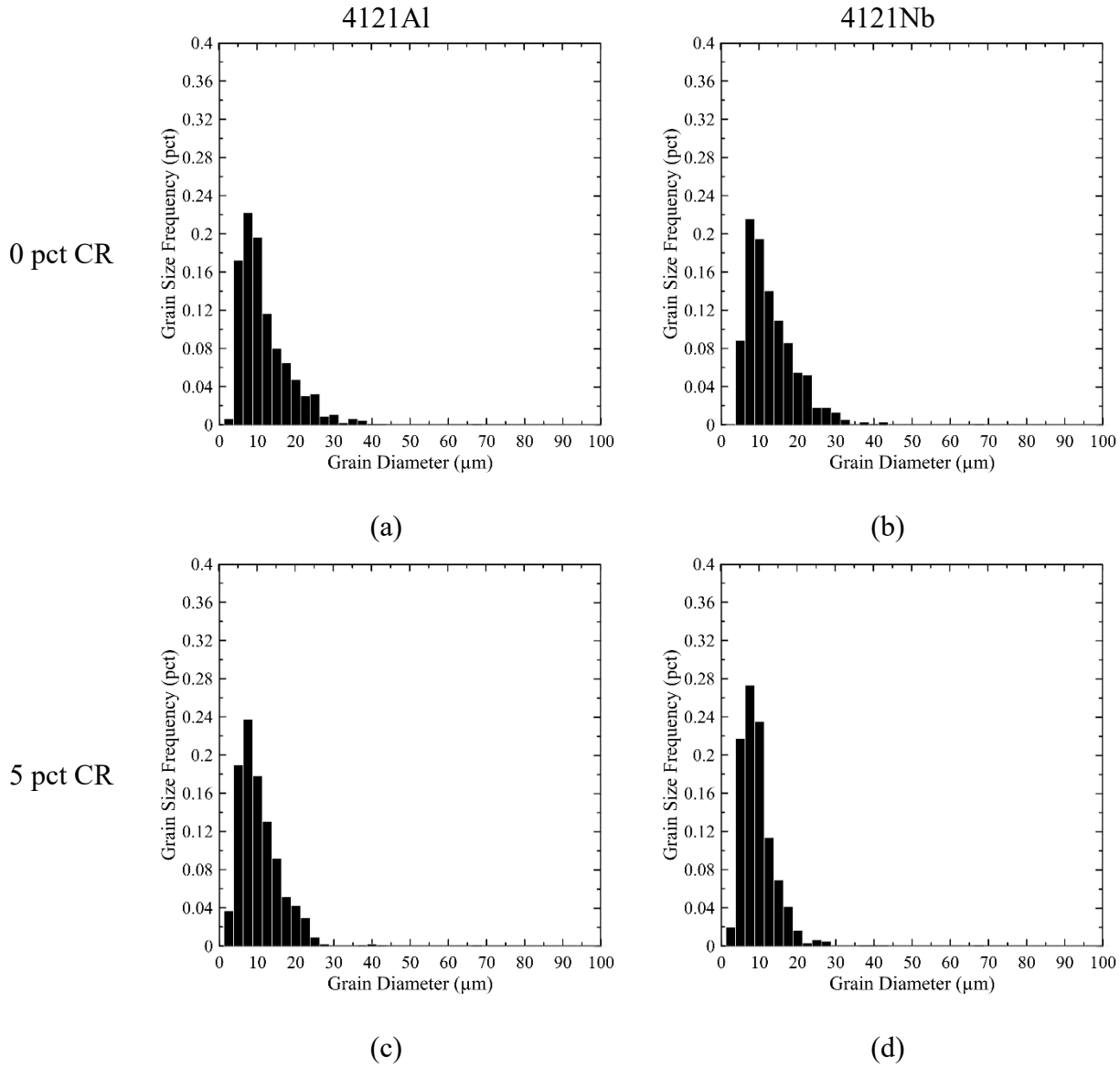
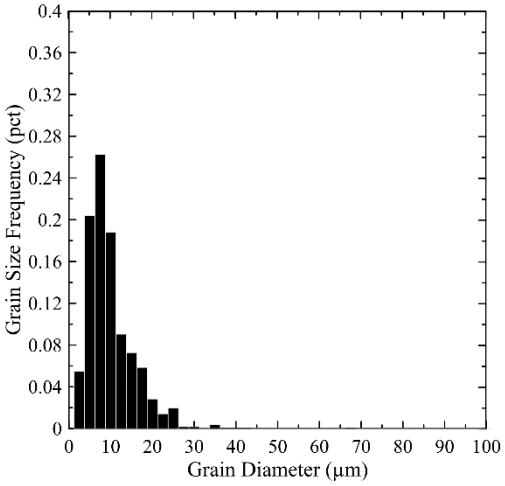


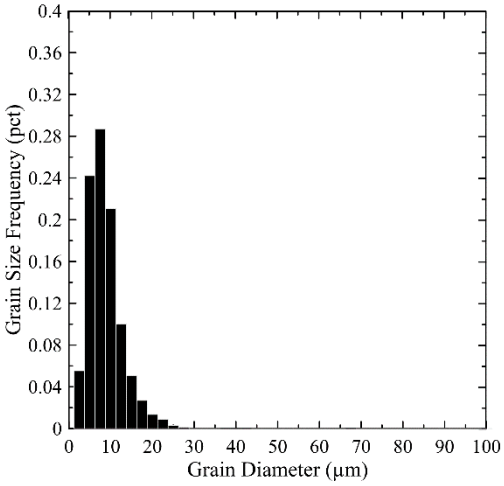
Figure D-14 Grain size frequency determined by line-intercept measurement in MATLAB of the 50 pct WR condition for both alloys after 328 min of simulated carburization where 4121Al has been previously subjected to (a) 0 pct CR, (c) 5 pct CR, (e) 10 pct CR, and (g) 25 pct CR and 4121Nb after (b) 0 pct CR, (d) 5 pct CR, (f) 10 pct CR, and (h) 25 pct CR.

Figure D-14 Continued

10 pct CR

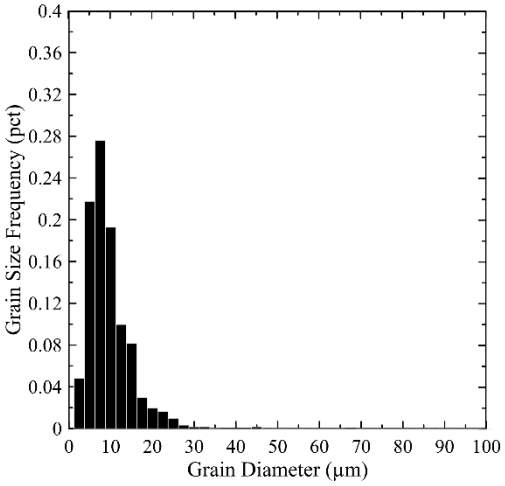


(e)

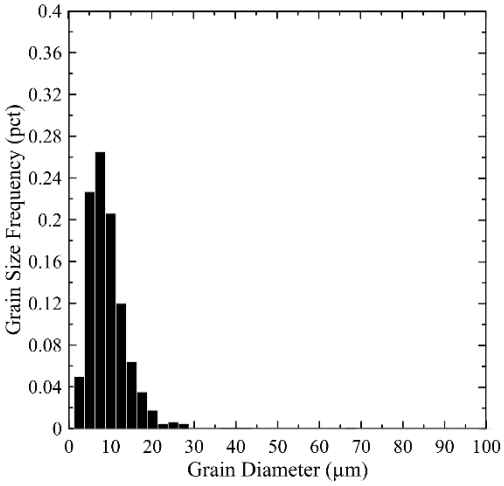


(f)

25 pct CR



(g)



(h)

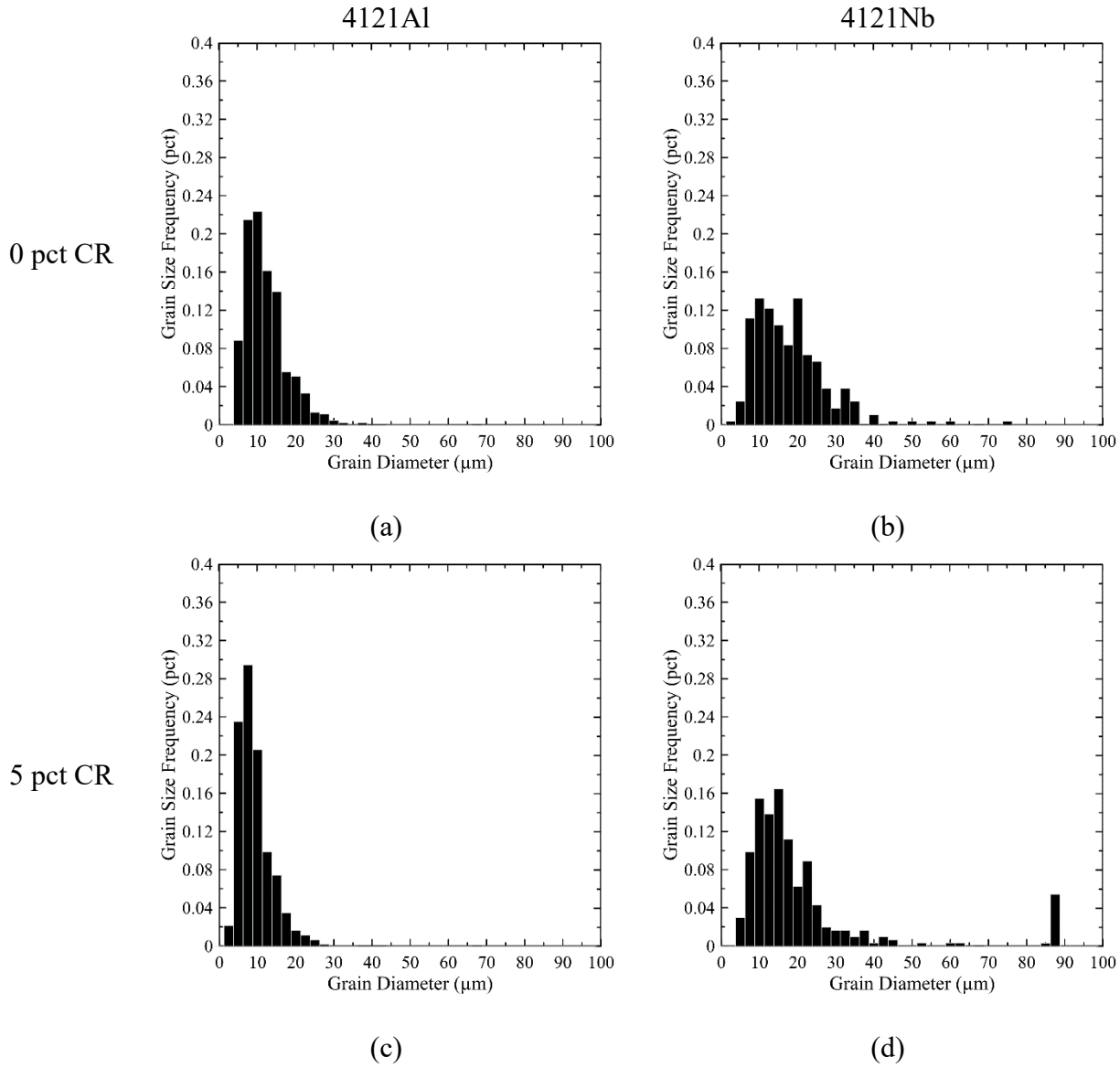
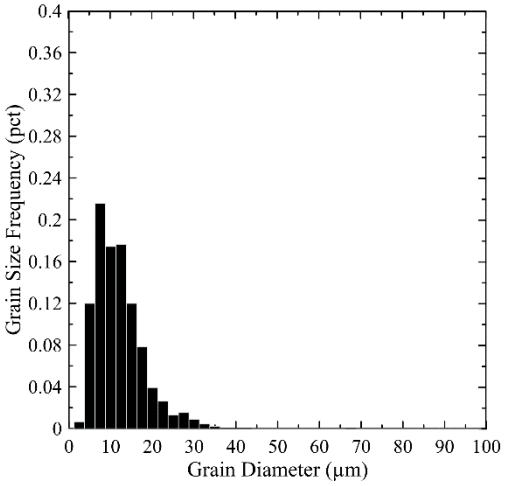


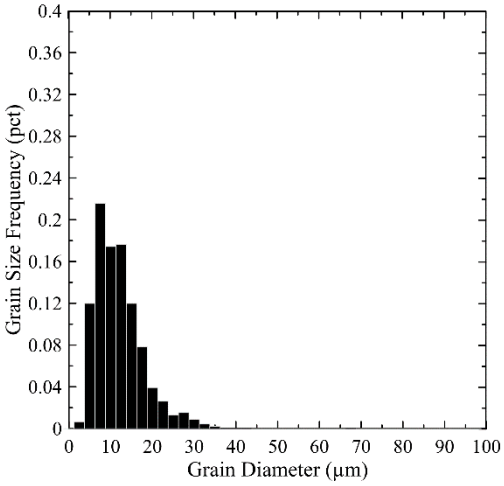
Figure D-15 Grain size frequency determined by line-intercept measurement in MATLAB of the 50 pct WR condition for both alloys after 328 min of simulated carburization where 4121Al has been previously subjected to (a) 0 pct CR, (c) 5 pct CR, (e) 10 pct CR, and (g) 25 pct CR and 4121Nb after (b) 0 pct CR, (d) 5 pct CR, (f) 10 pct CR, and (h) 25 pct CR.

Figure D-15 Continued

10 pct CR

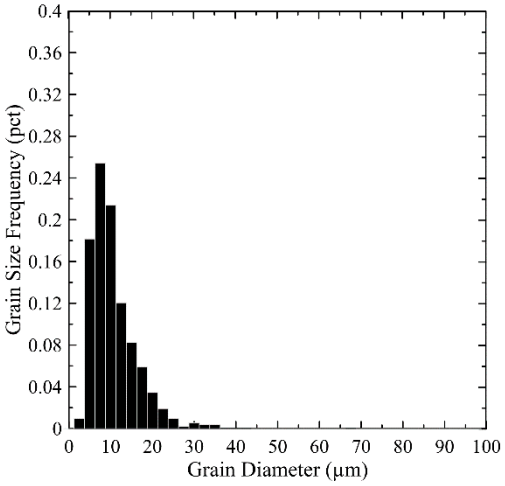


(e)

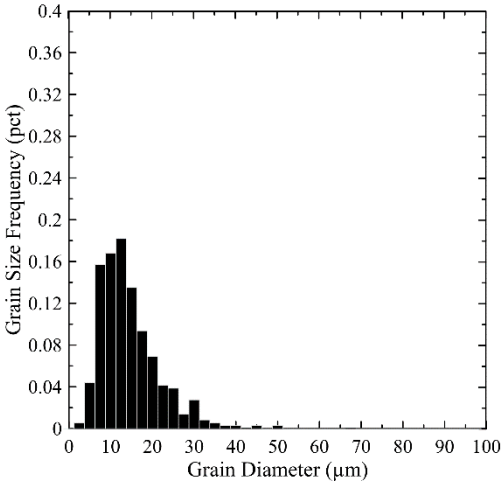


(f)

25 pct CR



(g)



(h)

APPENDIX E: COPYRIGHT PERMISSIONS

Permissions to include previously published material in this thesis is below.

- Figures 2.1, 2.2, 2.3, 2.15, 2.16, and 4.11 and Tables 2.1-2.3 were reproduced from the following sources associated with the MME department. Given the authors' affiliations, permissions for inclusion in this thesis were conveyed by the current department faculty.
    - G. Krauss, Steels - Processing, Structure, and Performance. ASM International, pp. 31, 2005.
    - G. Krauss, "Steel Heat Treatment and Processing Principles," ASM International, Materials Park, Ohio, pp. 194. 1990.
    - S. C. Kennett, "Strengthening and Toughening Mechanisms in Low-C Microalloyed Martensitic Steel as Influenced by Austenite Conditioning," Colorado School of Mines, PhD Thesis, pp. 21, 2014.
    - S. Lee, R. L. Cryderman, D. K. Matlock, and J. G. Speer, "Controlling Austenite Grain Growth in Annealed and Cold Formed Steel During Carburizing," Colorado School of Mines, ASPPRC Research Report No. MT-SRC-021-007, 2021.
    - C. M. Enloe, "The Effect of Molybdenum on Niobium, Titanium Carbonitride Precipitate Evolution and Grain Refinement in High-Temperature Vacuum Carburizing Alloys," Colorado School of Mines, PhD Thesis, 2013.
- Figures 2.9, 2.13, and 2.14 were recreated in accordance with the open-access policy of Multidisciplinary Digital Publishing Institute (MDPI).
- Figures 2.10, 2.11, and 2.12 were recreated in accordance with the open-access policy of the Iron and Steel Institute of Japan (ISIJ).
- Figure 2.4 is reprinted from the *SAE Technical Paper Series*, Vol 109, Issue 5, J.P Wise and D.K. Matlock, "Bending Fatigue of Carburized Steels: A Statistical Analysis of Process and Microstructural Parameters, 182-191, (1970), used with the following permission from the publisher, Society of Automotive Engineers:

Order Date	11-Dec-2023	Type of Use	Republish in a thesis/dissertation
Order License ID	1426008-1		
ISSN	0148-7191	Publisher	SOCIETY OF AUTOMOTIVE ENGINEERS,
		Portion	Chart/graph/table/figure

LICENSED CONTENT

Publication Title	SAE technical paper series	Rightsholder	SAE International
Article Title	Bending Fatigue of Carburized Steels: A Statistical Analysis of Process and Microstructural Parameters	Publication Type	Monographic Series
		Start Page	182
		End Page	191
		Issue	5
		Volume	109
Author/Editor	SOCIETY OF AUTOMOTIVE ENGINEERS.		
Date	01/01/1970		
Language	English		
Country	United States of America		

- Figure 2.6 is reprinted from the *Journal of Materials Engineering and Performance*, Vol 29, Issue 6, E.J Seo, J.G. Speer, D.K. Matlock, and R.L. Cryderman, “Effect of Mo in Combination with Nb on Austenite Grain Size Control in Vacuum Carburizing Steels”, 3575-3584, (2020), used with the following permission from the publisher, Springer Nature:

SPRINGER NATURE LICENSE

TERMS AND CONDITIONS

Dec 11, 2023

This Agreement between Colorado School of Mines -- James Gruich ("You") and

Springer Nature ("Springer Nature") consists of your license details and the terms and

conditions provided by Springer Nature and Copyright Clearance Center.

License Number 5686130198638

License date Dec 11, 2023

Licensed Content Publisher Springer Nature

Licensed Content Publication Journal of Materials Engineering and Performance

Licensed Content Title Effect of Mo in Combination with Nb on Austenite

Grain Size Control in Vacuum Carburizing Steels

Licensed Content Author Eun Jung Seo et al

Licensed Content Date Apr 2, 2020

Type of Use Thesis/Dissertation

Requestor type academic/university or research institute

Format print and electronic

Portion figures/tables/illustrations

Number of figures/tables/illustrations 1

Will you be translating? no

Circulation/distribution 1 - 29

Author of this Springer Nature content no

Title of new work

The Effects of Thermomechanical Pretreatment on Abnormal Grain Growth During Simulated Carburization

Institution name Colorado School of Mines

Expected presentation date Dec 2023

Order reference number 1

Portions Figure 9

Requestor Location

Colorado School of Mines

923 18th St

GOLDEN, CO 80401

United States

Attn: Colorado School of Mines

Total 0.00 USD

- Figure 2.6 is reprinted from *Acta Materialia*, Vol 49, Issue 5, B. Dutta, E.J. Palmiere, and C.M. Sellars, “Modelling the Kinetics of Strain Induced Precipitation in Nb Microalloyed Steels”, 785-594, (2001), used with the following permission from the publisher, Elsevier:

ELSEVIER LICENSE

TERMS AND CONDITIONS

Dec 11, 2023

This Agreement between Colorado School of Mines -- James Gruich ("You") and Elsevier

("Elsevier") consists of your license details and the terms and conditions provided by

Elsevier and Copyright Clearance Center.

License Number 5686141058834

License date Dec 11, 2023

Licensed Content Publisher Elsevier

Licensed Content

Publication Acta Materialia

Licensed Content Title Modelling the kinetics of strain induced precipitation in Nb microalloyed steels

Licensed Content Author B. Dutta,E.J. Palmiere,C.M. Sellars

Licensed Content Date Mar 14, 2001

Licensed Content Volume 49

Licensed Content Issue 5

Licensed Content Pages 10

Type of Use reuse in a thesis/dissertation

Portion figures/tables/illustrations

Number of figures/tables/illustrations 1

Format both print and electronic

Are you the author of this

Elsevier article? No

Will you be translating? No

Title of new work The Effects of Thermomechanical Pretreatment on Abnormal Grain Growth During Simulated Carburization

Institution name Colorado School of Mines

Expected presentation date Dec 2023

Order reference number 4

Portions Figure 2

Requestor Location

Colorado School of Mines

923 18th St

GOLDEN, CO 80401

United States

Attn: Colorado School of Mines

Publisher Tax ID 98-0397604

Total 0.00 USD